ADDIS ABABA UNIVERSITY

ADDIS ABABA INSTITUTE OF TECHNOLOGY

AFRICAN RAILWAY CENTER OF EXCELLENCE

INFLUENCE OF NON-UNIFORM RAILWAY TRACK MODULUS ON WHEEL-RAIL CONTACT DYNAMIC FORCES AND WHEEL TREAD WEAR.

A Finite Element Analysis Approach

A Thesis in Railway Engineering (Rolling Stock)

By

Lovejoy Mutswatiwa

July 17, 2020

A Thesis in Partial fulfillment for the degree of Master of Science.

A

Thesis

Presented to the African Railway Center of

Excellence Graduate College at Addis Ababa University

In Partial Fulfillment of Requirements

For the Degree of Masters of Science.

Addis Ababa Institute of Technology,

Addis Ababa University,

Major: Railway Engineering, Rolling Stock

Under the Supervision of Dr Celestin Nkundineza and the Co-

Supervision of

Professor Mehmet A. Guler
College of Engineering and Technology,
American University of the Middle East, Kuwait

Addis Ababa, Ethiopia

Email: mutswatiwalovejoy@gmail.com

CERTIFICATION

The undersigned members of the Addis Ababa Institute of Technology under the department of Railway Engineering have examined the thesis entitled '**INFLUENCE OF NON-UNIFORM RAILWAY TRACK MODULUS ON WHEEL-RAIL CONTACT DYNAMIC FORCES AND WHEEL TREAD WEAR**' presented by **Lovejoy Mutswatiwa**, a candidate for the degree of **Master of Science** in **Rolling Stock Design** and hereby certify that it is worthy of acceptance.

Board of Examiners

Dr Celestin Nkundineza	……..	……
Advisor	Signature	Date
……..	……..	……
Co-Advisor	Signature	Date
……..	……..	……
External Examiner	Signature	Date
……..	……..	……
Internal Examiner	Signature	Date
……..	……..	……
Chairperson of Department Graduate Committee (DGC)	Signature	Date

DECLARATION

I hereby declare that the research work entitled "**INFLUENCE OF NON-UNIFORM RAILWAY TRACK MODULUS ON WHEEL-RAIL CONTACT DYNAMIC FORCES AND WHEEL TREAD WEAR**" is my own work and that it has not been presented elsewhere for assessment as a thesis or research paper. Where material from other sources have been utilized proper acknowledgements and references are provided.

Lovejoy Mutswatiwa

Signature: ……..

ACKNOWLEDGEMENT

The work presented in this thesis was carried out at the Department of Railway Engineering, Addis Ababa Institute of Technology under the supervision and co-supervision of Dr. C. Nkundineza and Dr. M.A. Guler respectively. First and foremost, I would like to thank my advisors for giving me the opportunity to conduct this research, under their guidance, and for being extremely supportive and understanding when any circumstances interfered with my work. Other than being great supervisors, smart, intelligent, knowledgeable expert in vehicle dynamics and contact mechanics, they are also very nice and caring people. It has been a rewarding experience to work with them, and I will forever be grateful for everything they have done for me. In addition, I would like to show my gratitude to all the department's staffs for their comments, suggestions and help. Thank you as well to the colleagues and friends at the African Railway Center of Excellence. It was quite a privilege to work in such a cultural diverse environment.

Finally, I would love to express my utmost gratitude and love towards my family, especially my mother, for their stupendous support and encouragement towards finishing this thesis and produce quality research. Thank you to Mum and Dad for all you gave me and thanks to my brothers and sister for your unconditional support, I could have not been here without you.

ABSTRACT

The current trend of increased speeds and axle loads in the railway industry has led to accelerated wear of railway contact materials. This effect has brought with it new technological challenges including the monitoring and optimization of the wheel-rail interface parameters. For predictive maintenance purpose, railway vehicle wheel wear evolution models have been developed. These models are known to assume the wheel rotating on a rigid rail. However recent developments have found out that flexibility of the track plays an important role in wear evolution. On the other hand, track stiffness variation along the track is known to exist because of environmental conditions or transitions between slab and ballasted track or transition through railway level crossings, and it affects the track flexibility. The present research work investigates the influence of non-uniform track modulus and its spatial variation on the wheel-rail contact forces, stresses and wheel tread wear using dynamic explicit finite element analysis (FEA). The FE model consists of a quarter car running on a rail supported by three crossties. The modulus of elasticity of the crossties is calibrated to produce the actual strains in the rail during normal operation of a light rail, with a reference to Addis Ababa Light Rail Transit Service (AALRTS). In addition the crosstie modulus is used to resemble the total equivalent rail support system stiffness on the FE model. The rotating wheel is equipped with a dashpot suspension that supports the quarter railcar load. The stresses, forces, moments, contact areas, and slip velocities are extracted from the ABAQUS FEA model repetitively, at varying crosstie moduli ratio, using Python codes. These contact quantities are used to calculate the volume of material removal on the wheel tread using the Archard wear model. It was observed that an increase in crosstie modulus variation results in an increase of amplitudes of contact forces and the variations of their frequencies. Furthermore, high contact stresses were recorded at non-uniform track supports modulus. These factors influenced an increase in the volume of material removed on the wheel tread surface, at varying relative to uniform crosstie modulus. This research work intends to incorporate the spatial variation of the railway track stiffness into rail vehicle wheel tread wear prediction models. It leads to the development of better maintenance strategies and policies, which in-turn reduces the railway life cycle costs.

Key Words: Wear, Rolling Stock Maintenance, Track Infrastructure maintenance, Railroad Track Stiffness Spatial Variation, Track Stiffness, Life Cycle Cost, Contact mechanics, Track Stiffness/Modulus and Wheel-Rail Materials, wheel-rail interaction, explicit finite element analysis.

Table of Contents

Certification……..……..……...I
Declaration…….……..…...… II
Acknowledgement …….…..….. III
Abstract ……..…… IV
Table of contents …….…….. V
List of Figures…….…...VIII
List of Tables…….……XII
1 INTRODUCTION 1
1.1 Problem statement 3
1.1.1 General research questions 3
1.1.2 Specific research questions 4
1.2 Research objectives 4
1.2.1 General 4
1.2.2 Specific 4
1.3 Significance of the study 4
1.4 Scope/delimitation 5
1.5 Limitation 5
1.6 Thesis report chapters arrangement 5
2 LITERATURE REVIEW 6
2.1 Wheel-rail interaction 6
2.1.1 Wheel and rail material 7
2.1.2 Fundamentals of contact mechanics in railway engineering 10
2.1.3 Wheel-rail contact finite element analysis 16
2.2 Structures of the railway track infrastructure 17
2.2.1 Substructure 17
2.2.2 Superstructure 19

2.3 Railway track stiffness definition 19
2.4 Effects of railway track stiffness variation 20
2.5 Modelling of coupled train track dynamics 21
2.6 Experimental methods using strain gauges to determine strains in rails 22
2.7 Wheel-rail contact wear mechanisms and models 23
2.8 Conclusion 24
3 RESEARCH DESIGN METHODS AND VALIDATION OF COMPUTATIONAL MODELS 26
3.1 Validation methods of the wheel-rail contact finite element models 28
3.1.1 Validation of finite element static and rolling contact models using analytical solutions 28
3.1.2 Closed form solution of the 2D static contact mechanics problem. 31
3.1.3 Closed form solution of the 2D rolling contact mechanics problem 33
3.1.4 Simple roller on a flat plane FE model validation. 35
3.1.5 FE rolling contact analysis solution comparison with previous studies 40
3.2 Methods of equivalent track stiffness determination for finite element analysis models 41
3.2.1 Literature data of railway track web strains 43
3.2.2 Wheel-rail contact FE static model design and validation method 46
3.2.3 Validation of a 3D wheel-rail FE static contact model 51
3.2.4 Evaluation of the equivalent track stiffness 59
3.3 Finite element dynamic model design and validation method 61
3.4 Wear analysis 64
3.5 Conclusion 64
4 COMPUTATIONAL RESULTS: INFLUENCE OF NON-UNIFORM TRACK MODULUS ON WHEEL-RAIL CONTACT STRESSES, FORCES, AND WEAR 65

4.1 Normal contact forces and stresses variation with varying track stiffness ratio 65
4.2 Influence of non-uniform track stiffness on shear contact forces, shear stresses and moments. 78
4.3 Influence of track stiffness on wheel-rail slip parameters (i.e. slip velocity) 83
4.4 Track stiffness variation influence on wheel tread wear rate 83
4.5 Discussion of results 86
5 CONCLUSIONS AND FUTURE WORK 88
5.1 Conclusions 88
5.2 Recommendations 89
5.3 Future work 90
6 REFERENCES 91
7 APPENDIX 96

List of Figures

Figure 2-1. Diagrammatic representation of the wheel tread and railhead profiles after service operation. 7
Figure 2-2. (a) Cast iron rail sections covered with thick layers of rust due to rapid oxidation of cast iron. (b) Cast iron microstructure with lead as an alloy for altering the mechanical properties [15]. 8
Figure 2-3. The pearlite steel microstructure for rails. Light phase: Ferrite. Dark phase: Fe_3C [18] 9
Figure 2-4: Defined contact coordinate system (b) Deformed bodies after load application and contact terminology [24] 11
Figure 2-5: Stick-slip regions within the contact patch according to Johnson [26] 16
Figure 2-6: Substructure layers for a railroad track. Left: Ballast, sub-ballast and subgrade. Right: Typical thicknesses of substructure components [21]. 18
Figure 2-7: Principle of load transfer from the rail vehicle to the track foundation structures. ... 18
Figure 2-8: Rail superstructures 19
Figure 2-9: Winkler foundation using spring and damp for moving load in the railway road track [31]. 20
Figure 2-10: Railway track mounted with strain gauges[43] 23
Figure 3-1: Research design flowchart 27
Figure 3-2. The variation of the constants C_a, k and C_b with respect to values $B/A = R_2/R_1$ [51] for the case straight longitudinal contact surface profile, and straight transversal wheel contact surface profile. 30
Figure 3-3. Contact pressure distribution in the wheel-rail contact patch according to AALRTS vehicle parameters. 30
Figure 3-4: A plot of normal contact stresses (σ_{yy}) against longitudinal dimension of the contact patch for static analytical solution 33
Figure 3-5: Analytical plot of normal contact stresses (σ_{yy}) and surface shear stress (σ_{xy}) against longitudinal dimension of the contact patch for rolling contact analytical solution 35
Figure 3-6: Simple roller on a half plane Finite Element (FE) static and dynamic analysis model. 36

Figure 3-7: Coupling constraints definition in ABAQUS between the roller center reference point and the roller side surfaces. 36
Figure 3-8: Meshed roller on a half plane model. 38
Figure 3-9. Normal contact stress (σ_{yy}) distribution within the roller and the half plane in the FE static analysis. 38
Figure 3-10. Comparison of normal contact stress (σ_{yy}) and surface shear stress (σ_{xy}) against contact patch dimension. (a) A plot of static contact analytical and FEA results. (b) A plot of rolling contact analytical and FEA solutions. 39
Figure 3-11: Schematic diagram of the transient FE model according to Zhao [28] 40
Figure 3-12: Normal contact stress solution using various methods (Zhao 2011 [28]) 41
Figure 3-13: Surface shear stress distribution within the contact patch comparison of FE surface shear stress results with Hertzian and contact solutions [28]. 41
Figure 3-14. Railway track laying on an elastic foundation[54] 43
Figure 3-15. Strain measurements for insulated rail joints [56] 44
Figure 3-16. Calibration schemes for the strain-gauge section with: a) static force applied from the expanding device; b) static force applied to the cross beam of a loaded freight car; c) dynamic force applied from the special-purpose impact device [57]. 44
Figure 3-17. Relative strains against the vertical force applied to the rail (strain unit-parts per million, ppm) (Replotted from [57]). 45
Figure 3-18. UIC60 railway track profile (Dimensions in mm) 46
Figure 3-19. Crosstie dimensions (Dimension in mm) 47
Figure 3-20. ABAQUS FE static analysis model set up 48
Figure 3-21: Traction force application within the contact patch which is distributed in accordance with Eq. 3-3 49
Figure 3-22: Rail profile FE model solution for normal contact pressure distribution in the contact patch area in accordance with hertz theory (a) σ_{yy} results visualization for the whole model (b) Contact pressure distribution in the contact patch. 50
Figure 3-23: A plot of FE static contact pressure against the contact patch dimensions. Contact pressure distribution and contact patch dimensions are in accordance to the Hertz contact theory calculations. 51
Figure 3-24. Standard P8 railway vehicle wheel profile 52

Figure 3-25. P8 railway vehicle wheel 3D view and cross section along the wheel diameter. 52
Figure 3-26. 2D schematic diagram of a single wheel rolling on a rail 53
Figure 3-27: Couple and tie constraint application at the static model..... 54
Figure 3-28. A spring/dashpot was defined between the wheel center reference point and another reference point just above the wheel. As indicated by the red line in this diagram..... 55
Figure 3-29: Applied boundary conditions 56
Figure 3-30: Assembled and meshed ABAQUS FE model of a coupled quarter car train- track system with a fined mesh at contact points..... 56
Figure 3-31: Contour plot of a 3D wheel-rail static contact FE model results. The presented results are in MPa. 57
Figure 3-32: Validation of normal contact stress of a 3D static wheel-rail contact Finite Element model using comparisons with the Guler analytical solution procedure. 57
Figure 3-33: Validation of contact pressure of a 3D static wheel-rail contact Finite Element model using comparisons with the results obtained from Hertz contact theory solution procedure. 58
Figure 3-34: Location of rail track web strain data collection from the FEA solution (i.e. on nodes just above the middle crosstie and below the loading point). 60
Figure 3-35: Strain results for a train-track interaction model for a crosstie modulus of 500 MPa 60
Figure 3-36: A plot of crosstie modulus of elasticity versa vertical strains in the rail track web. 61
Figure 3-37: FEA dynamic model setup 62
Figure 4-1: ABAQUS 3D FE model displaying contact pressures..... 66
Figure 4-2: A plot of wheel-rail contact force magnitudes at each time increment in the rolling step and at varying crosstie modulus ratio. Railhead top surface normal contact force at varying crosstie modulus ratios (a) Above 1 and (b) Below 1. (c) Wheel normal contact force at varying crosstie modulus..... 67
Figure 4-3: A plot of contact force impact factor at varying crosstie modulus ratio. (a) Crosstie modulus ratios above 1. (b) Crosstie modulus ratios below 1. 68
Figure 4-4: (a) Visualization of normal contact forces fundamental frequencies at different crosstie modulus ratios. (b) A plot of normalized contact force amplitude against frequency spectrum at different crosstie modulus ratios 70

Figure 4-5: A plot of wheel-rail contact pressure at each time increment in the rolling step for various crosstie moduli ratios. (a) Crosstie modulus ratios above 1. (b) Crosstie modulus ratios below 1. 71
Figure 4-6: Geometry of the contact area and contour plots of contact pressure distribution (a) On the wheel tread and (b) Railhead top surface 72
Figure 4-7: Wheel-rail contact area at every time frame and at different crosstie modulus ratios 73
Figure 4-8: A plot of the total force magnitude due to contact pressure and frictional stresses (CFTM) against time 74
Figure 4-9: Total force magnitude due to frictional stress at every 0.000 seconds time increment at different crosstie moduli ratios. (a) Crosstie modulus ratio of 1 (b) Crosstie modulus ratio of 0.5 (c) Crosstie modulus ratio of 2.5 (d) crosstie modulus ratio of 0.2. 76
Figure 4-10: Plots of forces due to frictional stresses against time increments (a) in the x-direction (longitudinal) (b) in the y-direction (vertical) (c) in the z-direction (transvers). 77
Figure 4-11: Plots of the contact moments at each time increment. (a) Total contact moment magnitude plot. (b) A plot of contact moments about the z-axis. (c) A plot of contact moments about the y-axis. (d) A plot of contact moments about the x-axis. 79
Figure 4-12: Wheel shear stress at varying crosstie modulus ratios 80
Figure 4-13: Plots of shear stresses occurring on the wheel tread surface at different crosstie modulus ratio. (a) Ratio-1 and 0.143. (b) Ratio-1 and 2.5. 80
Figure 4-14: Plots of wheel shear force at varying crosstie modulus ratio. (a) Plots at various crosstie moduli ratios (b) Plots for crosstie modulus ratio-1 and 0.143 (c) Plots for crosstie modulus ratio-1 and 2.5. 82
Figure 4-15: Slip velocity plot at different crosstie modulus ratios 83
Figure 4-16: Wear chart for the wear coefficient, K based on laboratory measurements with wheel and rail steels(Taken from T. Jendel [61]) 84
Figure 4-17: Plot of wear volume at different crosstie modulus ratios (a) Plots of the volume of material removal at each time increment. (b) Plots of total volume of material removed on the wheel tread surface due to wear at different modulus ratios. 85

List of Tables

Table 3-1. Contact parameters in accordance to Addis Ababa Light railway transit system 29
Table 3-2: Parameters used in this study 32
Table 3-3: Roller and half plane geometry parameters..... 35
Table 3-4: Mesh specifications 37
Table 3-5. Material properties for Railway track UIC60..... 46
Table 3-6. Equivalent Properties for the rail track support structure (i.e. Crosstie Properties).... 47
Table 3-7: Addis Ababa Light Rail Transit Vehicle parameters 48
Table 3-8. P8 rail vehicle wheel material properties 52
Table 3-9: Mesh specifications in the contact region 56

1 INTRODUCTION

This chapter gives an introduction to the thesis research and the motivations behind the topic under research. An over view of the importance of researches on wheel-rail contact mechanics and railway vehicle dynamics is presented in the first section of this chapter. This is followed by an elaborate problem statement that, in accordance to the author's knowledge, needs to be addressed. Moreover the questions raised from the problem statement are noted down. Furthermore the limitations and scope of the research are provided as well as the potential contributions (i.e. significance) that this research can add to the railway industry. Lastly the arrangement of this thesis report is outlined.

INTRODUCTION

A large portion of railway life cycle cost (LCC) is distributed towards maintenance of failures associated with the wheel-rail interface and these include wear, fatigue, corrugation, ratcheting, fretting, delamination etc. A move towards more efficient, economic, environmental friendly, safe and sustainable railway systems is possible through optimization of the wheel-rail contact parameters which includes but not limited to wheel-rail material properties, the adhesion coefficient, the wheel and track geometries, track stiffness etc. which in-turn reduces the contact resistance, wear rate and fatigue crack initiation and propagation [1]. In the railway industry large quantities of energy consumption is distributed towards overcoming the friction and wear between the wheel-rail contact interface. The recent increase in traction power due to the development of more efficient power systems has resulted in a dramatic increase in axle loads and rail vehicle speeds which increases the wheel-rail wear and shortened fatigue life thereby reducing the wheel re-profiling and rail grinding intervals as well as increase the maintenance costs. The life span of both the wheels and the rails is also reduced which renders a reduction in the competitive advantage of the railways as a mode of transport.

The major root cause for the majority of mechanical failure mechanisms is due to the tribological characteristics of contacting surfaces [2]. Damages in the wheel-rail interface not only result in railway vehicle dynamic instability and poor riding comfort, but also reduced safety due to the increased risk of derailment. In order to minimize these risks numerous maintenance strategies have been developed since the dawn of railways and these are diagnostic maintenance approach, preventative maintenance approach and condition based maintenance approach. Diagnostic maintenance is maintenance which is done once failure has occurred and due to the catastrophic nature of the failures associated with railway systems and the increase in the human desire for comfort, safety, security, and awareness of dangerous operating conditions this approach had become obsolete [3]. Preventative maintenance is based on scheduled maintenance periods regardless whether failure has occurred or not. This maintenance strategy has been successful in the railway industry but it is still associated with risks of catastrophic failure if the maintenance interval is not well optimized. The unpredictable nature of the damage trend of some mechanical components [4] makes it cumbersome to prescience future failures and prescribe an optimum inspection and maintenance interval, therefore condition based maintenance approach is currently under research to overcome the risks associated with both diagnostic and preventative maintenance approaches. In order to apply condition based maintenance for both the rolling stock and the track infrastructure it is crucial to have a deeper fundamental understanding of the factors that influence the wheel-rail failure mechanisms.

The railway transportation system has gained a considerable amount of attention over the past few decades due to its high levels of safety, energy efficiency, reliability and huge hauling capacities relative to other modes of land transport. The uniqueness of the railway mode of transport is brought about by the unique characteristics of the wheel-rail contact. Contact forces that carry the train load are transmitted in a very small contact area (approximately 1 cm^2) between wheel and rail. The low adhesion coefficient between the steel to steel contact of the wheel and rail gives the railways its energy efficiency characteristics but it also restricts the tractive effort. The open nature of the wheel-rail contact system introduces a wide range of operating parameters and conditions that influences the wear and damage of both rolling stocks and track infrastructure components. Some of these factors includes axle loads, the type and form of third body materials present on the wheel-rail interface, train speed, track and wheel geometry, track and wheel material type and properties, the environmental conditions [5] etc. In addition the spatial variation of the railroad track stiffness and modulus also influences the wheel-rail contact forces and stresses which in-turn influences the damage trend.

This study is therefore aimed at investigating the influence of railroad track stiffness spatial variation on wheel tread wear. Firstly the influence of track stiffness variation on the wheel-rail contact

parameters was analyzed. This was followed by a comparison between contact parameters at constant track stiffness and varying track stiffness. A Finite Element Analysis simulation software package, ABAQUS was be utilized in this study. The Archard wear model was used to calculate the material removal volume on the wheel tread.

1.1 Problem statement

The railway track modulus provides a measure of the vertical deflections and vibrations of both the railway track and its foundation components. For civil infrastructure maintenance and management a high track modulus results in less track vibrations and deflection, therefore good track conditions. On the other hand stiff track modulus results in high wheel-rail impact forces and accelerate the wear of both the wheel and the rail, which is a major concern for rolling stock maintenance and management. Furthermore, the track modulus varies along railway networks due to different compaction level of track foundation components, fastener stiffness, different soil types, different sleeper spacing, environmental conditions, transitions points from blasted track to level crossings and bridges etc. The track modulus influences the level of track flexibility and track flexibility is known to have an effect on wheel-rail contact parameters. Several researcher i.e. [6], [7] [8] have studied the influence of track flexibility on wheel-rail contact behavior, however they assumed a uniform track modulus. The current study tries to incorporate the track modulus non-uniformity in track flexibility studies. In this study the influence of track flexibility and its variation along a track network will be included in wear calculations. Both the terms track stiffness and track modulus will be used interchangeably to mean the total equivalent track structure flexibility, in this study. The effects of the degree of the track modulus non-uniformity on both rolling stock and track components needs to be investigated for the development of better maintenance strategies and policies. Moreover, an understanding of the influence of railway track modulus non-uniformity on contact quantities and wheel tread wear can improve the railway vehicle wheel wear prediction models. In addition the railroad track modulus variation needs to be reduced in order to achieve better track performance at the same time flexible enough to reduce the wheel-rail contact stresses and prolong the life span of both wheels and rails at a reduced life cycle cost.

1.1.1 General research questions

“How does the non-uniformity of the track modulus influence the wheel-rail contact parameters such as contact area, forces, stresses as well as the wear and damage patterns of the rolling stock wheel tread?”

1.1.2 Specific research questions

- What is the estimate average rail track web strain of a light rail such as the one of Addis Ababa Light Rail Transit Service?
- How does the wheel-rail normal contact stresses/forces, contact force impact factor, contact area, shear contact stress etc. vary with variation in track modulus?
- How is the wheel tread wear affected by the variation in track modulus?
- To what extent does the knowledge of the influence of track stiffness variation improves the rail vehicle wheels maintenance approaches?

1.2 Research objectives

This study focuses on investigating the influence of non-uniform track modulus on wear of rail vehicle wheel tread. ABAQUS simulation software and Python scripting packages was utilized.

1.2.1 General

"To investigate the influence of track modulus non-uniformity on the wheel tread wear"

1.2.2 Specific

- To estimate the average rail track web strain based on previous researches involving railway track web strains measurements using strain gauge.
- Calibration of the railway track modulus into a Finite Element (FE) model in terms of track support material modulus of elasticity.
- To validate a rolling contact FE model using closed form analytical solutions.
- To determine the wheel rail contact stresses and forces using finite element method.
- To determine the effect of track stiffness variation (or track non-uniformity) on wheel-rail contact parameters.
- To determine the effect of track stiffness variation on wheel tread wear.
- To suggest improvements on rail vehicle wheels maintenance by including track modulus variation in maintenance planning and strategizing.

1.3 Significance of the study

Successful completion of this study will provide a fundamental understanding of how the track modulus non-uniformity influences wheel-rail contact parameters and the wear and damage of railway vehicle wheels. This research can provide measures to reduce the variation of the track modulus and ensures better track performance as well as good rolling stock dynamics. Better wear prediction models

can also be developed which includes track modulus non-uniformity. Furthermore, better maintenance strategies can be developed based on the results of this research. The competitive advantage of railways over other modes of transports can be improved through a reduction is failure risk and improved safety.

1.4 Scope/delimitation

This study is a combination of railway vehicle dynamics, contact mechanics and material science. Computer based simulations were conducted to fulfill this research investigation. The forces acting on the wheel-rail interface during the train service will be analyzed through simulations. The main concentration of this study is the wear of the wheel tread under varying track support flexibility.

1.5 Limitation

This study is not focused in the individual contribution of the railway track infrastructure components to the total track stiffness. Instead an equivalent track stiffness is determined and used in the simulations. Track settlement and other forms of track damage mechanisms are not part of this study. Temperature effects in the wheel-rail interface at non-uniform track modulus where not taken into consideration in this study.

1.6 Thesis report chapters arrangement

The first chapter of this thesis report was the introduction to the topic under research. The problem statement and research questions to be addressed were also introduced in CHAPTER 1. A literature review of past researches on wheel-rail contact mechanics and tribology is in CHAPTER 2. Furthermore, materials used for wheel and rails as well as their mechanical properties and damage mechanisms are reviewed. CHAPTER 3 gives the research design and methodology. The validation of a finite element model to be used in the study is also provided. The design of a train-track rolling contact FE model is outlined in CHAPTER 3 as well. The Computational results and their discussions are presented in CHAPTER 4. Different graph plots of wheel-rail contact parameters at varying track modulus are shown. CHAPTER 5 is the research conclusions, recommendations and future work.

2 LITERATURE REVIEW

This chapter presents a review of past studies related to wheel-rail interface parameter such as materials properties, track stiffness and its variation etc., and their influence on the coupled train-track system performance. Furthermore, a literature review on failure mechanisms (i.e. wear, rolling contact fatigue, corrugation etc.) associated with the wheel-rail contact is highlighted. In addition Finite Element Analysis (FEA) models for wheel-rail rolling contact analysis are reviewed. Wear models used for railway vehicles wheel and railway tracks are also presented in this chapter.

2.1 Wheel-rail interaction

The wheel rail interface has been a field of research interest since the 1800s and it is still a major field of research today since mostly all the unique characteristics of the railway mode of transport are defined at that interface. Some areas of research on the wheel-rail interface includes contact mechanics, fracture mechanics, dynamics, tribology, noise and vibration, and mechatronic and active control [9]. One of the broadest area of study in the wheel-rail interface is contact mechanics which covers topics such as particle emission, non-destructive testing, rolling stock and track infrastructure maintenance as well as tribology. The major concern in researches on wheel-rail contact mechanics is to provide solutions to overcome the problems associated with wear, rolling contact fatigue [10] and other forms of damage so as to reduce the life cycle costs of railway systems. As an appropriate response to known stresses and failure mechanisms, the materials employed in wheels and rails were, and indeed still are, those steels whose predominantly pearlite microstructures containing hard cementite lamellae guarantee high resistance to wear and fatigue [11]. Figure 2-1 below depicts a railway vehicle wheel on a railway track in real operation. In addition a smooth shiny surface on the wheel tread and rail head is shown and it is mainly as a result of wear.

Figure 2-1. Diagrammatic representation of the wheel tread and railhead profiles after service operation.

The early focus on solutions to improve the durability and reduce the maintenance of railway wheels and rails was focused on providing harder materials [12] with high resistance to wear and longer re-profiling intervals, this was later found to have adverse effects on other railway vehicle performance parameters such as riding comfort and riding quality. Wheel-rail materials with high hardness values reduce the contact stiffness between the wheel and rail, which in-turn eliminates the damping characteristic of the wheels resulting in high sensitivity of the carbody to track excitations. With increased attention on railway mode of transportation as the solution to high levels of road congestion, large quantities of greenhouse gas emission and underutilization of land, the speeds and haulage capacities of the railway vehicles have increased drastically over the past few years [13]. Current focus on wheel-rail interface researches has been shifted towards challenges that are interdisciplinary combining the knowledge of communication and traction, rolling stocks and civil infrastructure. A combination of rolling stock and civil infrastructure knowledge in the analysis of the wheel-rail dynamic response will result in different conclusions on the material properties required to achieve better track and rolling stock performance. Another major focus that has recently emerged is concerned with optimization of wheel-rail parameters in order to achieve the ‘magic wear rate’ (i.e. a synchronous between the wheel-rail wear rate and the rate of formation and propagation of fatigue cracks).

2.1.1 Wheel and rail material

The early railways in the 1700s used cast iron rails which were found to be inadequate for passenger trains in the 1800s due to their poor fracture toughness, brittleness and high hardness values [14]. Cast

iron was also easy oxidized (Figure 2-2-2 (a)) which shortens its life span. To improve the mechanical properties of cast iron, alloys such as lead, manganese and later on carbon were added to form better wheel-rail materials such as Wrought iron and steel which have better fracture toughness, fatigue resistance and longer life spans but the one area where cast iron was found to have superior properties than other used metals was the wear resistance. Figure 2-2-2(b) shows the micro-constituents of gray and ductile cast iron.

(a)

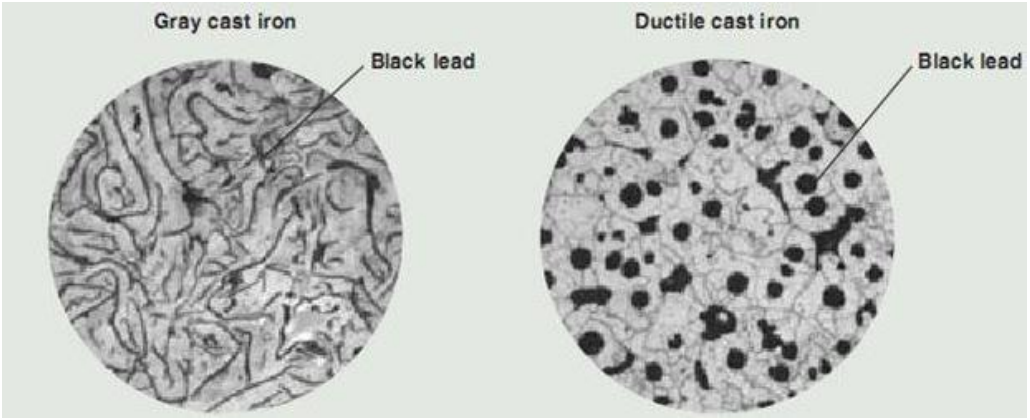

(b)

Figure 2-2. (a) Cast iron rail sections covered with thick layers of rust due to rapid oxidation of cast iron. (b) Cast iron microstructure with lead as an alloy for altering the mechanical properties [15].

In order to reduce the life cycle costs and increase the life span of railway tracks and rolling stock wheels, steel with pearlite microstructure was developed and is currently used in wheels and rails as of today. Railway vehicle wheels and rails are subjected to cyclic compressive forces, rolling forces, sliding forces and frictional forces etc. acting in a small contact patch, thus resulting in high contact stresses which causes wheel and rail plastic deformation as well as high induced contact temperatures. The presences of these extreme operating conditions is indicated by excessive wear rates, fatigue,

corrugation etc. Numerous studies have shown that the wear resistance of both rails and wheels is dependent on chemical composition, steel manufacturing process and associated hot forming process(s) [16]. Most rail steels used in japan, Europe and other countries has been manufactured from a low-alloy, carbon-manganese steel with medium to near-eutectoid levels of carbon the primary reason being the low cost of these steels and moderate wear resistance. The normal structure is pearlite with a varying degree of pro-eutectoid (PE) ferrite at the prior austenite (PA) grain boundaries; with higher carbon grades the percentage of PE ferrite will be very low and, in some recent grades, non-existent [17].

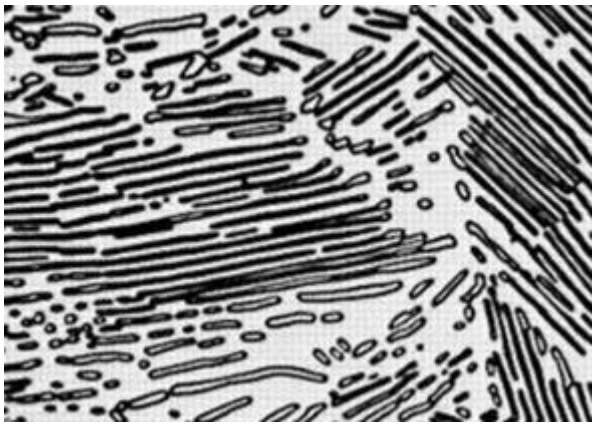

Figure 2-3. The pearlite steel microstructure for rails. Light phase: Ferrite. Dark phase: Fe_3C [18]

The most commonly used rail steel is pearlite steel as mention earlier, it consist of alternating lamellae of ferrite and cementite (Fe_3C) as shown in in Figure 2-3. Pearlite steel has high resistance to wear, low response of mechanical properties with temperature, good weldability and sound strength and ductility. However pearlite steel has poor Rolling Contact fatigue (RCF) resistance properties. To improve the RCF properties of pearlite steel more carbon content is added and the distance between cementite lamellae is reduced [19]. Bainite steel has drawn more attention as a potential alternative for pearlite steel rails since it has a very low carbon content and possess all the qualities of pearlite steel together with superior RCF resistance properties [15]. The wide range of Bainite steel behavior under different contact and operating conditions makes it cumbersome to predict its damage trend therefore it has hindered its application in railways.

The chemical composition of wheel and rail materials are depended on the standard being used and these includes but limited to the UIC-860-01986-2008, EN 13674-1 2006, UIC-860-01986-2008, Arema 2006 [20] etc. The differences in mechanical properties of wheels and rails are as a result of the different manufacturing processes and heat treatment procedures used. In the manufacturing process of railway vehicle wheels firstly casting is performed to form solid steel cylinders. Upon casting completion the steel cylinders are reheated to a temperature of $1500\ ^0F$ and they are pressed

fitted into a template with the required diameter and rim thickness. The center of the wheel is punched to make the axel hole [21]. The flange shape of the wheel is made from a spinning process. The dimensions of the central hole are also fine-tuned by the spinning process. To remove undesired residual stress the wheel is then heat to austenitizing temperature and once the wheel is homogenized, the rims are quenched with water spray on the tread surface. Rim quenching wheel provides the required material microstructure which ensures that adequate strength level of steel, wear resistance and compressive residual hoop stress in the rim are achieved. The microstructure formed depends on the cooling rate of the wheel tread and the time prescribed for the water spray quench process to finish. Water spray quenches the hot outer wheel rim which then cools and shrinks as a result a compressive stress in exerted on the hot inner rim. The wheel is then tempered at a temperature of $950\ ^{0}F$ to reduce the compressive residual stresses to the desired level. During this phase, the inner yielded rim and upper plate are constrained by the cooler outer rim. This results in the lower part of the rim and the plate starting in tension while the wheel tread is in the compression. Then the wheels are exposed to ambient conditions as they cool to room temperature. This heat-treatment results in the beneficial circumferential residual compressive stresses in the wheel rim. These compressive stresses are known to help prevent the formation of rim fatigue cracks in railroad service and thus are important to wheel safety [22].

In addition to the circumferential residual compressive stresses, the wheel and rail heat treatment processes also provides a material damping property that assist in damping the high cyclic loads involved in wheel-rail contact[23]. A coupled influence of material damping and track stiffness variation on wheel-rail contact forces as well as wear is not part of this study, but will be investigated in the future.

2.1.2 Fundamentals of contact mechanics in railway engineering

The field of contact mechanics always comes into play whenever the study of railway vehicle dynamics is in question. This is mainly because the most basic principle of applying and transferring loads is through contact and stress concentrations in the vicinity of the contact locations are crucial in the design of mechanical components which involves relative motion. Contact mechanics is studied in two different aspects of vehicle dynamics depending on the area of interest. If the vehicle response to the track excitation is of interest, then the normal and tangential contact forces acting at the wheel-rail interface must be computed. On the other hand, if the wear and damage mechanisms of the wheel and rail surfaces is of interest, then the contact pressure maximum magnitude, the contact pressure distribution, the contact area dimensions and the location of contact points are to be calculated.

a. The contact problem

When two bodies are in contact the nature of the contact can be explained in two ways, conforming and non-conforming contact depending on how well the contacting points fit with each other. A contact is said to be conforming when the contact bodies fit exactly without deformation. Non-conforming contact is when the initial contact of two un-deformed bodies brought together is either a point contact or line contact. The contact characteristic of a new wheel and rail is non-conforming. In non-conforming contact, a contact area is developed in the contact interface when a load is applied. The dimensions of the contact point, the maximum contact pressure and its distribution in the contact area are dependent on the magnitude of the load applied.

The normal contact problem of two contact bodies is characterized with the determination of the area under contact and the distribution of pressure within this area. To address this problem several aspects of the material in contact have to be known and assumption made. The contact bodies can be considered as rigid bodies or elastic bodies. In the study of railway vehicle dynamics and contact mechanics, both the wheel and the rail are regarded as elastic deformable bodies. Figure 2-4 shows the configuration of two elastic deformable bodies in contact, taken from a study conducted by Sichani [24] on wheel-rail contact modelling in vehicle dynamics simulation. The surfaces of the two contacting bodies are represented by the functions $z_1(x, y)$ and $z_2(x, y)$, for the first and second body respectively as shown in Figure 2-4. The origin of these functions is at the initial point contact of the bodies.

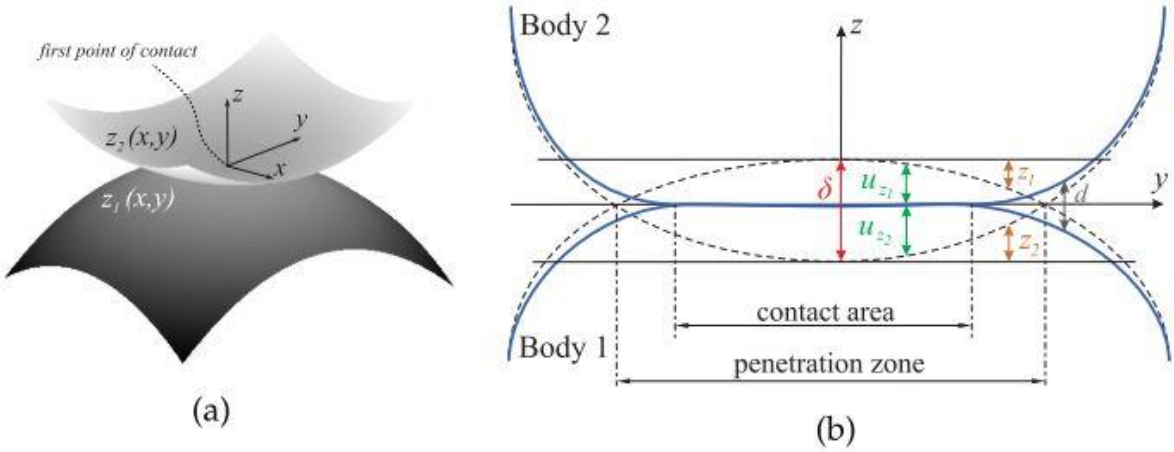

Figure 2-4: Defined contact coordinate system (b) Deformed bodies after load application and contact terminology [24]

After the bodies are pressed against each other, (like the wheel pressing on a rail) the centers of the two bodies move towards each other through a distance of δ, known as the approach. The separation,

is the distance between the un-deformed surfaces and it is calculated as $z(x,y) = z_1(x,y) + z_2(x,y)$. The sum, $U_Z(x,y) = U_{Z1}(x,y) + U_{Z2}(\mathrm{x},\mathrm{y})$ is known as the normal elastic deformation. Using the quantities described above, the distance between the deformed surfaces at any particular point within the coordinate system can be denoted by the function,

$$d(x,y) = z(x,y) - \delta + U_Z(x,y) \qquad \text{Eq. 2-1}$$

Using Eq. 2-1, the contact area can be defined using the following contact inequalities.

$$If \quad d(x,y) = 0 \qquad p(x,y) = -\sigma_z > 0 \qquad then\ (x,y)\ \epsilon\ C \quad and \qquad \text{Eq. 2-2}$$

$$if, \qquad d(x,y) > 0 \qquad p(x,y) = -\sigma_z = 0 \qquad and\ (x,y) \notin C$$

where,

$d(x,y)$ is the distance between deformed surfaces

σ_z is the normal contact pressure

$p(x,y)$ is the contact pressure disdtribution function

C is the contact area set of coordinates

Ignoring the molecular attraction (i.e. tension force) between the atoms of the two bodies in contact, the contact pressure can only be compressive [25]. A normal contact solution is the one which can satisfy both equation, Eq. 2-1 and the inequality in Eq. 2-2. This is where the name Heinrich Hertz emerge in contact mechanics. Hertz was the first scholar to find and publish a closed form solution of elastic deformable bodies in static contact.

b. Hertz contact theory

Hertz normal contact pressure solution for elastic bodies in contact includes these assumptions [26]:

- The bodies in contact are homogeneous, isotropic, and linearly elastic.
- The bodies are assumed to be perfectly smooth (i.e. Frictionless contact).
- The bodies can be considered as half-spaces in the vicinity of the contact (i.e. non-conformal contact)

Hertz observed that the problem in elasticity is analogous to one of electro-static potential. He noted that a charge, whose intensity over an elliptical region on the surface of a conductor varies as the ordinate of a semi-ellipsoid, gives rise to a variation in potentia1 throughout that surface which is

parabolic. By analogy, Hertz proposed that the pressure distribution within the contact area to be elliptical with semi axes a and b. The ellipse is given by the equation:

$$p(x,y) = p_o\sqrt{1-\left(\frac{x}{a}\right)^2-\left(\frac{y}{b}\right)^2} \qquad \text{Eq. 2-3}$$

p_o is the maximum contact pressure at the origin (i.e. the initial contact point) and its integration over the contact area is supposed to be equal to the applied static force. Therefore p_o can be calculated by the equation:

$$p_o = \frac{3N}{2\pi ab} \qquad \text{Eq. 2-4}$$

Hertz defined the separation as $z(x,y) = Ax^2 + Bx^2$

where,

A and B are the longitudinal and lateral curvatures respectively defines as:

$$A = \frac{1}{2}\left(\frac{1}{R_{1y}}+\frac{1}{R_{2y}}\right) \quad and$$

$$B = \frac{1}{2}\left(\frac{1}{R_{1x}}+\frac{1}{R_{2x}}\right),$$

where R_{1x} and R_{2x} are the transversal radii of the contact surface profile of body 1 and boddy 2 respectively, R_{1y} and R_{2y} are the longitudinal radii of the contact surface profile of of body 1 and body 2 respectively.

The semi axes a and b are dependent on the force applied and the geometry of the contacting bodies. Firstly an intermediate parameter θ is defined as:

$$cos\,(\theta) = \frac{|A-B|}{A+B} \qquad \text{Eq. 2-5}$$

θ is then used to find the Hertzian coefficients, m, n and r, by using pre-calculated tables [26]. The semi-axes of the contact patch are then given by:

$$a = m\left(\frac{3}{4}\frac{N}{E^*}\frac{1}{A+B}\right)^{1/3}, \qquad \text{Eq. 2-6}$$

$$b = n\left(\frac{3}{4}\frac{N}{E^*}\frac{1}{A+B}\right)^{1/3},$$

$$\delta = r\left(\left(\frac{3}{4}\frac{N}{E^*}\right)^2 (A+B)\right)^{1/3},$$

where,

$$\frac{1}{E^*} = \frac{1-{v_1}^2}{E_1} + \frac{1-{v_2}^2}{E_2},$$

E_1, E_2 and ν_1, ν_2 are the elastic moduli and Poisson's ratios of the bodies in contact respectively.

c. Rolling contact mechanics

Johnson [26] defined rolling as the relative angular motion between two bodies in contact about an axis parallel to their common tangent plane. Two distinct frames of references are defined in rolling contact mechanics, the Lagrangian and the Lagrangian-Eulerian. The Lagrange frame of reference moves with the point of contact moves while the Lagrange-Eular frame of reference remains stationary. Two bodies in relative rolling motion can move with velocities V_1 and V_2 and also angular velocities ω_1 and ω_2. If the velocities V_1 and V_2 are not equal a kinematic quantity called slip velocity (i.e. Sliding occurs) is defined. It is the relative velocity of two points from different objects in contact. Spin is created when the angular velocities of the bodies in relative rotational motion are unequal. Pure rolling contact is when the sliding and the slip are zero, while partial slip rolling contact is when the contact area is divided between the pure rolling region (i.e. stick region) and the sliding region (i.e. slip region). The partial slip rolling contact is the rolling motion which is mostly characterized at the wheel-rail interface.

The Spin and Slip are mostly due to the rigid-body motion and elastic deformation of the bodies in contact. The contribution of the rigid body motion to sliding and slip are as shown in Eq. 2-7 [24].

$$\Delta v_x = v_{x1} - v_{x2},$$

Eq. 2-7

$$\Delta v_y = v_{y1} - v_{y2},$$

$$\Delta\omega_z = \omega_{z1} - \omega_{z2}.$$

The elastic contribution to the relative velocities is given by Eq. 2-8:

$$\dot{u}_x = -V\frac{\partial u_x}{\partial x} + \frac{\partial u_x}{\partial t}, \qquad \text{Eq. 2-8}$$

$$\dot{u}_y = -V\frac{\partial u_y}{\partial x} + \frac{\partial u_y}{\partial t},$$

where,

$$u_x = u_{x1} - u_{x2},$$

$$u_y = u_{y1} - u_{y2}, \qquad \text{Eq. 2-9}$$

And V is the rolling speed. The slip can be written in the longitudinal and the lateral direction as,

$$s_x = \Delta v_x + \Delta\omega_z y - V\frac{\partial u_x}{\partial x} + \frac{\partial u_x}{\partial t},$$

$$s_y = \Delta v_y + \Delta\omega_z x - V\frac{\partial u_y}{\partial x} + \frac{\partial u_y}{\partial t}.$$

The longitudinal and lateral creepages are defined as the relative velocities of the rolling bodies in contact divided by the rolling velocity (See Eq. 2-10).

$$v_x = \frac{\Delta v_x}{V}, \qquad \text{Eq. 2-10}$$

$$V_y = \frac{\Delta v_y}{V}.$$

respectively, while the spin is defined as,

$$\varphi = \frac{\Delta\omega_z}{V}.$$

d. Partial slip rolling contact

Rolling motion can be classified as free rolling and tractive rolling depending on the whether there is a driving force or not. Tractive rolling in railways is when there is traction force or a braking force applied to the wheels. As defined earlier partial slip involve the distribution of sliding and pure rolling within the contact area. At pure rolling the slip area is zero within the contact patch and it increase

with increase in tractive force, starting from the trailing edge of the contact area, progressing forward to the rear parts of the contact area. The limiting value of the tractive force is defined by a traction coefficient which is described by the inequality in Eq. 2-11

$$0 < \frac{Q}{\mu P} \leq \mu, \qquad \text{Eq. 2-11}$$

where,

$Q\ (i.e.q(x))$ is the tractive force, $P\ (i.e.p(x))$ is the normal force and μ is the coefficient of friction.

The distribution of the stick and slip areas within the contact area of two bodies in rolling contact is as shown in Figure 2-5 below. The contact ellipse dimension in the rolling direction is donetated by $2a$.

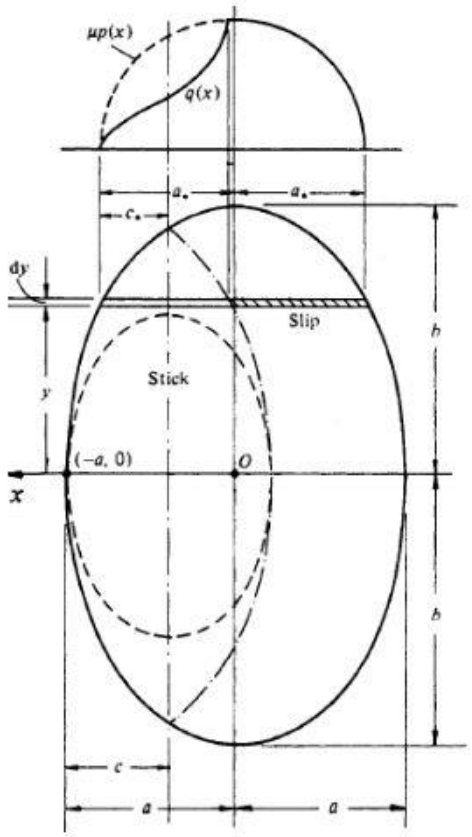

Figure 2-5: Stick-slip regions within the contact patch according to Johnson [26]

2.1.3 Wheel-rail contact finite element analysis

A number of solution procedures for the wheel-rail contact problem have been proposed by different scholars from time to time. Among those solutions is the CONTACT software for railway vehicle dynamics simulation by Professor Kalker and the FASTSIM algorithm for the simplified theory of rolling contact. Kalker was also the first to obtain the so called full solution of rolling contact but it

was still based on the half space assumptions and limited to homogenous materials. Vermeulen-Johnson also developed a theory for 3D rolling contact analysis but it was still limited to small spin values and a short contact area distance in the rolling direction.

The Finite Element Method (FEM) was developed to overcome the shortcomings of the former methods. Anisotropic material properties can be taken into consideration when studying contact mechanics of surfaces used FEM. The FEM is a numerical method of solving partial differential equations be decomposing them in to sets of algebraic equations. Large engineering models with complicated geometries can be analyzed using the FE technique.

Arslam and kayabasi [27] studied the 3D wheel-rail contact using Finite Element Analysis (FEA). In their study they validated the FEA results of wheel-rail contact analysis with field results and commented in the applicability of FEM to contact modelling. It was found that the FEA results matched well with the results observed in the field. Zhoa and Li [28] conducted a 3D transit finite element analysis of frictional wheel-rail rolling contact. A wheel and a railway track were modelled with simplified geometry using an FEA software package ANSYS. The frictional rolling contact of a railway vehicle wheel on the rail was validated for both the normal and the tangential solutions using results from the CONTACT software and the Hertz theory. The authors concluded that the FE model is a valid and promising tool for the solution of frictional rolling contact, in statics and dynamics, in elasticity and plasticity. Furthermore, Zhao and Li [29] also conducted a research in the influence of velocity on the dynamic friction coefficient using the FEM. The results proved the negligible effect of normal forces on the change of the dynamic friction coefficient with velocity. Focus was said to be put on the tangential solution when studying the friction characteristics in the contact patch. The efficiency of FEM in obtaining detailed results of rolling contact was proven in that paper (Zhao and Li 2016).

2.2 Structures of the railway track infrastructure

The most commonly used forms of railway tracks are the ballasted track and the slab track. Addis Ababa Light Rail Transit System uses the ballasted track form which is divided in to two sections the substructure and the superstructure. This subsection gives a detailed elucidation of the parts of both the substructure and the superstructure as well as their contribution to track stiffness variation. Numerical models used to study the railroad track dynamics are also provided.

2.2.1 Substructure

The substructure is the foundation of the railway track infrastructure and it consist of the ballast, sub-ballast and the subgrade. The order of arrangement of the substructure us as shown in Figure 2-6 and Figure 2-7. Ballast is made up of coarse-sized, angular-shaped, non-cohesive and uniformly graded

granular material. It is used to provide stability and resilience and to distribute the load from the track superstructure to the subgrade. Further, it should allow for drainage and alleviation to frost, as well as adjustment of track geometry. The subgrade should provide a stable foundation for the sub-ballast and ballast layers, while the sub-ballast is an intermediate granular layer to prevent the intermixing of ballast and subgrade. It is concluded that the most important parameters affecting the degradation of track geometry at a given site are the characteristics and quality of the substructure, track drainage, ballast, track components and rail surface. For example, to provide conditions for maximum durability in track geometry, the substructure needs to be as homogeneous as possible with a uniform resistance to dynamic loads. Further, the rail surface needs to be free of irregularities (rail corrugation, rolling contact fatigue defects, joints, etc.) inducing dynamic loads, and the ballast must allow for a good drainage.

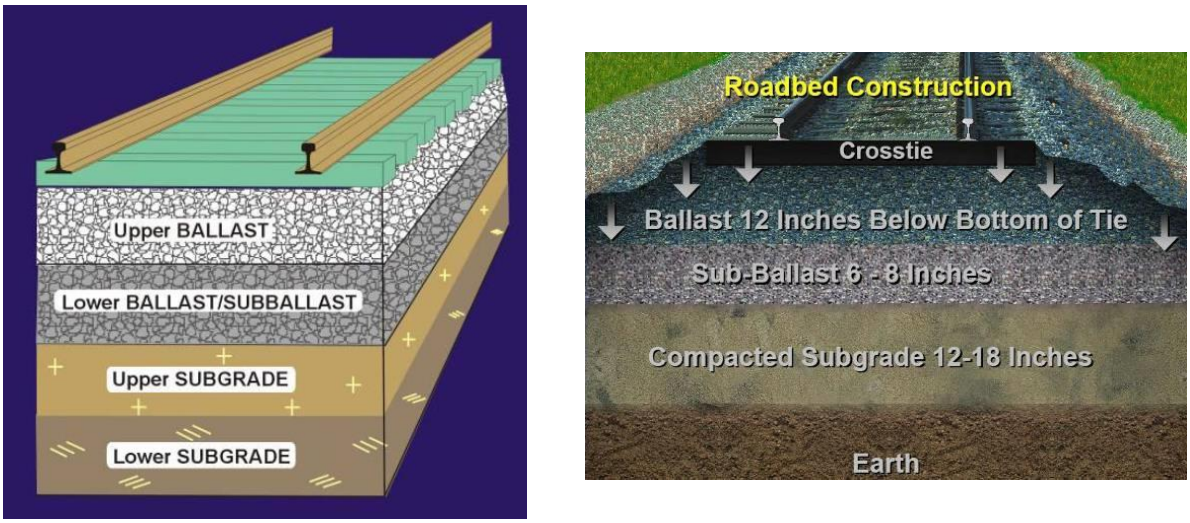

Figure 2-6: Substructure layers for a railroad track. Left: Ballast, sub-ballast and subgrade. Right: Typical thicknesses of substructure components [21].

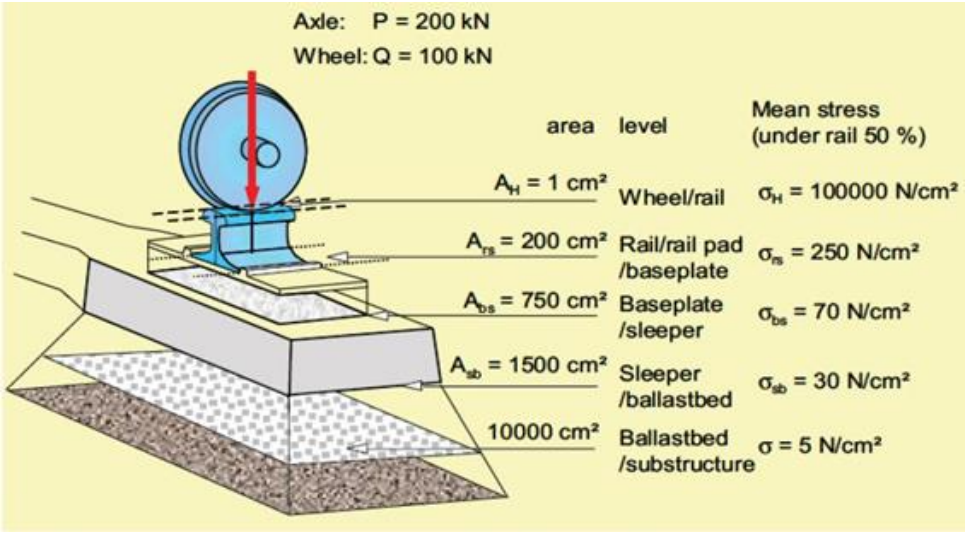

Figure 2-7: Principle of load transfer from the rail vehicle to the track foundation structures.

2.2.2 Superstructure

The superstructures of railway track infrastructure includes fasteners, sleepers, rail pads and the rail itself, see Figure 2-8. The fasteners is the means of connection between the rail track and the sleepers. Fasteners maintain the rail gauge and fix the rail in position. The loads from the railway vehicle are transfer to the substructure through fasteners. Between the rail and sleep there is a rail pad which acts as a damper to reduce the transmission of unwanted dynamic excitations from the railway vehicle to the track substructures. Rail pads are also used to provide a gradual change in track stiffness when entering or exiting bridges for example. The use of rail pads for track stiffness smoothening can reduce the track stiffness variation which result in uniform track settlement and reduced impact loads.

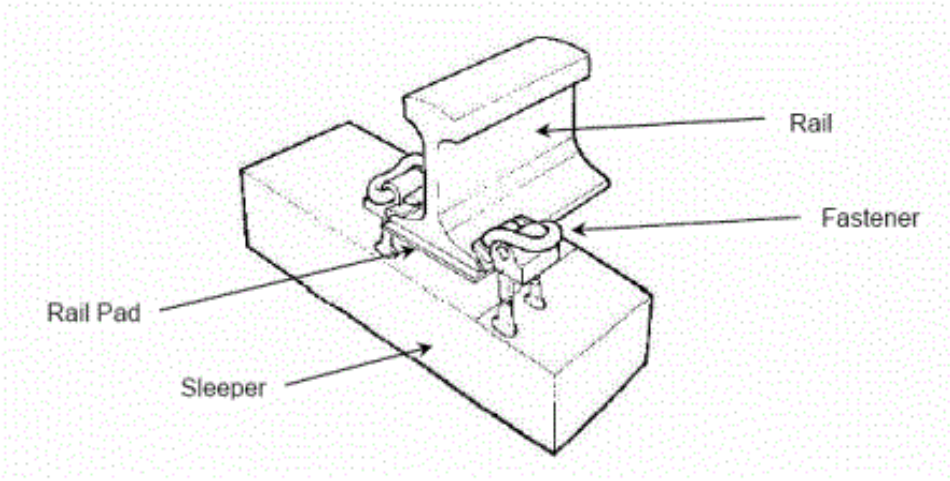

Figure 2-8: Rail superstructures

2.3 Railway track stiffness definition

Railroad track stiffness is a parameter of significant importance from the design, maintenance and construction point of view of railway infrastructure[8]. This parameter represent the basis for calculating the stresses in the elements of the railroad track and track foundation. Track stiffness influences the railroad track geometry deterioration processes, rail fatigue, superstructure and substructure settlement, rail corrugation etc. therefore understanding its real definition and impact on train-track dynamics is of utmost importance for the preservation of railroad vehicle wheels and track geometries.

Conventionally the railroad track system has been modeled as a beam laying on an elastic foundation of uniform stiffness and this is referred to as the Winkler's hypothesis. Winkler's Hypothesis assumes that the elastic foundation is a system of identical, independent, closely spaced, discrete and linearly elastic springs. Based on the Winkler's theory the railroad track stiffness can be defined at the proportion of the loads applied in a certain direction to the deflection experienced in that particular

direction at a certain point in time. The track stiffness can be vertical or lateral depending on the direction of loads applied and displacement. Another term track modulus is also used to refer to the vertical stiffness of the railroad track foundation [30].

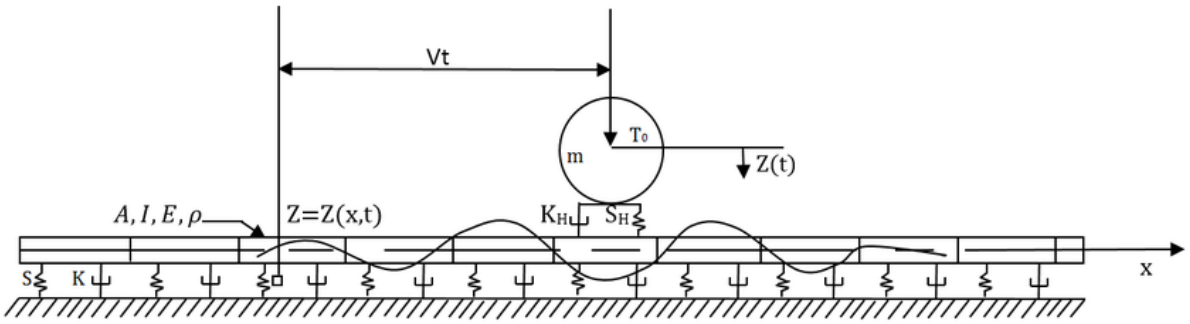

Figure 2-9: Winkler foundation using spring and damp for moving load in the railway road track [31].

The vertical track stiffness can be represented by as shown in Eq.1 where:

$D\ (t)$ vertical track stiffness Eq. 2-12

$Q\ (t)$ vertical loads

$Z\ (t)$ vertical track displacement

$$D(t) = \frac{Q(t)}{Z(t)}$$

This defined track stiffness is also referred to as static track stiffness since it is measured as a single point along the railroad track. Apart from track deflection the railroad track stiffness is also dependent on the excitation frequency induced by moving loads thus a railroad track stiffness definition that incorporates the frequency is necessary. The term dynamic stiffness can be used to describe this stiffness. Dynamic stiffness is usually used when dimensioning elastic elements of the railway track such as rail pads, under sleeper pads, ballast pads etc. Past researchers identified a lower static stiffness than dynamic stiffness [32].

To provide a more realistic model for wheel-rail dynamic interaction analysis non-linear and inelastic foundation models are introduced. The deflection of the foundation elements such as rail pads and ballast varies non-linearly with increasing loads and speeds. Therefore non-linearity of the track should be taken into consideration when studying the dynamic impact forces between the wheel and rail [31].

2.4 Effects of railway track stiffness variation

The railroad track stiffness variation is a common track irregularity that originates from either the superstructures (i.e. fasteners, rail pads, rails, sleepers etc.) or from substructures (i.e. subgrade, soil type, foundation etc.). Because of factors such as transition from slab track to ballasted track, non-uniformity of the ballast and subgrades, differences in rail pad stiffness along the track, different levels

of ballast compaction, different ballast thickness, different fastener forces, etc, railroad track stiffness varies spatially along the track. A dramatic variation of track stiffness in very short distances is usually due to substructure elements. Places along the track where track stiffness will change rapidly are for example at pile decks, embankments, bridges, transition zones, level crossings, turnouts, switches etc. Dahlberg [33] pointed out that the rate of degradation of track components and the rate of track settlement depends on the severity of the stiffness variation. Irregular track stiffness induces random wheel-rail contact forces as well as impact forces which catalyze track settlement, wheel-rail geometry deterioration, fatigue problems, cracks, wear, plastic deformation, hanging sleepers, and so on. High frequency vibrations are also a product of railroad track stiffness variation which results in noise transmission to the infrastructures within the vicinity of the railway track thereby reducing the quality of city life.

Frohling, Scheffel and Ebersöhn [34] studied the influence of the spatially varying track stiffness on the performance of the rail vehicle and the dynamic loading between the wheels and rails. It was concluded that the track stiffness variation has an insignificant effect on the riding quality however it is the major contributing factor for the dynamic loading of the track and the subsequent deterioration of both track and rolling stock components.

2.5 Modelling of coupled train track dynamics

Investigations on the track performance has utilized both coupled train-track static and dynamic simulations as well as field experiments. Tutumluer at el [35] studied the differential movement at railway transitions for high speed trains. It was pointed out in their research that differences in track system stiffness, track damping characteristics and foundation types are some of the main factors causing differential movement at railway transitions. A review of modelling railway track deterioration mechanisms was conducted by Ferreira and Murray [36]. In their research they defined a hierarchy of main categories of models which have been developed. On one hand, there are microscopic models which analyze railway system components such as rail stresses, ballast settlement etc. on the other hand, there are macroscopic models such as network analysis, maintenance planning, investment appraisal etc. In-between these two periphery models are a large number of models used to predict the deterioration behavior of railway components given the relationship between microscopic and macroscopic models. Kabo, Nielsen and Ekberg [37] studied the “dynamic train-track interaction and material deterioration in the presence of insulated rail joints”. A finite Element Analysis (FE) model was designed in ABAQUS constituting of rails, sleepers, rail pads and ballast. Uniform track support properties such as sleeper modulus, ballast stiffness and damping constants etc. were kept constant and it was observed that the surface irregularity introduced by the joint increased the contact loads

magnitudes and causes a dynamic excitation which leads to increased Rolling Contact Fatigue (RCF) in the regions near the joint. Berggren at el [38] identified the substructure properties of railway tracks by dynamic track stiffness measurement and simulations. It was pointed out that the vertical track stiffness differ in static and dynamic situations. The variation of vertical track stiffness due to substructure (i.e. all the track elements below the sleeper including the subsoil) properties variation was highlighted. An instrumented vehicle was used to conduct the dynamic track stiffness measurements using Neural Network and Relevance Vector Machine.

It has been shown in previous researches that the railway track vertical stiffness is an average of the both superstructures and substructures components vertical stiffness [39], [40], [41]. The first step in the study for the influence of railway track stiffness variation on the wear of the wheel tread is the determination of an equivalent track modulus. A finite element static analysis of a train-track interaction system was conducted in order to establish the averaged equivalent railway track vertical stiffness used in this study.

2.6 Experimental methods using strain gauges to determine strains in rails.

The strains is railway track web just like the vertical track stiffness can be measured experimentally at standstill and/or at rolling conditions. Four common methods are used namely, instrumentation, impact hammer, falling weight deflectometer (FWD) and a track-loading vehicle (TLV) [42]. The Instrumentation method is based on measured displacements and accelerations responses on sleepers and rails to the passage of a railway vehicle of known axle load. The vertical track stiffness can then be evaluated through load- deflection and load acceleration diagrams.

The impact hammer is a hand-held tool which is equipped with a device to measure the impulse load and it is used to hit either the sleeper or the rails in a controlled manner. The sleeper or rail is equipped with an accelerometer. The impulse of the hammer and the acceleration of the sleeper or rail are then evaluated. Investigations such as noise, vibrations and interaction forces between wheel and rail can be conducted using this method.

The falling weight deflectometer is another method that often is used in the road industry to measure vertical stiffness. However with small modifications it can also be used in the railway industry. A object of known mass is dropped on the rail head top surface and the deflections of the rail as well as the strains are recorded automatically by sensors (i.e. one of which is a strain gauge) at various distances along the rail. Lastly the track-loading vehicle method consists of a railway vehicle loaded to create force on the track with the help of hydraulic jacks.

Dynamic railway track web strains measurements depicts more accurately the real scenario of both rail deflections and strains during train operation, relative to standstill measurements. In addition the

railway operation is not interrupted and the experiments are time efficient. Tutumluer et al. [43] conducted experimental dynamic railway track web strain measurements on the differential movement at railway track transitions for US high speed trains. The authors experiment set up was as depicted in Figure 2-10, strain gauges were mounted on the railway web above sleepers and in-between sleepers after surface cleaning.

Figure 2-10: Railway track mounted with strain gauges[43]

2.7 Wheel-rail contact wear mechanisms and models

Two approaches of modeling wheel and rail wear have been developed over time through extensive theoretical and experimental studies[44]. The sliding contact wear modeling is based on the Archard's equation (Eq. 2-13) [45] and the rolling/sliding contact wear models uses the energy dissipation effect. The Archard's wear equation has been calibrated for use in the wear analysis of wheels and rails.

$$V = K\,\frac{Ns}{H}, \qquad \text{Eq. 2-13}$$

where K is the wear coefficient.

Wear manifests through different wear mechanisms on the surfaces of wheel and rail. The most common wear mechanisms occurring in the wheel-rail interface are delamination, adhesive, abrasive, corrosive and fatigue wear [46]. The evolution of the wheel and rail profiles is usually due to adhesive and abrasive wear. Railway vehicle wheel wear takes place in two forms, regular wear which refers to the change in the transversal profile, and irregular wear (i.e. out of roundness) of wheel which is the formation of periodic wear in circumferential direction of the wheel. These wear forms are usually treated separately due to the difference in contact conditions which results in each wear form. Regular

wear is more dominant in terms of wheel tread profile evolution which is produced by slowly varying values of the contact forces and slips in the contact area as a result of longitudinal and lateral wheelset motions [44]. In this study only the regular wear is taken into consideration.

Pearce and Sherratt [47] developed a program for wheel profile prediction during the wearing process. Good profile evolution prediction of P8 and P11 wheel profile were achieved through the use of the energy dissipation wear technique. Zobory [48] wrote a paper on the prediction of wheel-rail profile wear. It was pointed out that, the essential component of the dynamical analysis of railway vehicle is the description of the forces and moments transmitted on the wheel/rail contact points. Zobory also gave an explanation of the dissipated energy based wear hypothesis. This formulation states that the debris-mass-flow-density is proportional to the density of flow of energy dissipated on the contact surface. Defining the energy flow density $E_d\ (r_p\ , t)$ reflecting the specific energy loss due to sliding friction at a point with position vector r_p. Its unit of measure is Nm / (sm^2). In the course of rolling contact of two elastic bodies in the presence of dry friction, contact area is divided into two disjoint subsetsA_a, and A_s, namely the area of adhesion and area of slip, respectively. The energy flow density equation is given by:

$$E_d(r_p,t) = \begin{cases} \tau_x(r_p,t)\delta v_x(r_p,t) + \tau_y(r_p,t)\delta v_y(r_p,t) & for \quad r_p \in A_s(t) \\ 0 \quad for & r_p \notin A_s(t) \end{cases}, \qquad \text{Eq. 2-14}$$

where

$\tau_x\ and\ \tau_y$ are the tangential traction components arising at position r_p,

$\delta v_x\ and\ \delta v_y$ are the micro-slip-velocity components

The dissipated energy based wear hypothesis proportion then state that;

$$m_d(r_p,t) = k \times E_d(r_p,t), \qquad \text{Eq. 2-15}$$

where

$m_d(r_p,t)$ is the debris mass flow density at position r_p and

K is the wear coefficient.

2.8 Conclusion

In this chapter a review of literatures related to the wheel-rail contact mechanics, and damage mechanisms was done. To provide a better understanding on these phenomena, firstly an overview of wheel-rail materials and their impact on wear strength was given. This was followed by a section on the fundamentals of rolling contact mechanics in wheel-rail contact and railway vehicle dynamics. The Hertzian theory of contact mechanics was introduced in this section. In addition a brief review of other

methods used in solving the wheel-rail contact problem was provided. Furthermore, the application of FEM to wheel-rail contacts was reviewed. Since this study investigates the influence of railway track stiffness on wheel-rail contact parameters, a review of the railway track infrastructure components was inevitable, and Section 2.2 provide that. The definition of track stiffness was given in Section 2.3 and the factors that influences its variation are given in Section 2.4. This study involved modeling of a coupled track-track system, therefore a review of coupled finite element train-track systems is highlighted in Section 2.5. The stresses and strains occurring the rails and their methods of measurements are of important use in this research which is why a review of such information was carried out in Section 2.6. Last but not least Section 2.7 shows the wear mechanisms associated with the wheel-rail contacts and the wear models that have been developed over time by both scholars and industries, to quantify the volume of material removal due to wear.

3 RESEARCH DESIGN METHODS AND VALIDATION OF COMPUTATIONAL MODELS

This chapter provides a detailed set of steps to be followed to move towards achieving the aims and objectives of this thesis research study. Firstly the research design flowchart is presented followed by a literature data collection and our FE methods used for determining the equivalent track modulus. The literature data collection includes rail web strains which are to provide adequate input data for the Finite Element (FE) static analysis. The FE static analysis is used in the determination of an equivalent railway track modulus inform of crosstie modulus of elasticity. Moreover, detailed outlines of the static and dynamic finite element models are provided. Furthermore, the validation of finite element models using both analytical and a FE model consisting of a simple roller on a half-plane surface, is presented. A flow chart of the methods is presented in Figure 3.1

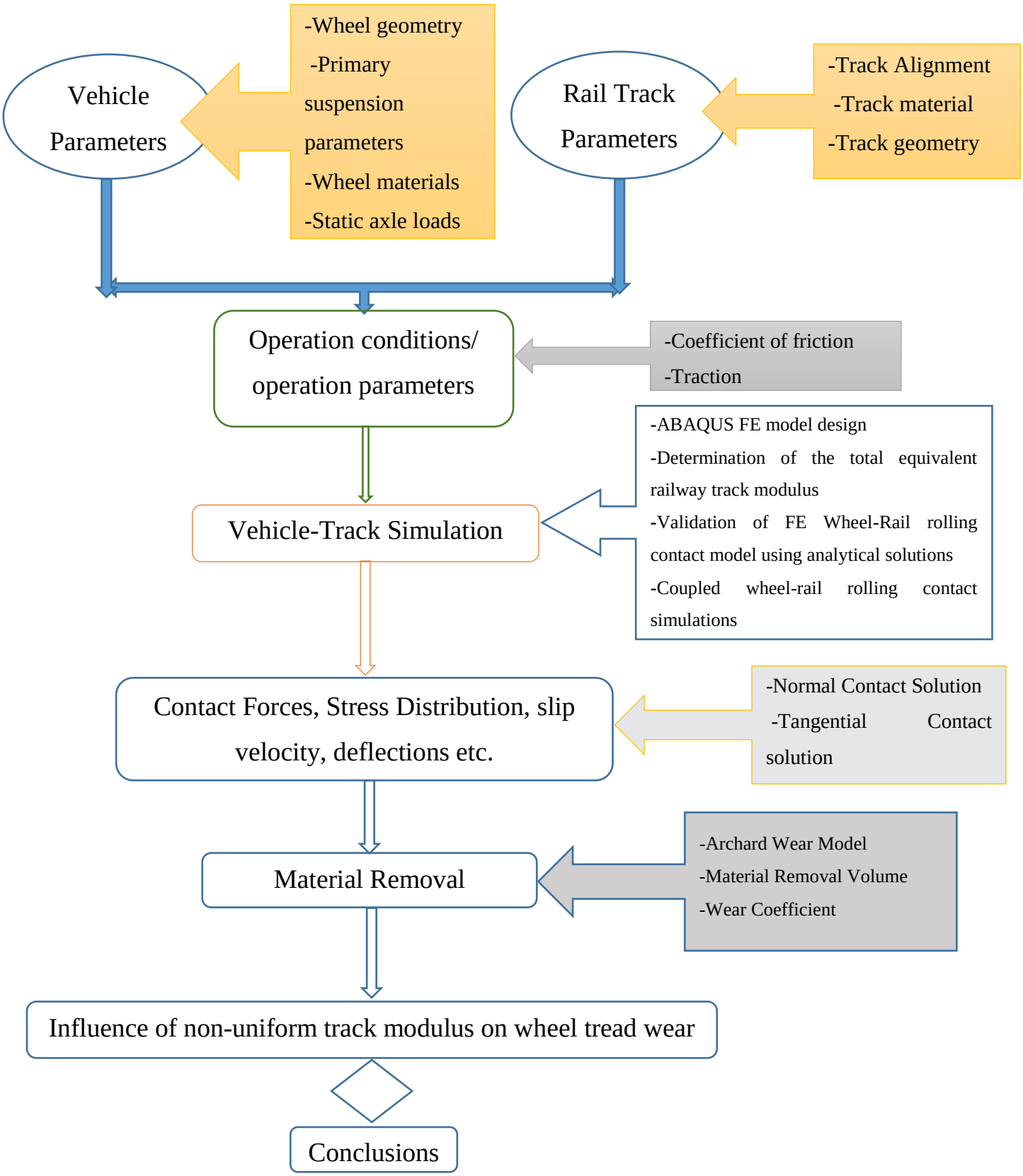

Figure 3-1: Research design flowchart

3.1 Validation methods of the wheel-rail contact finite element models

This section shows various methods to validate the Finite Element (FE) model which is used in this study. The model is validated in terms of mesh element type, mesh element size, model geometry as well as contact patch characteristics. The ABAQUS rolling contact analysis solution is also validated in this section. Firstly, using some of the railway vehicle parameter of Addis Ababa Light Rail Transit system vehicles a Hertzain contact analysis is carried out to establish the contact stress distribution curve as well as contact patch dimensions and geometry. This is followed by a presentation of closed form 2D analytical static and rolling contact solutions which are used to validate a simple roller on a half plane finite element model. Two analytical methods found from the literature, Guler's static contact analytical solution and Alinia's rolling contact solution, were used to validate the static and rolling contact FE models respectively. The FE model was based on the wheel and rail cross sectional dimensions at the point of contact for which a small thickness was assigned.

3.1.1 Validation of finite element static and rolling contact models using analytical solutions

a. Hertz theory

Wheel tread wear behavior is analyzed in this study therefore only a single point contact between the wheel tread and the railhead top surface is considered. Two point contacts which includes wheel flange and rail gauge corner contacts are out of the scope of this study. Due to the availability of the closed form solution of the Hertz contact problem, the Hertz contact theory was applied for both contact patch geometry and contact pressure distribution [49], [50]. The governing equation for the contact patch geometry according to Hertz contact theory solution is given by Eq. 3-1.

$$1 - \frac{x^2}{a^2} - \frac{z^2}{b^2} = 0, \qquad \text{Eq. 3-1}$$

where, a and b are the semi-axis of the elliptical contact patch.

A railway vehicle in motion is subjected to dynamic loads which differ from static loads because of the influence of railway vehicle speeds, wheel and rail geometries, track irregularities etc. A dynamic normal load was considered in the static analysis. The static loads are transformed into dynamic loads according to Eq. 3-2 [51]**,**

$$P_d = P_S + \theta P_S, \qquad \text{Eq. 3-2}$$

where;

P_d is the dynamic load,

P_S is the static load and

$$\theta = 0.33\frac{\upsilon}{D},$$

and

υ is the vehicle speed in miles/hours and,

D is the wheel diameter in inches.

According to the Hertz theory the contact pressure is semi-ellipsoidal distributed within the contact patch according to Eq. 3-3.

$$\sigma_y(x,z) = \sigma_{max}\sqrt{1 - \frac{x^2}{a^2} - \frac{z^2}{b^2}}, \qquad \text{Eq. 3-3}$$

where,

$$\sigma_{max} = \frac{C_a b}{\Delta}, \qquad b = C_b\sqrt[3]{P\Delta}, \qquad a = \frac{b}{k},$$

$$\Delta = \frac{2R_1R_2}{R_1 + R_2}\left(\frac{1 - {\upsilon_1}^2}{E_1} + \frac{1 - {\upsilon_2}^2}{E_2}\right).$$

Table 3-1. Contact parameters in accordance to Addis Ababa Light railway transit system

Rail head contact surface radius, R_1	**360** mm
Wheel radius, R_2	380 mm
Wheel material poison ration, *v2*	0.3
Rail material poison ratio, *v3*	0.3
Wheel material modulus of elasticity, $\boldsymbol{E_1}$	2×10^5 MPa
Rail material modulus of elasticity, $\boldsymbol{E_2}$	2×10^5 MPa
$\boldsymbol{P_S}$	68670 N
$\boldsymbol{\upsilon}$	8.4 m/s = 18.79 mph
$\boldsymbol{P_d}$	71 056.09 N
$\boldsymbol{D}$	29.92 inches

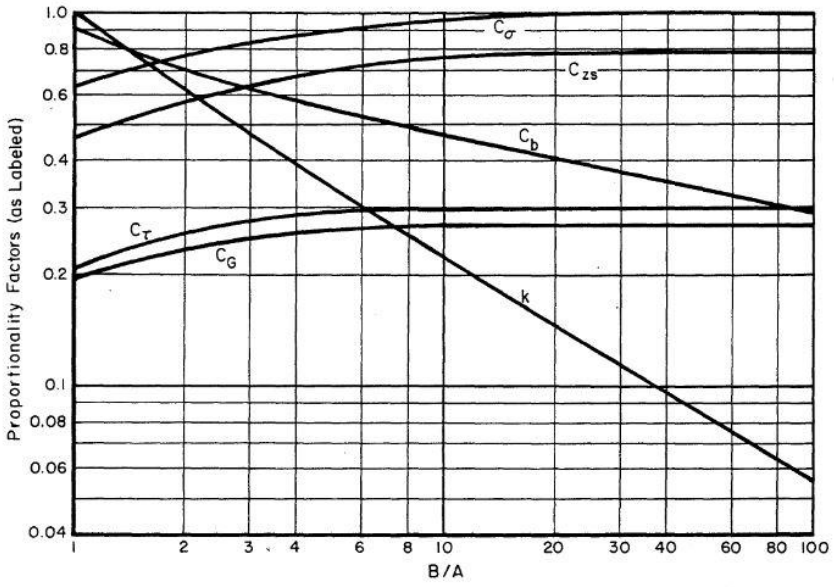

Figure 3-2. The variation of the constants C_a, k and C_b with respect to values $B/A = R_2/R_1$ [51] for the case straight longitudinal contact surface profile, and straight transversal wheel contact surface profile.

The constants C_b, C_a and k can be obtained from Figure 3-2 above and using the parameters is Table 3-1, as 0.82, 0.66 and 0.81 respectively. Using the equations presented above and the data obtained from Addis Ababa Light Railway Transit System (AALRTS) the contact patch dimensions are $a = 6.3$ mm and $b = 5.1$ mm. Furthermore a maximum normal contact pressure of 998.3 MPa was obtained. A plot of contact pressure distribution within the contact patch in accordance with Eq. 3-3 is shown in Figure 3-3.

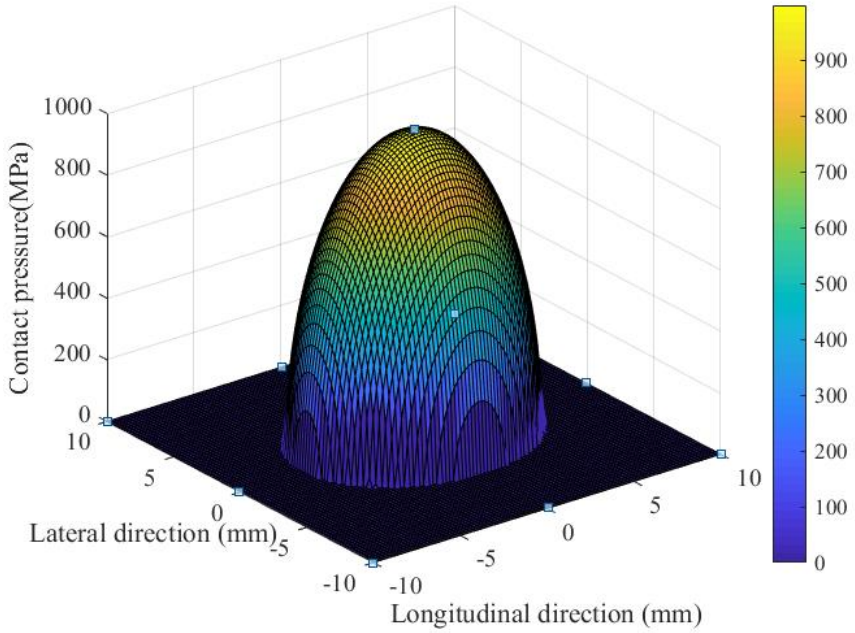

Figure 3-3. Contact pressure distribution in the wheel-rail contact patch according to AALRTS vehicle parameters.

3.1.2 Closed form solution of the 2D static contact mechanics problem.

2D rolling contact mechanics problems have been studied numerically, especially in the contact stress distribution behavior of functional graded materials (FGM). A closed form solution of a cylindrical stamp on a homogeneous half space was provided by Guler in [52]. Equations 3-4 to 3-6 show the analytical solution procedure for a 2D static contact between a roller and a flat surface.

$$\frac{\sigma_{yy}(x,0)}{\mu_{20}} = -\frac{p(x)}{\mu_{20}} = -\frac{1}{RD^*} sin\pi\alpha (b-x)^{\alpha}(x+a)^{\beta}, \qquad \text{Eq. 3-4}$$

$$\frac{\sigma_{xx}(x,0)}{\mu_{20}} = \begin{cases} -p(x) - \dfrac{\eta}{RD^*} L_c(x), & -a < x < b \\ -\dfrac{\eta}{RD^*} L_c(x), & x < -a, x > b \end{cases}$$

where

$\sigma_{yy}(x,0)$ is the normal contact pressure,

$\sigma_{xx}(x,0)$ is the surface shear stress in the longitudinal direction,

$L_c(x)$

$$= \begin{cases} -2(b-x)^{\alpha}(-x-a)^{\beta} - 2x + b - a + 2(\alpha-\beta)(b+a), & \infty < x < -a, \\ (b-x)^{\alpha}(x+a)^{\beta} cos\,\pi\alpha - 2x + b - a + 2(\alpha-\beta)(b+a), & -a < x < b, \\ 2(x-b)^{\alpha}(x+a)^{\beta} - 2x + b - a + 2(\alpha-\beta)(b+a), & b < x < \infty, \end{cases} \qquad \text{Eq. 3-5}$$

$$\frac{P}{\mu_{20} R_1} = \frac{2\pi\alpha\beta}{\kappa_2 + 1}\left(\frac{b+a}{R_1}\right)^2, \qquad b = \frac{\beta}{\alpha} a,$$

where

P is the vertical load in the negative direction.

μ_{20} is the modulus of rigidity.

R_2 radius of the roller.

a & b are the semi axis of the contact area.

α & β are constants obtained according to Eq. 8

η is the coefficient of friction

$$\eta > 0: \quad \alpha = \frac{\theta}{\pi}, \quad \beta = 1 - \frac{\theta}{\pi}$$
$$\eta = 0: \quad \alpha = 0.5, \quad \beta = 0.5 \qquad \text{Eq. 3-6}$$
$$\eta < 0: \quad \alpha = 1 - \frac{\theta}{\pi}, \quad \beta = \frac{\theta}{\pi},$$

$$\theta = arctan\frac{1}{\eta A^*},$$

$$\kappa_i = \begin{cases} 3 - 4\upsilon_i, & for\ plane\ strain \\ \dfrac{3-\upsilon_i}{1+\upsilon_i}, & for\ plane\ stress \end{cases} \quad ; \quad i = 1,2 \ldots$$

$$A^* = \frac{(\kappa_2 - 1) - (\kappa_1 - 1)\Gamma}{(\kappa_2 + 1) + (\kappa_1 + 1)\Gamma}, \qquad \Gamma = \frac{\mu_{20}}{\mu_{10}}$$

$$D^* = \frac{(\kappa_2 + 1) + (\kappa_1 + 1)\Gamma}{4}$$

$$R = \frac{1}{1/R_1 + 1/R_2}$$

'a' the longitudinal dimension of the contact patch was initially set at 9 mm in the analytical analysis. The vertical force corresponding to this contact patch dimension was calculated using Eq. 3-5 and used in the finite element analysis. To validate the mesh size and element type in ABAQUS the same contact patch dimension in the FEA has to be equivalent or approximately close to the analytical analysis solution. Moreover the equal or approximately close absolute maximum normal contact stress values has to be obtained in both analysis.

Table 3-2: Parameters used in this study

Vertical load, $\boldsymbol{P}$	1.6741×10^5N
Roller modulus of rigidity, $\boldsymbol{\mu_{10} = E/2(1+\nu)}$	80770 MPa
Half Plane modulus of rigidity, $\boldsymbol{\mu_{20} = E/2(1+\nu)}$	80770 MPa
Roller Radius, $\boldsymbol{R_1}$	380 mm
Half Plane Radius, $\boldsymbol{R_2}$	∞
Contact patch longitudinal dimension, a	6.3 mm
Roller modulus of elasticity, $\boldsymbol{E_1}$	200000 MPa
Half plane modulus of elasticity, $\boldsymbol{E_2}$	200000 MPa
Roller Poisson's Ratios , $\boldsymbol{\nu_1}$	0.3
Half plane Poisson's Ratios, $\boldsymbol{\nu_2}$	0.3
Plane stress coefficient, $\boldsymbol{k_1}$	2.08
Plane stress coefficient, $\boldsymbol{k_2}$	2.08
Friction coefficient, $\boldsymbol{\eta}$	0.4
Modulus of rigidity ratio, $\boldsymbol{\Gamma}$	0.96

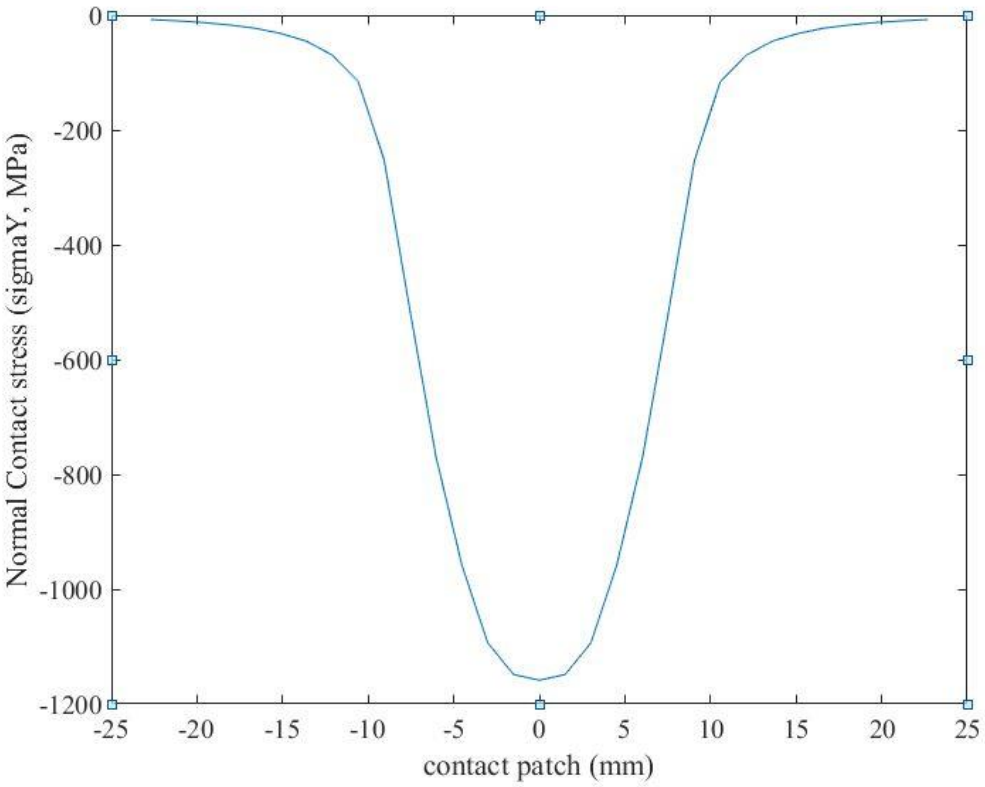

Figure 3-4: A plot of normal contact stresses (σ_{yy}) against longitudinal dimension of the contact patch for static analytical solution

3.1.3 Closed form solution of the 2D rolling contact mechanics problem

An analytical formulation and solution for rolling contact was conducted by Yadollah Alinia's [53]. The solutions provides plots of normal contact stresses and shear traction stresses. The profile of the shear traction stresses plot against the contact patch dimensions gives details of the slip and stick regions in the contact patch area. Eq. 3-7 presence the governing integral equations of a rolling contact problem according to Alinia. The solution procedure for these equation is presented in Eq. 3-8.

The governing integral equations for rolling contact problem

$$\frac{1}{\pi}\left(\frac{\kappa_1+1}{4\mu_1}+\frac{\kappa_2+1}{4\mu_2}\right)\int_{-a}^{+a}\frac{p(t)}{t-x}dt=-\frac{x}{R_0};\qquad -a<x<a \qquad \text{Eq. 3-7}$$

$$\frac{1}{\pi}\left(\frac{\kappa_1+1}{4\mu_1}+\frac{\kappa_2+1}{4\mu_2}\right)\int_{-a}^{+a}\frac{q(t)}{t-x}dt=\xi;\qquad -a<x<b$$

$$\kappa_i=\begin{cases}3-4\upsilon_i, & for\ plane\ strain\\ \dfrac{3-\upsilon_i}{1+\upsilon_i}, & for\ plane\ stress\end{cases};\quad i=1,2\ldots$$

$$\xi: creep\ ratio, \qquad \frac{1}{R_0} = \frac{1}{R_1} + \frac{1}{R_2}$$

The surface contact tractions

$$\sigma_{yy}\left(Sigma_{yy}\right) = -P_0\sqrt{1-\left(\frac{x}{a}\right)^2}, \qquad -a \le x \le a, \qquad \text{Eq. 3-8}$$

$$\sigma_{xy}\left(Sigma_{xy}\right) = \begin{cases} \eta\sigma_{yy} + \sigma_s, & -a \le x \le b \\ \eta\sigma_{yy}, & b \le x \le a \end{cases},$$

where

$$\sigma_s = \eta P_0\sqrt{1-\left(\frac{2x+a-b}{a+b}\right)^2}\left(\frac{1+{}^{b}/_{a}}{2}\right),$$

$$P_0 = \frac{2P}{\pi a},$$

$$\frac{b}{a} = 2\sqrt{1-\left|\frac{Q}{\eta P}\right|} - 1,$$

$$\frac{R_0\zeta}{a\eta} = 1 - \sqrt{1-\left|\frac{Q}{\eta P}\right|},$$

$$a = \sqrt{\frac{2PAR_0}{\pi}},$$

$$A = \frac{\kappa_1 + 1}{4\mu_1} + \frac{\kappa_2 + 1}{4\mu_2},$$

P is the vertical load,

Q $= 0.75 \times \eta \times P$ (Traction Force),

μ_i for i=1,2 are the modulus of rigidity of the roller and half plane,

R_i for i=1,2 are the roller and half plane radii,

a & b are the semi axis of the contact area,

η is the coefficient of friction.

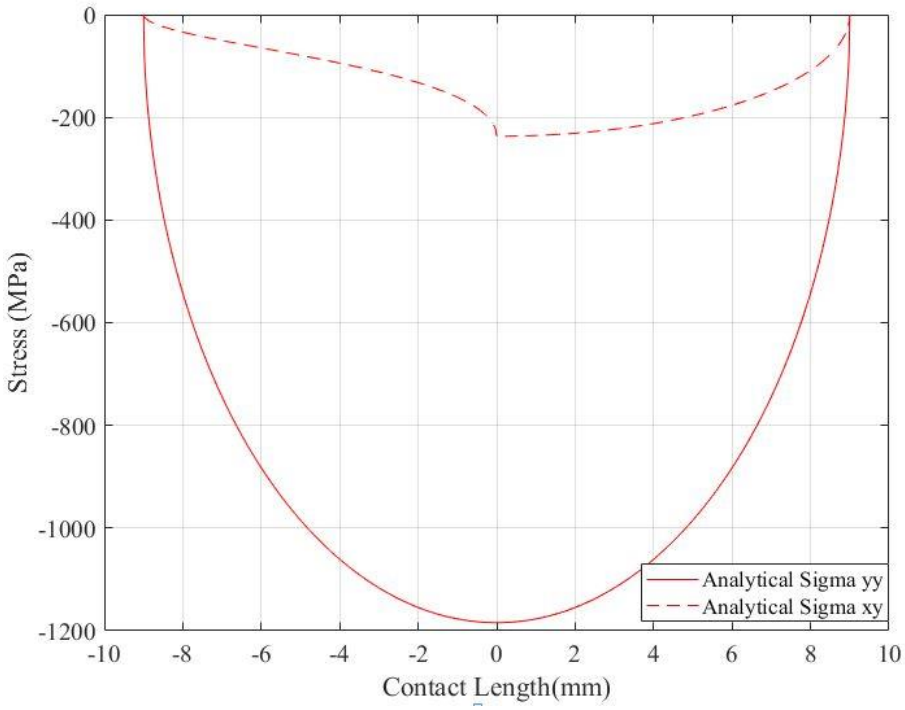

Figure 3-5: Analytical plot of normal contact stresses (σ_{yy}) and surface shear stress (σ_{xy}) against longitudinal dimension of the contact patch for rolling contact analytical solution

3.1.4 Simple roller on a flat plane FE model validation.

In the section a simple roller on a half plane (i.e. flat surface) is modelled and analyzed using the finite element techniques utilizing the ABAQUS simulation software package. The objective is to identify the mesh element type and size that provides a contact solution which converge to the 2D analytical static and rolling contact solutions. This validation technique also proves the validity of the contact algorithm to be used in ABAQUS (i.e. ABAQUS rolling contact solution). The cross sectional dimensions of the wheel and the rail at the point of contact are used as the dimensions of the roller and the half plane respectively. A very small thickness is assigned to the modelled parts to portray the 2D rolling nature solved in the analytical solution. The model outline and design is described below. Table 3-3 shows the geometrical parameters used in modelling both the roller and the half plane. Sketch of the model to be used in this analysis is depicted in Figure 3-6.

Table 3-3: Roller and half plane geometry parameters

Half plane (mm)			Roller (mm)	
Height	Width	Thickness	Radius	Thickness
171.82	1500	10	380	10

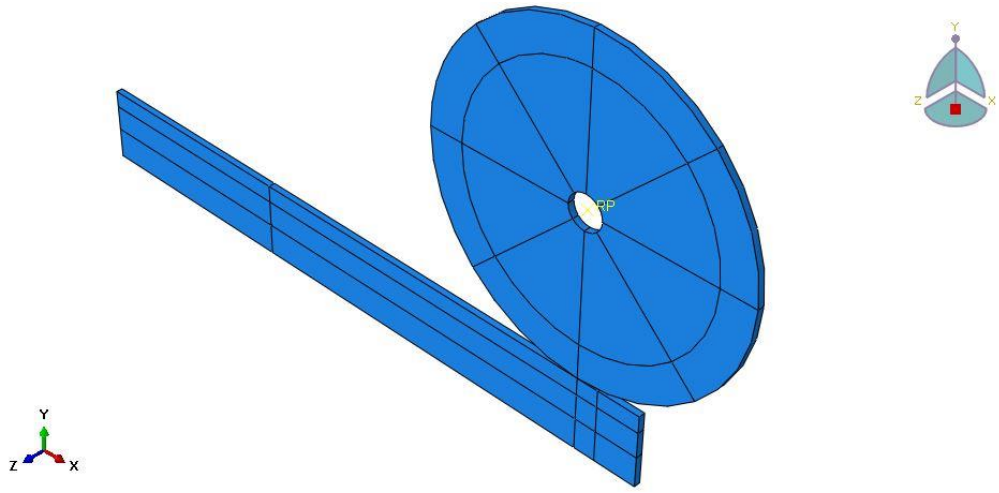

Figure 3-6: Simple roller on a half plane Finite Element (FE) static and dynamic analysis model.

a. Material parameters

Steel material was used in this analysis owing the steel to steel contact nature of the wheel and rail. A young's modulus of $E = 2 \times 10^5$ MPa, a Poisson's ratio of $v = 0.3$ and a density was 7.8×10^{-9} tons/mm^3 were used and material properties in this validation procedure.

b. Interaction module

Both normal and tangential contact behaviors were defined for the interacting surfaces of the roller and the half plane. A hard contact, pressure overclosure was defined for the normal behavior. In the tangential behavior a static-kinetic exponential decay coefficient of friction was defined for the friction formulation. A static friction coefficient of 0.4, a kinetic coefficient of friction of 0.32 and a decay coefficient of 6 were assigned based on literature review data. A coupling constraint was defined between the roller side surface and a reference point on the roller center (see Figure 3-7 below)

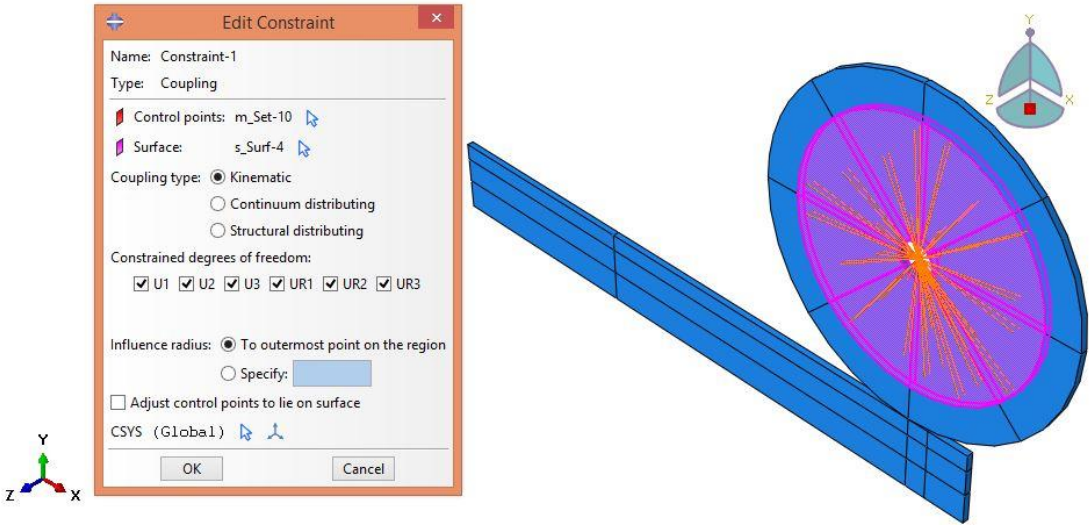

Figure 3-7: Coupling constraints definition in ABAQUS between the roller center reference point and the roller side surfaces.

c. Boundary conditions and loads application

The analysis was divided into two steps. The first step is the pre-stressing step where the loads are applied. This is followed by the rolling step where the roller is roller through a finite distance. The applied boundary conditions are dependent on the step and a propagated or modified in the following step. The static analysis has only step_1 the pre-stressing step while the rolling step consists of both steps.

Two dynamic explicit steps were created for the rolling contact analysis.

Step_1 Pre-Stressing: A downward force Fy was applied at the roller center with a linear amplitude.

- The bottom of the half plane instant was constrained in all degrees of freedom to zero.
- The roller was allowed only to move in the vertical direction. The boundary condition was applied on the reference point on the center of the roller instant.
- The side surfaces of the roller were restricted from moving sideways (i.e. z axis direction)

Step_2 Rolling-step. A rotation angle in the +ve z-direction was specified on the internal surfaces of the shaft hole on the roller.

- A torque was assigned to a reference point on the center of the roller which was coupled with the side surfaces of the roller.
- The vertical loads applied in Pre-stressing step were kept constant.
- A longitudinal displacement in the rolling direction was also defined.
- The roller side surfaces were restricted to move in the lateral direction

d. Mesh module

An 8-node linear brick with reduced intergration and hourglass control explicit 3D stress element was used as the m+esh element type in this study. Table 3-4 shows the element sizes used in the analysis. Figure 3-8 shows the meshed model, a fine mesh was assigned to the regions under consideration on both instances.

Table 3-4: Mesh specifications

Half plane (Refined mesh in contact area)		Roller (Refined mesh)
Element Size length	Element Size width	Cylindrical Edges Element Size
2.5mm	5mm	5mm

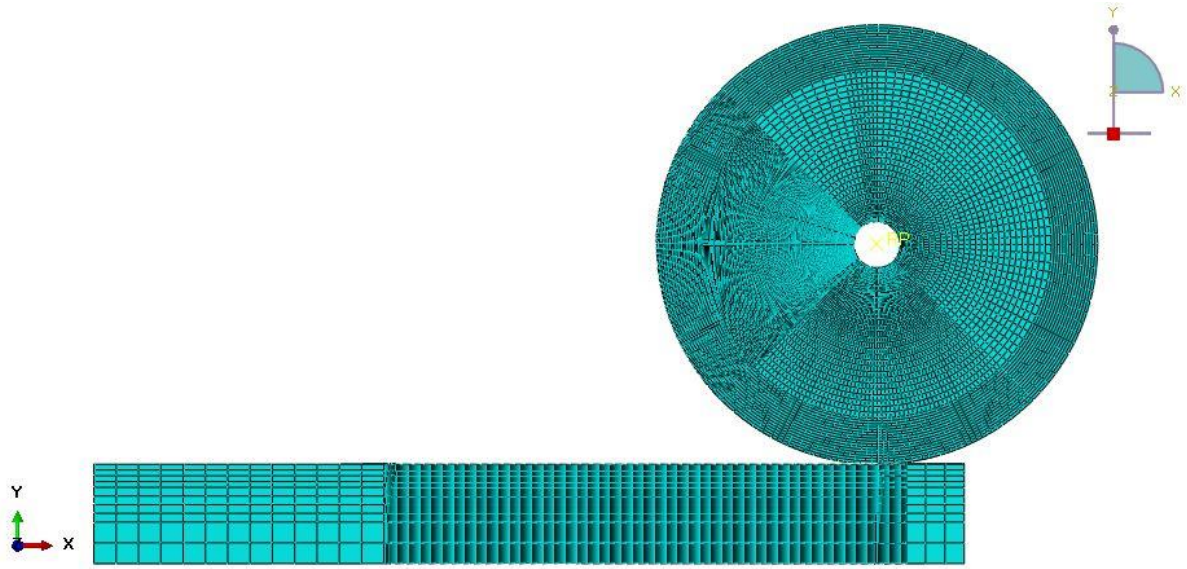

Figure 3-8: Meshed roller on a half plane model.

e. Static and rolling contact finite element solution results

The static analysis was done in only Step_1 the pre_stressing step. Only the vertical loads were applied and the roller was allowed to displace in the vertical direction. The static normal contact stresses were compared with the analytical solution from Gulers' method.

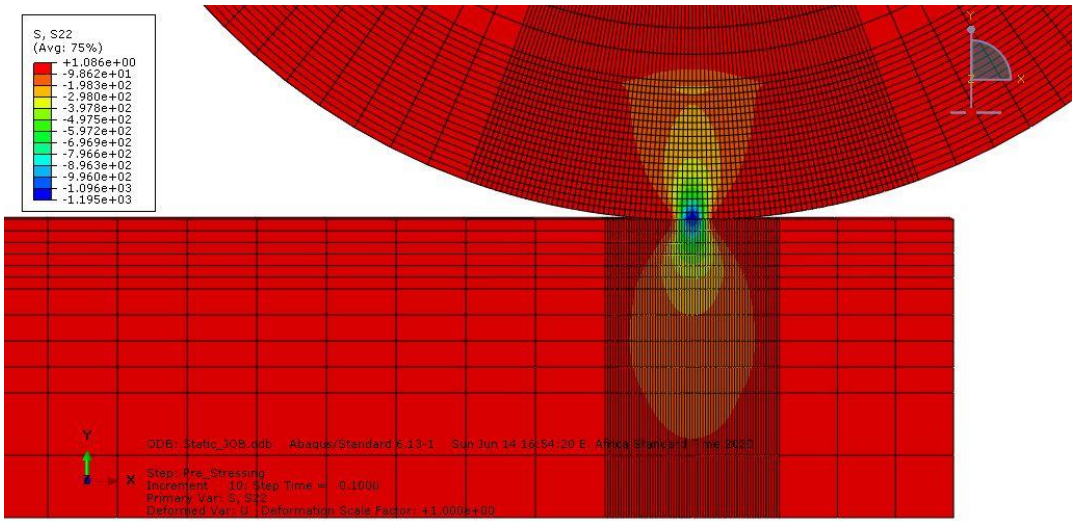

Figure 3-9. Normal contact stress (σ_{yy}) distribution within the roller and the half plane in the FE static analysis.

Figure 3-9 shows the contour plots of the results from the finite element analysis in the visualization module in ABAQUS. The maximum normal contact stress is on the contact interface of the roller and the half plane. A plot of normal contact stress against contact patch longitudinal dimension is shown in the figure below.

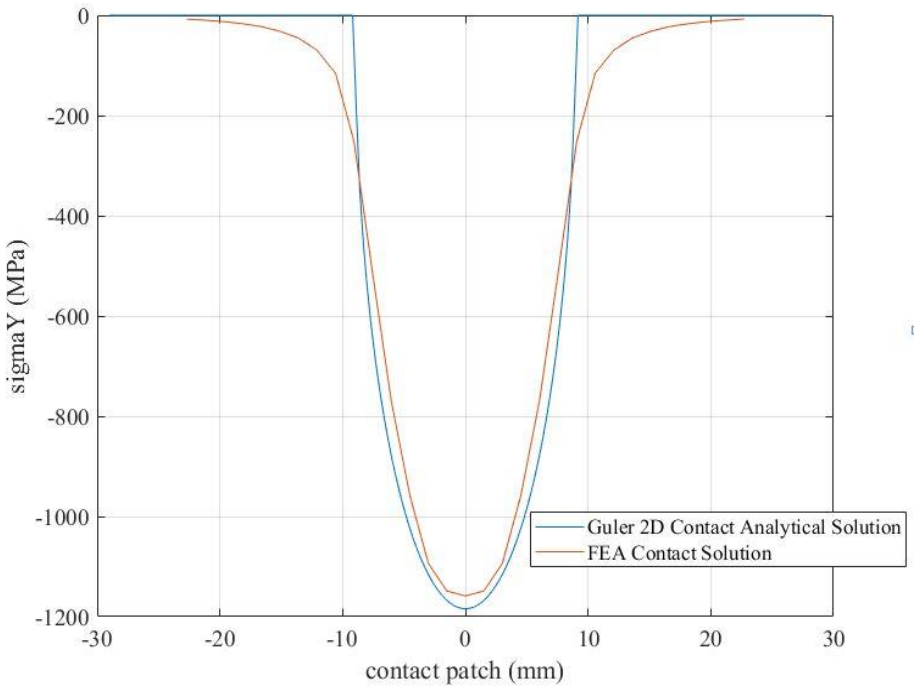

(a)

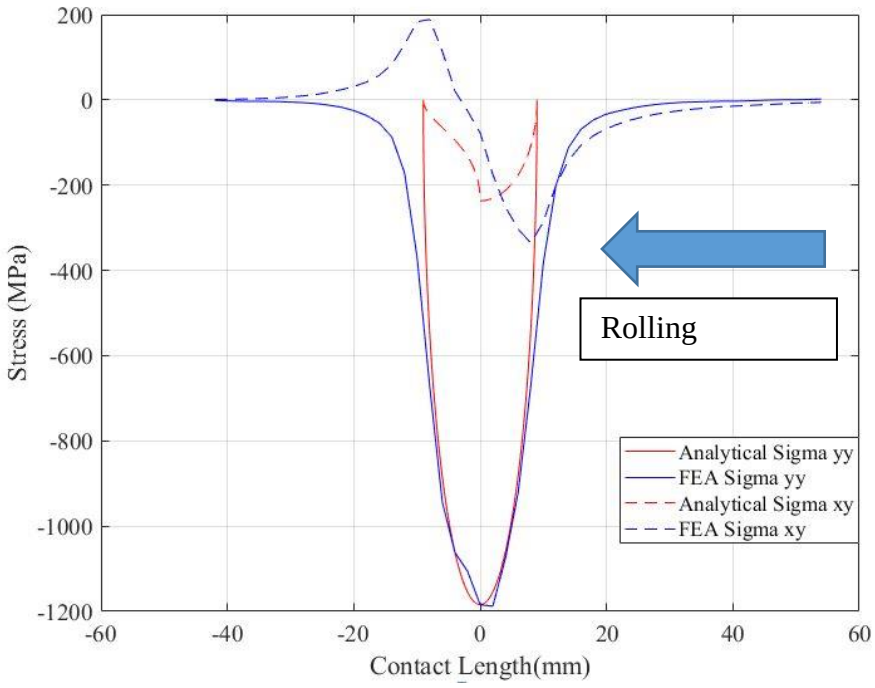

(b)

Figure 3-10. Comparison of normal contact stress (σ_{yy}) and surface shear stress (σ_{xy}) against contact patch dimension. (a) A plot of static contact analytical and FEA results. (b) A plot of rolling contact analytical and FEA solutions.

From Figure 3-10 (a) it can be seen that there is a good agreement between the static normal contact stress results obtained from the Guler analytical method and the Finite Element Method. A half contact patch length of 9 mm was used in the analytical solution, and there is a deviation of this dimension in

the FEA solution due to the gradient of the contact stress in the periphery of the contact patch, which was not observed in the analytical solution. This analysis proves that the element type and sizes used in the section 3.1.4 can provide reliable results for a contact solution.

The results of the rolling contact analysis of a simple roller on a half plane are shown in Figure 3-10 (b). Both steps outlined in the model design were applied for the rolling analysis. The roller was rolled for a distance of 800 mm with an angular velocity of 300 radian/sec. A time step of 0.007 seconds was prescribed for the rolling step. The results shown in Figure 3-10 (b) were extracted at the last frame of the rolling step. It can be seen that there a good agreement in the normal contact stress between the FE and analytical solution. There is a deviation in the shear stress solution in the FEA as compared to the analytical solution. The characteristics of the stick-slip contact conditions can still be observed from the profile of the shear stress curve and this provides the validity of the ABAQUS rolling contact solutions. From the analytical shear stress curve the concave section of the graph shows the slip region while the convex section shows the stick region.

3.1.5 FE rolling contact analysis solution comparison with previous studies

Zhao et al [28] conducted a research on the "solution of frictional wheel-rail contact using 3D transient finite element model". The 2D schematic diagram of the model used in their finite element analysis is as shown in Figure 3-11.

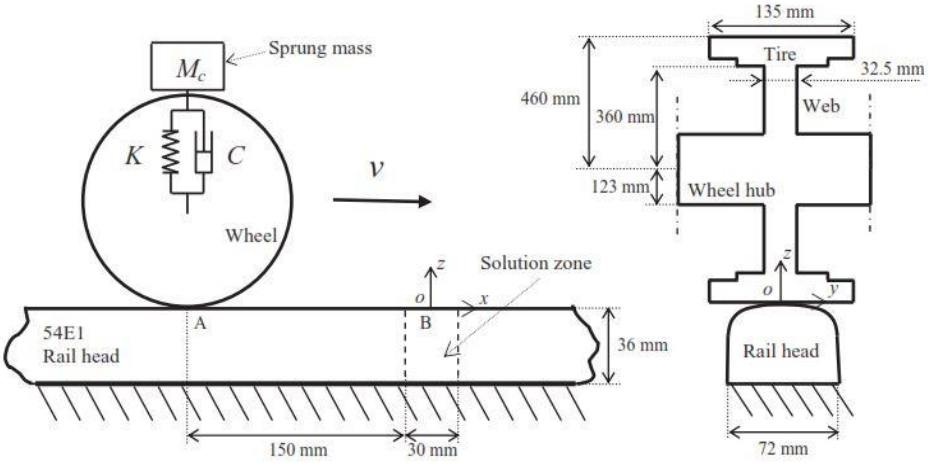

Figure 3-11: Schematic diagram of the transient FE model according to Zhao [28]

In their analysis the wheel was rolled on the rail at different friction coefficients. The Hertz theory as well as the Kalker's computer program CONTACT were used for the normal contact solution while the CONTACT software package was utilized for the tangential solution. The frictional FE rolling contact model was validated in this study based on the Hertz contact theory and the stick/slip condition occurring within the contact area during wheel rolling.

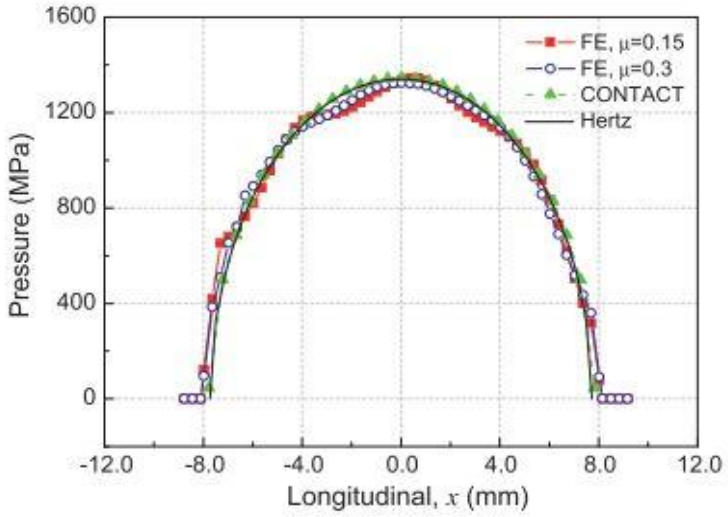

Figure 3-12: Normal contact stress solution using various methods (Zhao 2011 [28])

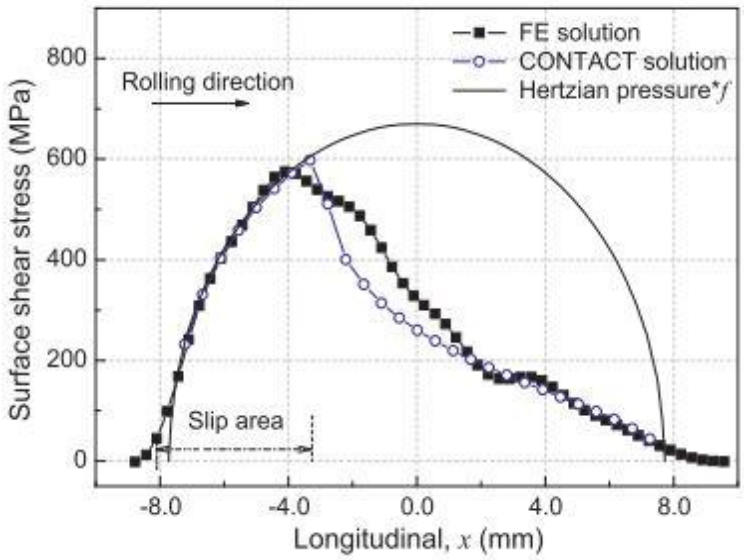

(b)

Figure 3-13: Surface shear stress distribution within the contact patch comparison of FE surface shear stress results with Hertzian and contact solutions [28].

The results presented by Zhao proved the validity of FEM in solving wheel-rail contact problems as shown in their solutions in Figures 3-12 and 3-13.

3.2 Methods of equivalent track stiffness determination for finite element analysis models

The railway road track stiffness at a particular point of contact can vary in three directions i.e. lateral, vertical and longitudinal directions. In this study the effects of vertical track stiffness variation in the longitudinal direction is studied. The railway road vertical track stiffness is a summation of the

individual stiffness of track components. This includes the rail stiffness, fastener stiffness, rail pads stiffness as well as the ballast, sub-ballast and subgrade stiffness. The vertical track stiffness can also be classified as static and dynamic track stiffness. In addition to railway track infrastructure components the static vertical track stiffness also depends on the vehicle loads. The dynamic vertical track stiffness is a function of vehicle speeds and acceleration in addition to track components and vehicle loads. In order to reduce the computational time in studies involving train – track system interaction simulations using finite element methods an equivalent track stiffness has to be defined for the track infrastructure. A number of methods and techniques have been adopted by various researchers over time to establish the equivalent track stiffness for finite element analysis of both coupled train-track dynamic systems and track system performance evaluations.

Drozdziel, Sowinski and Szulczyk [54] conducted a research which involved the determination of the equivalent track stiffness for FEA and its variation along the track. The authors defined a railway track as a continuous infinite Bernoulli-Euler beam resting on elastic foundations (see Figure 3-14 below) where *k* if the equivalent track stiffness. The governing differential equation of a Euler-Bernoulli beam laying on an elastic foundation and subject continuous loads (i.e. Eq. 9) was solved analytically for the beam deflections. The relationship between the rail deflection and the equivalent vertical stiffness was established.

$$EI\frac{\partial^4 y}{\partial x^4} + m\frac{\partial^2 y}{\partial t^2} - ky = q(x) \qquad \text{Eq. 3-9}$$

where;

EI- bending stiffness of beam,

k - vertical stiffness of elastic foundations,

$q(x)$ - continuous load,

m - Track mass.

$$y(x) = \frac{Q}{2kL}u(x) \qquad \text{Eq. 3-10}$$

where;

$$L = \sqrt[4]{\frac{4EI}{k}},$$

and $u(x)$ - normalized line of track center line deflection (relative deflection).

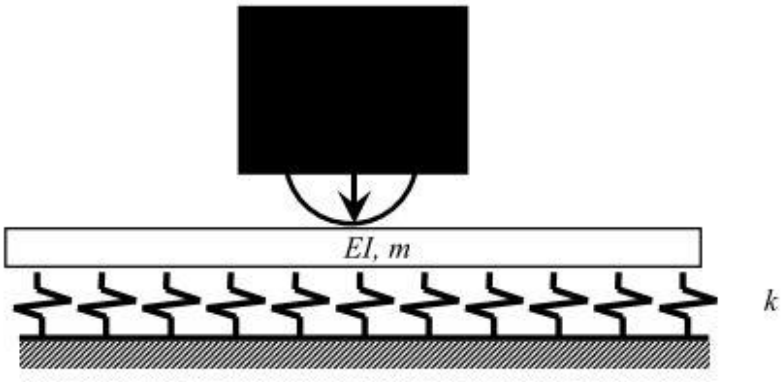

Figure 3-14. Railway track laying on an elastic foundation[54]

In this study the determination of the equivalent railway track stiffness is based on railway web strain measures at full loading capacity of a light rail transit vehicle. At constant loading condition the strains acting in the rail track web are dependent on the deflection of the rail which is dependent on the flexibility of the track support system (i.e. track stiffness) [55]. To determine the equivalent track stiffness for FEA a railway track laying on crossties (i.e. sleepers) of uniform modulus is modeled in a finite element simulation software package environment (i.e. ABAQUS). A constant load corresponding to the dynamic loads acting in the wheel-rail interface during train operation is applied on the rail head top surface in an elliptical shaped contact patch. The equivalent railway track stiffness is determined in terms of the equivalent crosstie modulus in the simulation software. At varying crosstie modulus and constant load application the strains acting in the railway track web are recorded and a plot of strains versa crosstie modulus is sketched. Using strain measurements data from experimental studies in past researches, a crosstie modulus that provides the same railway track web strains as the actual railway track stains in real operation is defined as the equivalent crosstie modulus. The spatial variation of railway track stiffness is achieved by varying the crosstie modulus ratio of consecutive crosstie in the simulations.

3.2.1 Literature data of railway track web strains

The strains occurring in the railway track web are dependent on a number of factors such as railway vehicle loads, track alignment, track irregularities, wheel-rail contact stresses and forces, track stiffness etc. as mentioned in the previous chapters. Mayers [56] studied the influence of railway vehicle speeds on the insulated railway joints after he observed the reduction in railway speeds at these joints imposed by the Australian Railways, with the aim of reducing failure. He used field measurements at two different locations on the Australian rail network in his study using strain gauges. It was concluded in this research that the railway vehicle speeds in the range of $20 - 90$ km/hr. did not have any influence

on the joint strains. The difference in failure rates and modes at the two different locations of study, was said to be due to the difference in sleeper deflections which are related to the track super and substructures stiffness difference. Figure 3-15 shows the strain measurements from Mayers experiments which are to be used as a reference to rail track web strain range in this study.

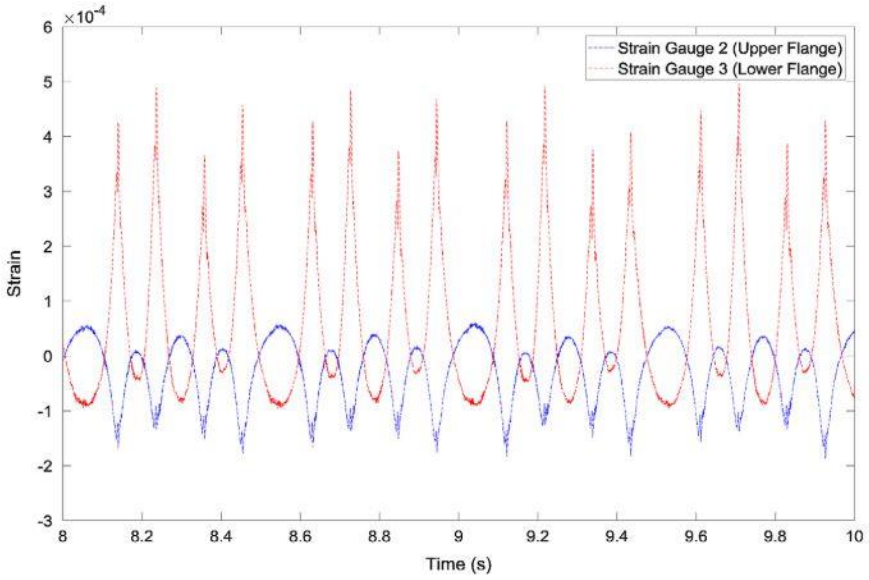

Figure 3-15. Strain measurements for insulated rail joints [56]

Rail web strain measurements are used to detect wheel tread defects and damages. Railway vehicle wheel tread defects induce high impact interaction between the wheel and the rail, which can damage both the rolling stock under equipment and cause high deterioration rate of the track infrastructure. Wheel tread defects monitoring systems have been developed which utilizes the railway track web strains values fluctuation to detect damages and potential hazards. Sych and Kolomeets [57] developed a calibration method of lateral and vertical rail forces based on strain measurements. Both static and dynamic experiments were carried out and their set up is as depicted in Figure 3-16 below.

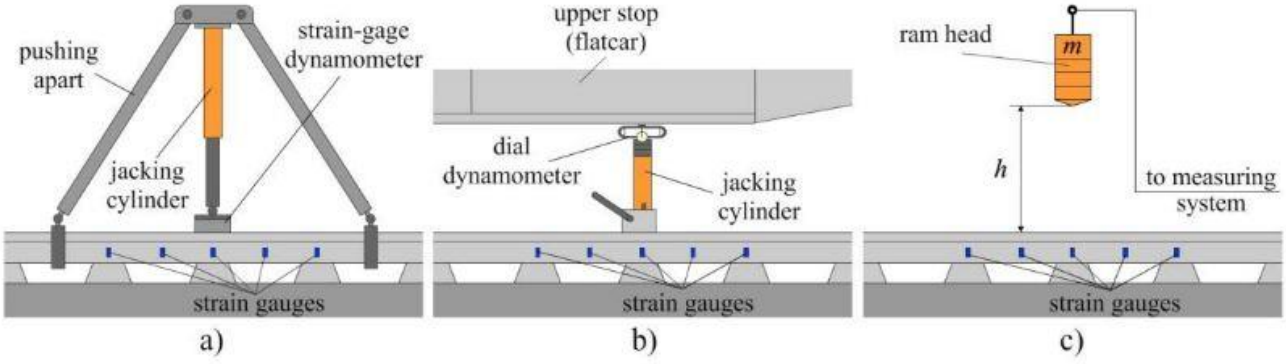

Figure 3-16. Calibration schemes for the strain-gauge section with: a) static force applied from the expanding device; b) static force applied to the cross beam of a loaded freight car; c) dynamic force applied from the special-purpose impact device [57].

In Sych and Kolomeets's research vertical loads with an 18 kN increment were applied on the rail head and a maximum load of 108 kN was set.

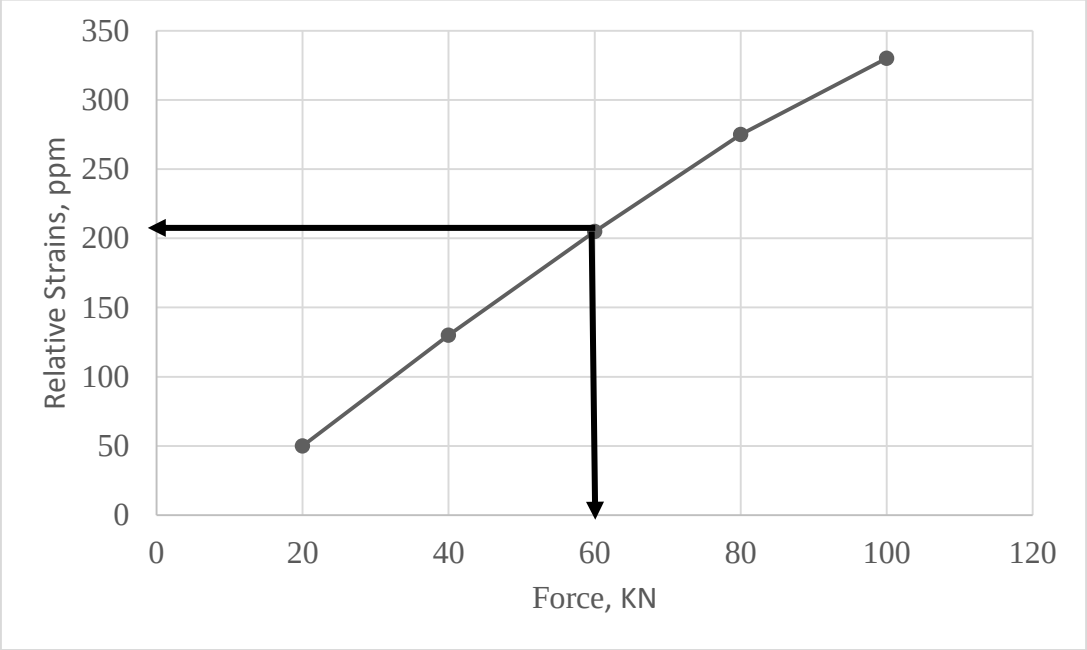

Figure 3-17. Relative strains against the vertical force applied to the rail (strain unit-parts per million, ppm) (Replotted from [57]).

The authors (Sych and Kolomeets) took into consideration the stiffness of the rail base which provides more realistic strain measurements. The stiffness of the substructure was not taken into consideration. Wang et al [58] conducted a study on the longitudinal force measurements in continuously welded rails. Energy method, stress method and strain method by measuring principles are the most used experimental techniques to determine the longitudinal forces in wheel-rail contact. Wang et al highlighted that the strain measurement method is the mainly used and more efficient and effective method of determining railway track longitudinal forces. A report from mid-America transportation center by Robert et al [55] provides a summary of a research on the development of a procedure to determine the existing stresses in steel rails used in railway tracks. Thermal effects as well as mechanical loading were taken into consideration.

Based on the presented short section of a literature review on the railway track web stresses and strains, it was observed that the railway track web strains in the vertical direction are in the range of $200 - 300$ ppm (i.e.300 parts per million) for loads in the range of $54 - 108$ kN [57]. In this study a strain of 206 ppm will be used as the railway track web strain value for a light railway vehicle. This stain value will be an input to a later section where the crosstie modulus of the crosstie material in ABAQUS, which will resemble the equivalent railway track stiffness in the simulation environment is determined.

3.2.2 Wheel-rail contact FE static model design and validation method

The railway track was assumed to be symmetrical about the rail gauge centerline therefore a single rail supported on sleepers (i.e. crossties) was analyzed throughout this study. A FE model consisting of a railway track, a full single middle crosstie and two half side crossties was developed in ABAQUS. The dimensions of the UIC60 Railway Track Profile used in this study are as shown in Figure 3-18. The material type and properties of the railway track used in the simulations are as shown in Table 3-5. A 1.5 meter long rail section supported by three crossties was modelled.

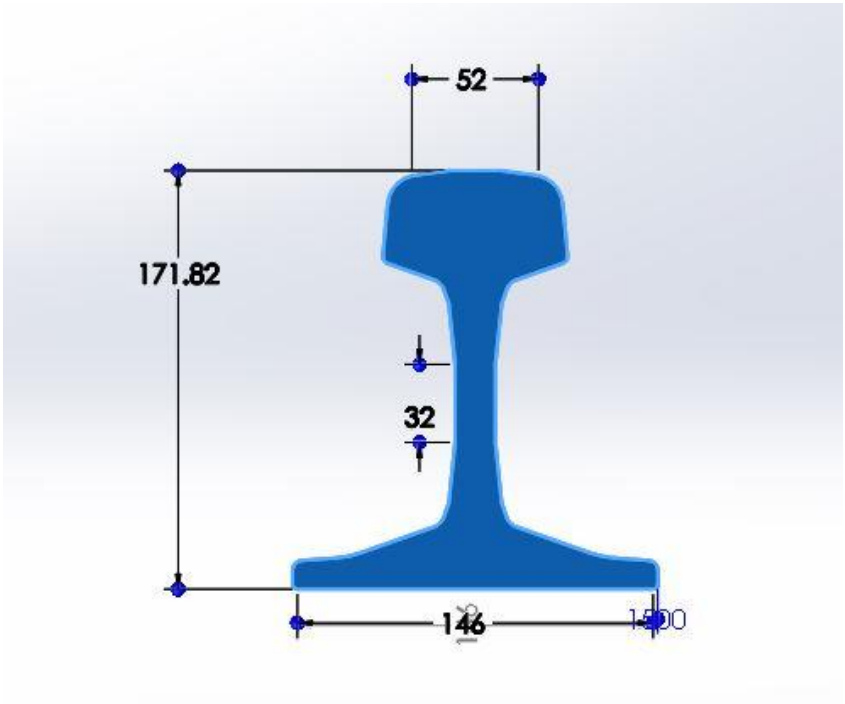

Figure 3-18. UIC60 railway track profile (Dimensions in mm)

Table 3-5. Material properties for Railway track UIC60

Material	Pearlite steel
Modulus of Elasticity	190 GPa
Density	7.8×10^{-9} tons/m^3
Poison ratio	0.3
Yield stress	550 MPa
Plastic strain	0
Rail specific heat	450 J/kg K

The sleeper was modelled as a rectangular block and its dimension are as shown in Figure 3-19 below. The material properties of the crossties used in this study are as shown in Table 3-6. The material was chosen to be concrete to portray a realistic track structure. The crosstie length was reduced to limit the

number of elements and reduce the computational time. The modulus of elasticity of the crossties is used to define the equivalent track stiffness in the study. An estimate starting value of 300 MPa for the crossties modulus of elasticity was assumed based on a previous study by Nkundineza and Turner [59]. The purpose of this FEA static analysis is to calibrate the crosstie modulus of elasticity so as to obtain equivalent rail track web strains in the simulation environment as in field observations and experiments from past researches. Therefore simulations with different crosstie modulus in the range of the initial selected value, were conducted in ABAQUS and the railway track web strains from the FE model were recorded.

Table 3-6. Equivalent Properties for the rail track support structure (i.e. Crosstie Properties)

Crosstie Height	**210** mm
Modulus of elasticity (Estimate value from literature)	300 MPa
Poison ratio	0.22
Material	Concrete
Density	2400 kg/m^3

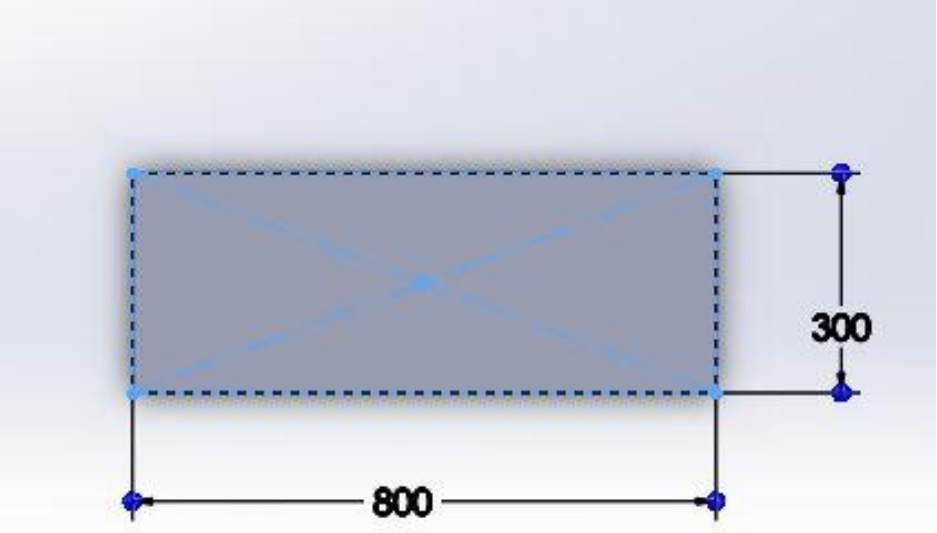

Figure 3-19. Crosstie dimensions (Dimension in mm)

This study was conducted based on some parameters from Addis Ababa Light rail transit system (AALRTS). These includes the vehicle parameters and loading conditions as shown in Table 3-7 below. Since a single rail and half of the axle (i.e. quarter car model) were used in the analysis, half of the axle loads was applied.

Table 3-7: Addis Ababa Light Rail Transit Vehicle parameters

Full capacity Axle loads, $\boldsymbol{m_1 \times 2}$	$\mathbf{10.5}$ tons
Primary suspension stiffness, $\boldsymbol{k_1}$	1150 N/mm
Primary suspension damping, $\boldsymbol{C_1}$	50 N.s/mm
Secondary suspension stiffness	550 MPa
Secondary suspension damping	60 MPa
Wheel diameter (new)	660 mm
Wear diameter limit	580 mm
Last re-profiling	595 mm
Flange thickness (new)	21.21 mm
Flange height (new)	28 mm

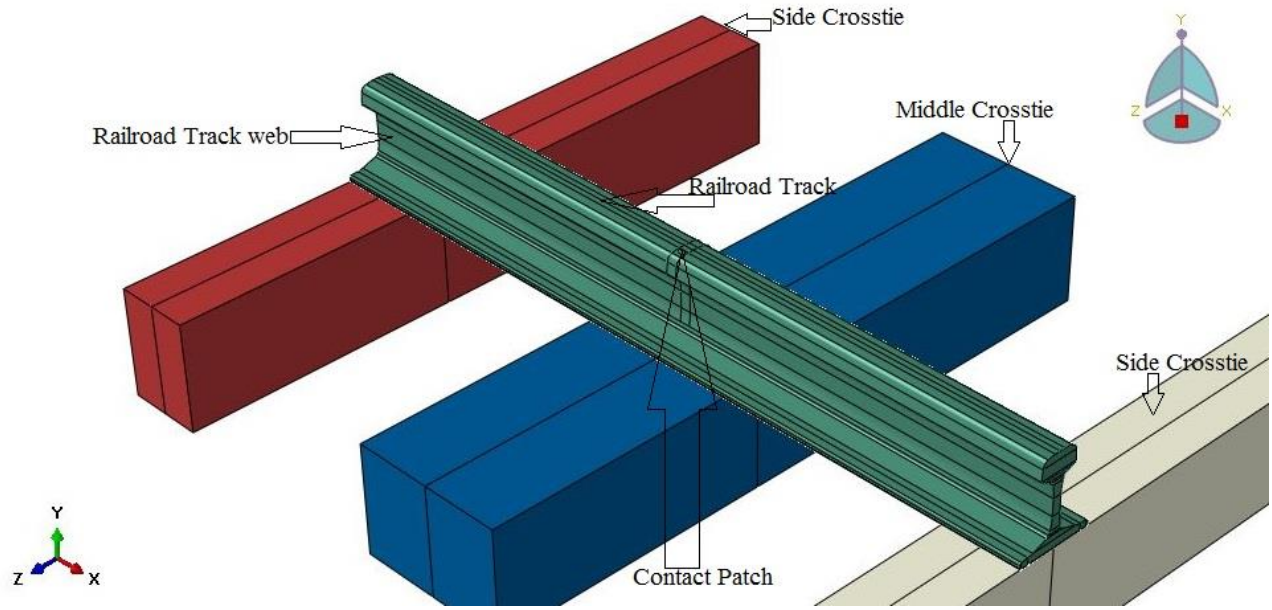

Figure 3-20. ABAQUS FE static analysis model set up

The assembled ABAQUS model to be used in the validation of the contact pressure and contact dimension in the determination of the equivalent railway track stiffness is as shown in Figure 3-20. A uniform crosstie modulus is employed to signify a uniform track stiffness in the static analysis. An elliptical shaped contact patch, 15 mm off set from the railhead center line was sketched on the railhead top surface. The dimension of the contact patch are $a = 6.3$ mm and $b = 5.1$ mm as calculated in Section 3.2. A contact pressure distributed according to the Hertz contact theory (i.e. semi ellipsoidal, see Eq. 3-3) was applied in the contact patch area. A fine mesh was defined in the contact patch in order to obtain accurate results.

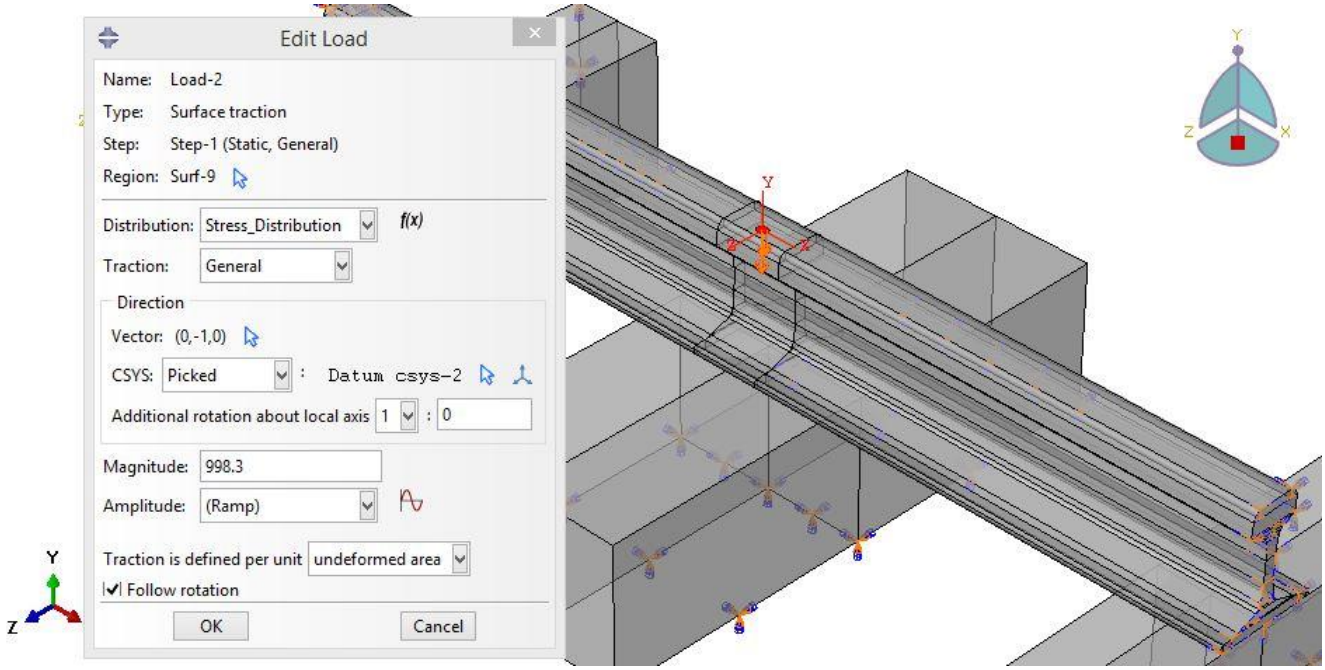

Figure 3-21: Traction force application within the contact patch which is distributed in accordance with Eq. 3-3

Applied boundary conditions

The static analysis was executed in a single step called the Pre-Stressing_Step. The vehicle load was applied through a ramp amplitude. The standard static general solution procedure was used in this analysis with a time step 0.1 seconds.

- The crossties were fixed at the bottom in all directions. This was to resemble the ground fixed the railway track support infrastructure.
- A tie constraint was defined between the crosstie and the railway track bottom surface. This constraint was used as a fastening system between the rail and sleepers.
- Both ends of the railway track were assigned a zero displacement in the longitudinal direction (i.e. x axis direction). This was to portray a large longitudinal length of the rail relative to other dimensions (i.e. lateral and vertical rail dimensions).

Results

The results of the above outlined simulation procedure are presented in Figure 3-22 and Figure 3-23 below. For simplicity reasons and for high accuracy of the Hertz contact results a simplified railway model with a flat railhead top surface was used in this analysis. A very fine mesh was defined in the contact patch area as shown in Figure 3-22. A path of nodes along the longitudinal semi axis of the contact patch was defined. The normal contact stress (σ_{yy}) was plotted against the contact patch length along the defined path. A plot of σ_{yy} against contact patch dimension is shown in Figure 3-23. The absolute maximum normal contact stress obtained in the FEA results and the dimension of the contact

point is equivalent to the results obtained in the Hertz contact analysis conducted in Section 3-2. These results provides the validity that a very fine mesh can provide small errors between the FE method and the analytical solutions. The results obtained in this analysis were used in the validation of a coarser mesh used in the determination of the equivalent crosstie modulus (i.e. See the following chapter for more detail).

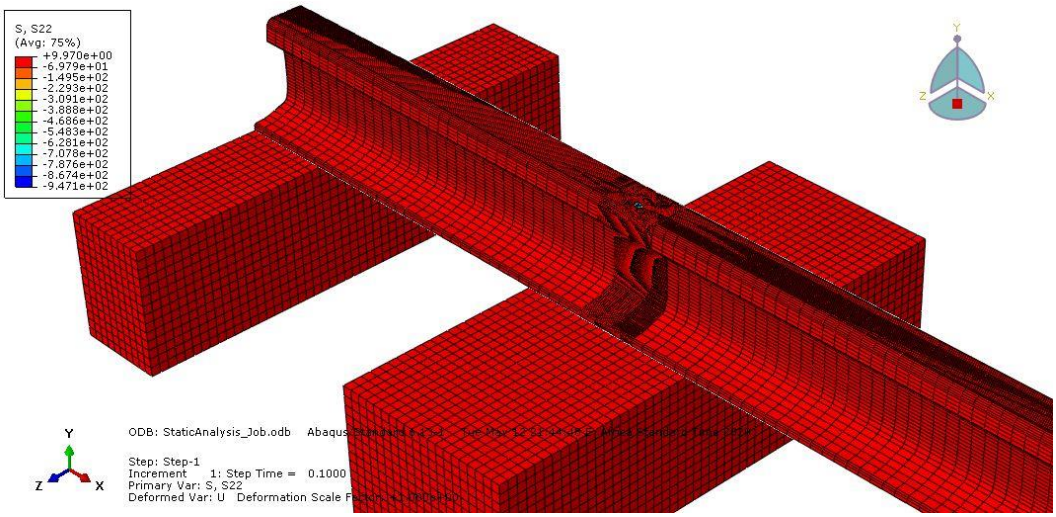

(a)

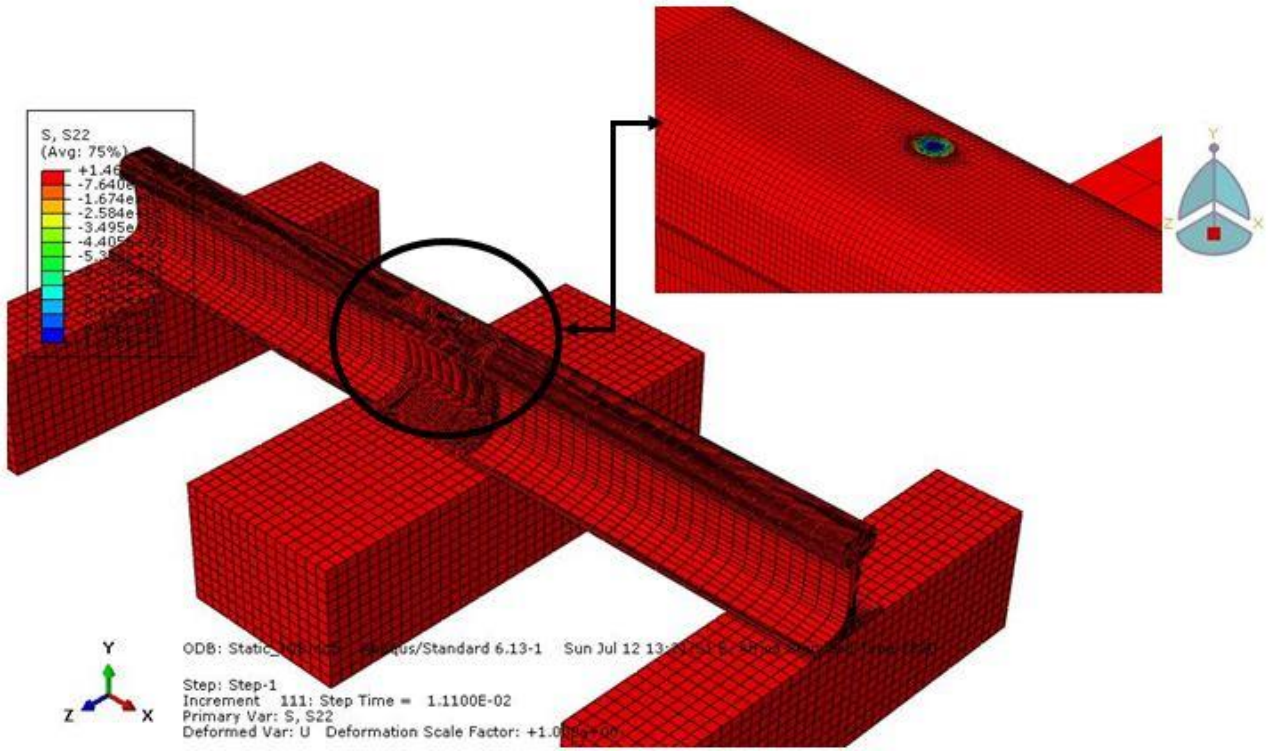

(b)

Figure 3-22: Rail profile FE model solution for normal contact pressure distribution in the contact patch area in accordance with hertz theory (a) σ_{yy} results visualization for the whole model (b) Contact pressure distribution in the contact patch.

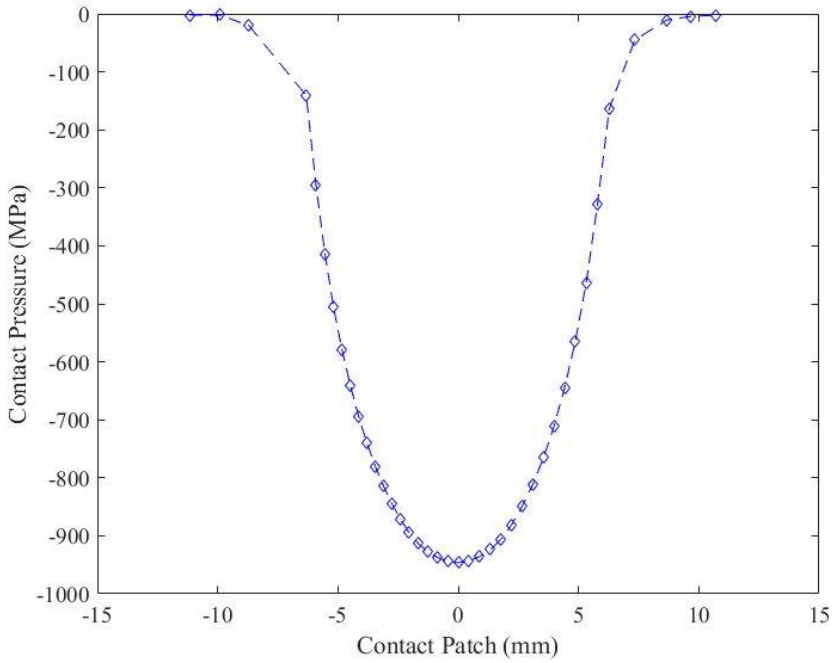

Figure 3-23: A plot of FE static contact pressure against the contact patch dimensions. Contact pressure distribution and contact patch dimensions are in accordance to the Hertz contact theory calculations.

Figure 3-22 and Figure 3-23, respectively shows the contour plots and the contact pressure plot from the static finite element analysis using data from the Hertz contact theory. As expected the contact pressure in the FEA solution for a very fine mesh matches the hertz contact analytical solution. As in the static analysis presented in section 3.1 the small difference in the contact patch dimensions is due to the FEA solution stress gradient in the contact patch periphery.

3.2.3 Validation of a 3D wheel-rail FE static contact model

The FE static analysis model to be used in the determination of the equivalent crosstie moludus is validated against the results obtained in the Hertz contact analysis. A coupled train-track system which consists a quarter car model was modelled in ABAQUS and the static sprung and unsprung loads were applied through a primary suspension system wheel axel respectively. The model design is elucidated below.

Model design

The railway track and crossties geometries used in the static analysis without a railway vehicle wheel were also imported into the static analysis model validation. In addition to the model described above a railway vehicle wheel based on the P8 wheel profile dimensions, was designed in Solid works and imported to ABAQUS. The wheel geometry is depicted in Figure 3-24. The 3D view of the P8 wheel

as well as the cross sectional view are shown in Figure 3-25. Table 3-8 shows the material type and properties used for the wheel.

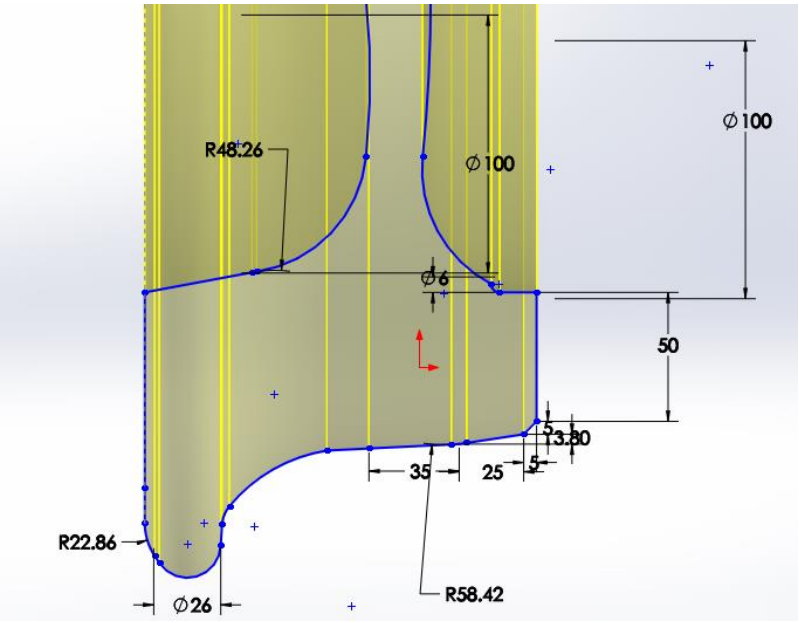

Figure 3-24. Standard P8 railway vehicle wheel profile.

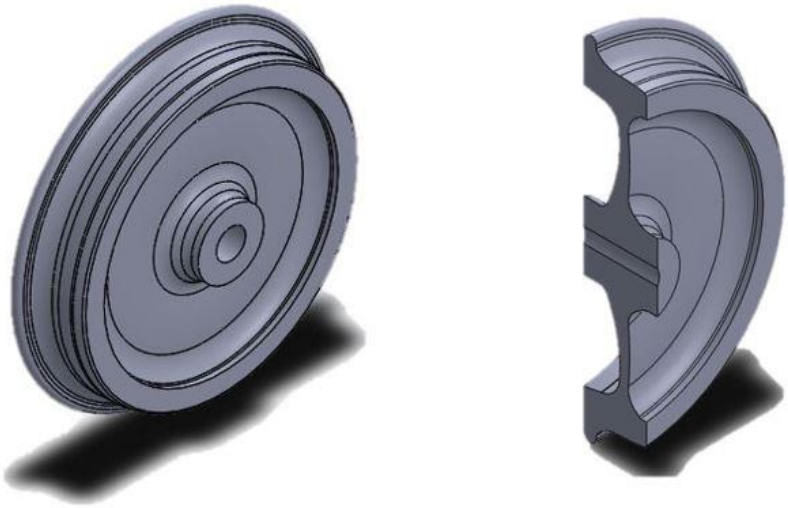

Figure 3-25. P8 railway vehicle wheel 3D view and cross section along the wheel diameter.

Table 3-8. P8 rail vehicle wheel material properties

Modulus of elasticity	**200000** MPa
Poison ratio	0.3
Yield stress	680 MPa
Plastic strain	*0*
Density	$7.8e-09$ tons/mm^3

Specific heat	450 J/kg K
Thermal conductivity	0.15
Wheel radius	380 mm
Wheel material	Steel

The model to be validated consist of a single wheel on a rail. Quarter weight of a fully loaded light rail transit vehicle is considered as well as the primary stiffness and damping as depicted in Figure 3-26. The primary suspension system parameters and the axle mass of a fully loaded light rail vehicle were introduced earlier in Table 3-7. As mentioned in the previous section, the crossties resemble the track foundation stiffness and the modulus of elasticity of the crosstie material is used as a measure of the track stiffness. Figure 3-26 shows a 2D schematic diagram of a single wheel on a rail to be used in the investigation of the influence of railway track stiffness on the wheel-rail contact forces and wear evolution.

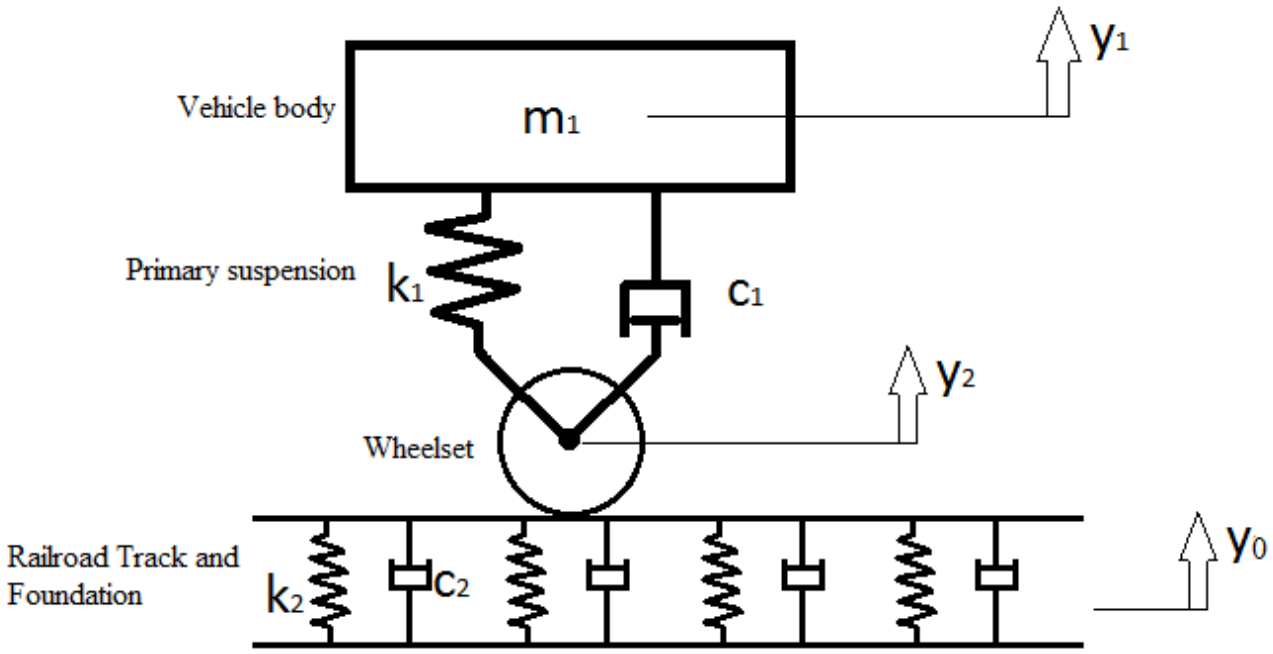

Figure 3-26. 2D schematic diagram of a single wheel rolling on a rail

The model presented above in the 2D schematic diagram (Figure 3-26) was designed in ABAQUS for the static analysis.

Applied interaction properties and contact formulations

A standard static general solution procedure was used in this analysis with a time step on 0.001 seconds. Tangential and normal contact behaviors were defined for the contact interaction properties.

A penalty friction formulation with a static coefficient of friction of 0.4 was defined. A hard contact pressure overclosure was prescribed for the normal contact behavior. A surface to surface discretization method with finite sliding was assigned between the wheel tread surface and the railhead top surface.

A couple constraint was set between the side surfaces of the wheel and a reference point at the wheel center. Tie constraint was set for the contact between the rail bottom surface and the crosstie top surface. This constraint was used as a fastening system between the rail and sleepers. Figure 3-27 shows the applied constraints on the FE static model.

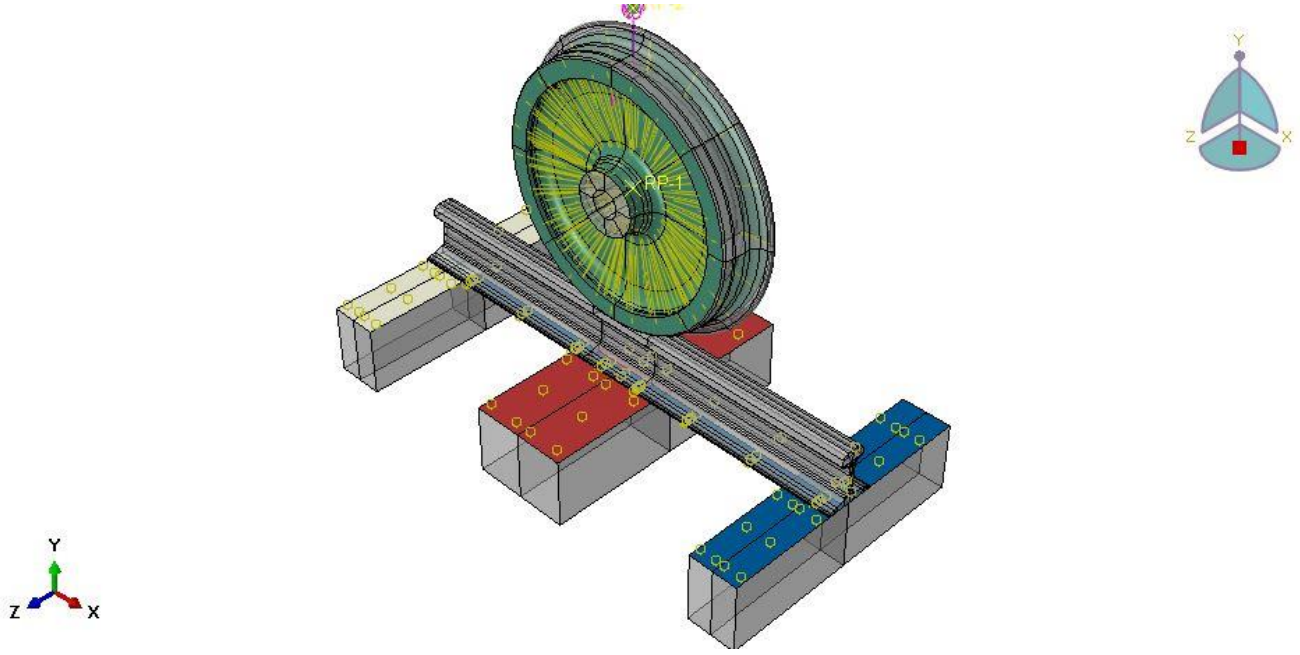

Figure 3-27: Couple and tie constraint application at the static model

The primary suspension system was defined as a spring and a dashpot in ABAQUS. The spring and damper was defined between two reference points, one at the wheel center and the other just above the wheel, and these reference points represent the wheelset and car body respectively. A spring stiffness of 1150 N/mm and a damping constant of 50 N.s/mm were used as primary suspension parameters. Figure 3-28 below shows the spring and dashpot connection between the reference points.

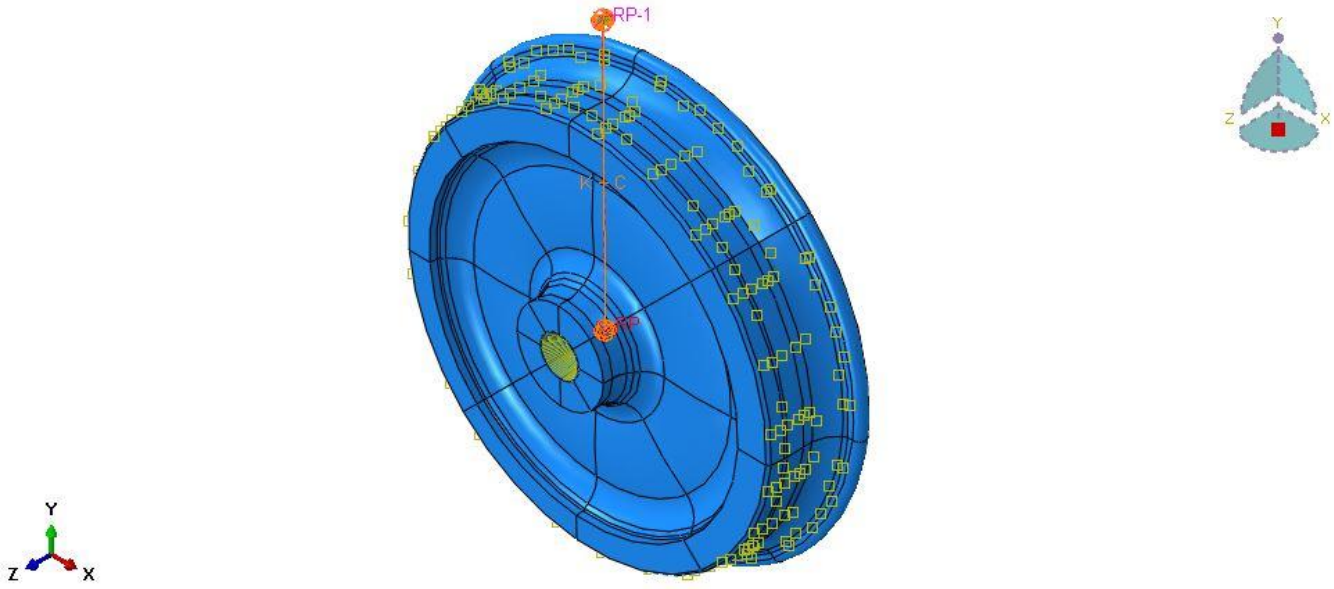

Figure 3-28. A spring/dashpot was defined between the wheel center reference point and another reference point just above the wheel. As indicated by the red line in this diagram.

Applied boundary conditions and loads

The static analysis was executed in a single step called the Pre-Stressing_Step. The vehicle load was applied through a ramp amplitude. The standard static general solution procedure was used in this analysis with a time step 0.001 seconds. A pictorial view of the applied boundary condition is shown in Figure 3-29 below.

- An ENCASTRE boundary condition was applied at the bottom surfaces of the crossties. This was to resemble the ground fixed the railway track support infrastructure.
- Both ends of the railway track were assigned a zero displacement in the longitudinal direction (i.e. x axis direction). This was to portray a large longitudinal length of the rail relative to other dimensions (i.e. lateral and vertical rail dimensions).
- The railway vehicle wheel was only allowed to displace in the vertical direction. The boundary condition was applied at the reference points.
- The Loads were applied at the reference points. A load corresponding to 5 tons quarter car mass was applied at the reference point above the wheel. A load corresponding to 0.875 tons half wheelset mass was applied at the reference point at the wheel center.

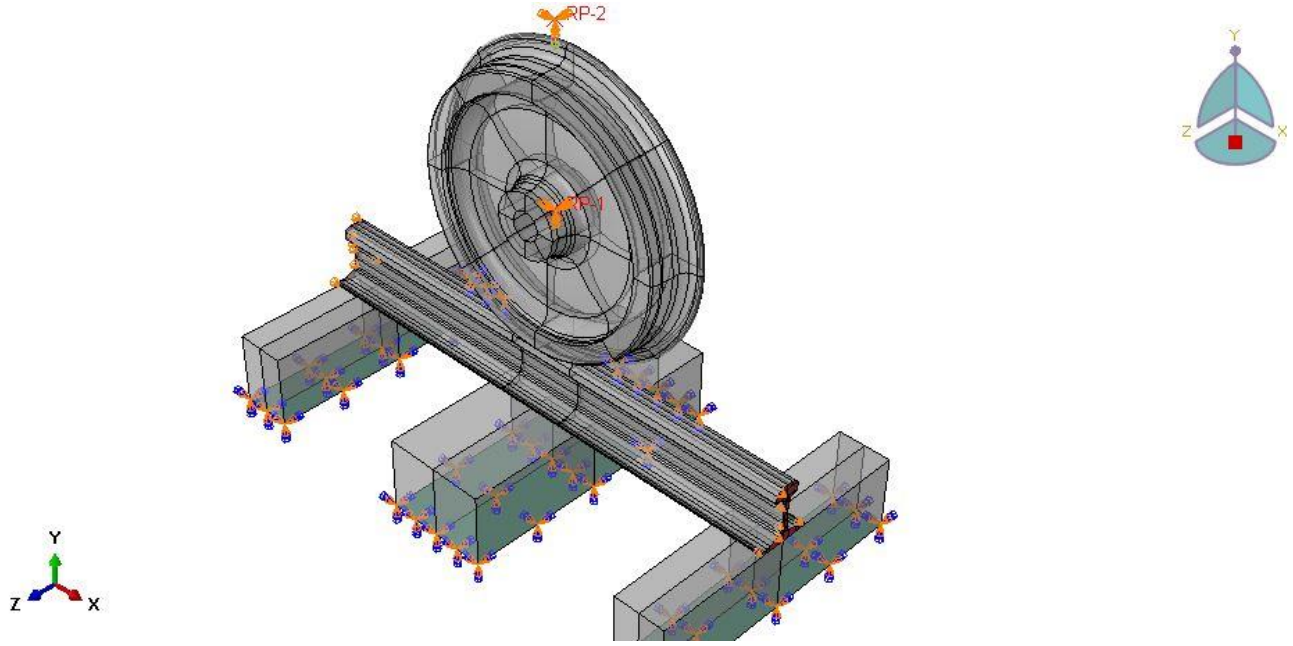

Figure 3-29: Applied boundary conditions

Applied mesh

A fine mesh as assigned in the contact region. An 8-node linear brick with reduced intergration and hourglass control, explicit 3D stress element was used as the mesh element type in this study. Table 3-9 shows the element sizes used in the analysis. Figure 3-30 shows the meshed model.

Table 3-9: Mesh specifications in the contact region

Half plane (Refined mesh in contact area)		Roller (Refined mesh)
Element length	Element width	Cylindrical Edges Element Size
2.5mm	5mm	5mm

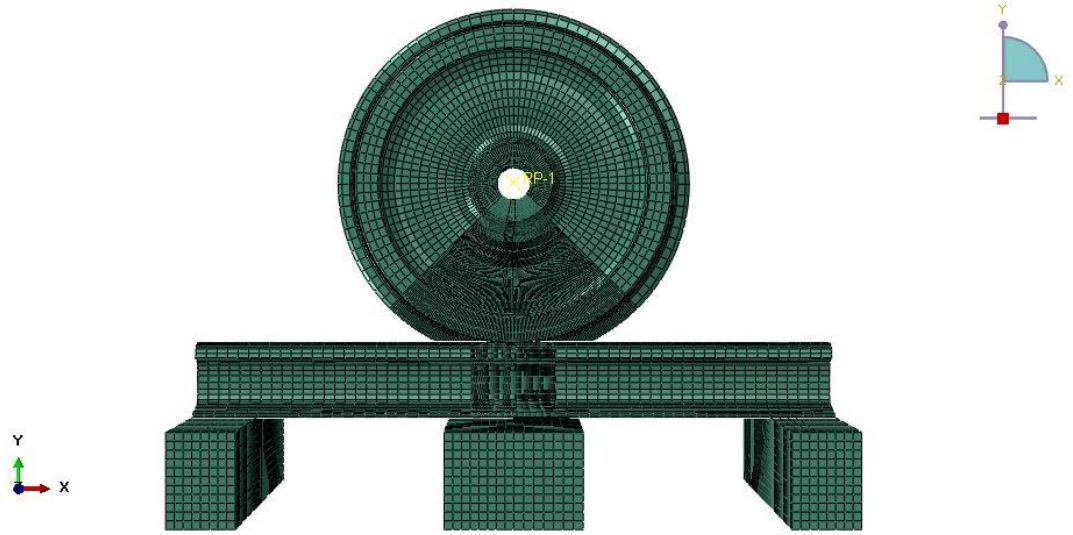

Figure 3-30: Assembled and meshed ABAQUS FE model of a coupled quarter car train- track system with a fined mesh at contact points.

Wheel-rail static contact results

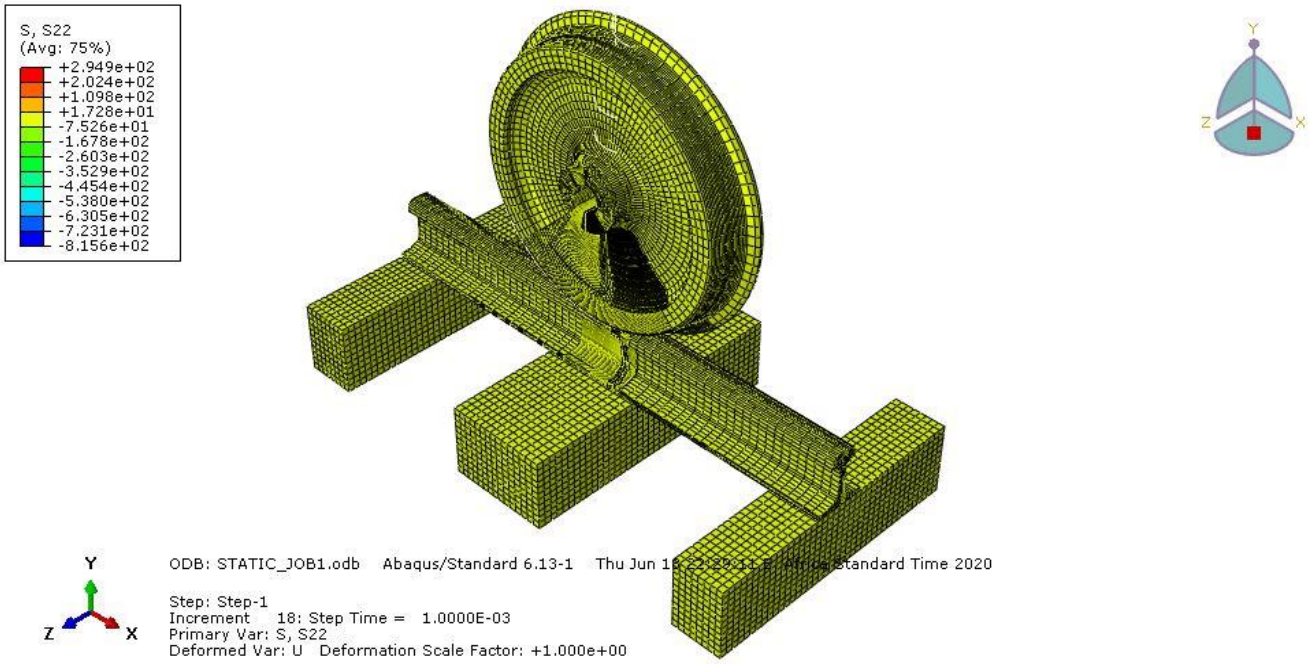

Figure 3-31: Contour plot of a 3D wheel-rail static contact FE model results. The presented results are in MPa.

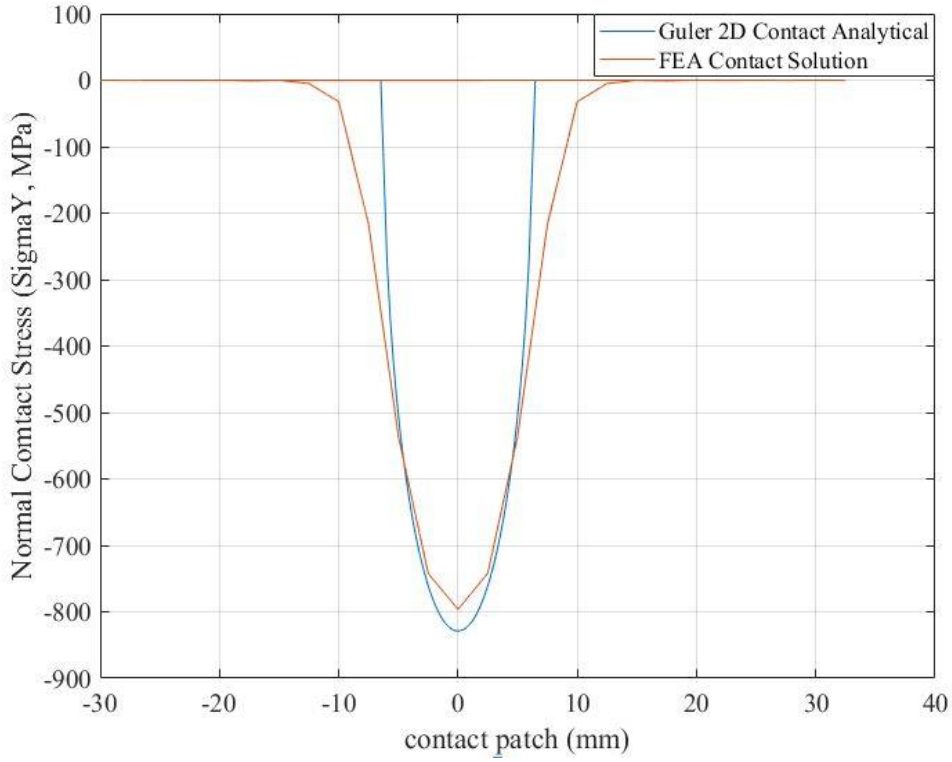

Figure 3-32: Validation of normal contact stress of a 3D static wheel-rail contact Finite Element model using comparisons with the Guler analytical solution procedure.

The 3D wheel-rail static FE model presented in this section was validated against the Guler analytical static solution presented in Section 3.1. A half contact patch dimension of 9 mm in the longitudinal

direction (i.e. $a = 9$ mm) was used in the solution provided in Section 3.1, this was because of the difficulties encountered in the in the FE solution through using small contact patch dimension for a thin roller and half plane. An acceptable agreement in the normal contact stress between the FE solution and the Guler analytical solution was obtained (see section 3.1.). The analysis conducted in this section is based on AALRT vehicle parameters and based on the calculations conducted earlier (i.e. Section 3.1) using the hertz contact theory, the contact patch dimension were calculated to be $a = 6.3$ mm and $b = 5.1$ mm. Figure 3-32 shows the analytical and FEA solutions for the normal contact stress using $a = 6.3$ mm. There is an agreement in the results presented in Figure 3-32 which provides the validity of 8-node linear brick, explicit 3D stress elements with reduced intergration and hourglass control, in contact analysis. The element sizes shown in Table 3-9 are also valid to analyse the contact of the model size under considartion.

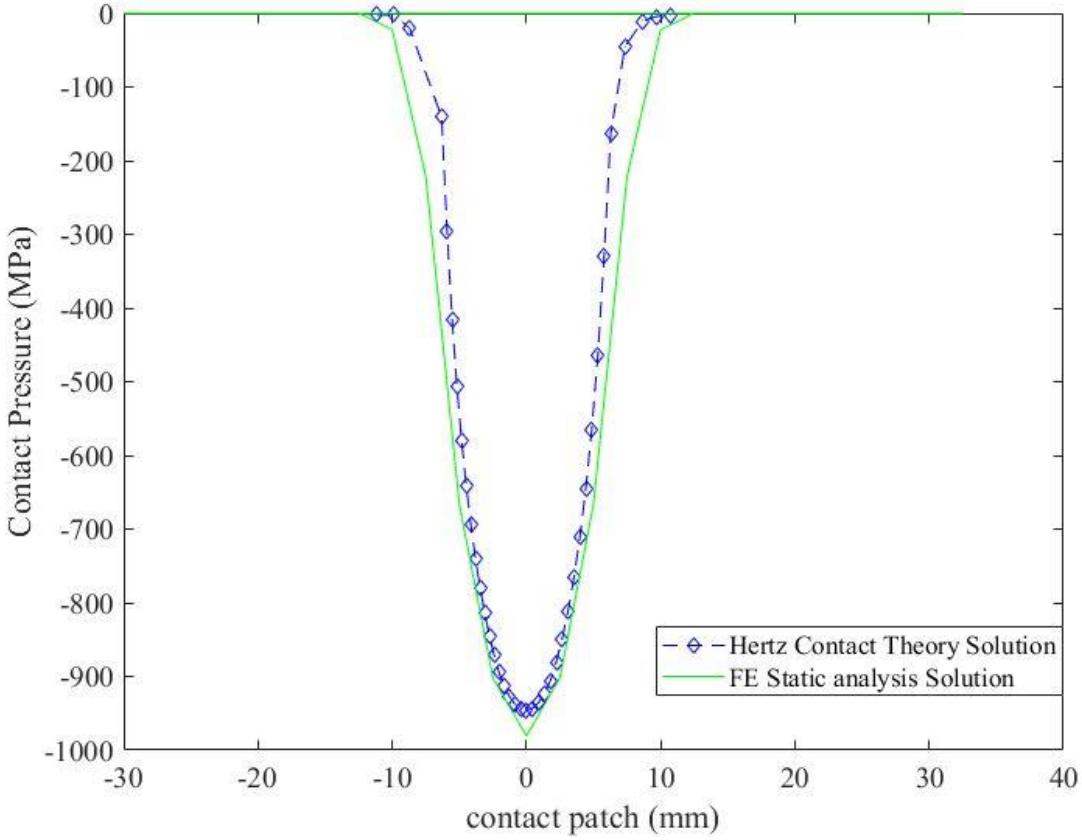

Figure 3-33: Validation of contact pressure of a 3D static wheel-rail contact Finite Element model using comparisons with the results obtained from Hertz contact theory solution procedure.

The Hertz contact pressure based on AALRT vehicle parameter was calculated in Section 3.2 and a 3D plot of the pressure distribution in the contact patch is shown in Figure 3-3. A finite element analysis using the results obtained from the Hertz solution was conducted in the first part of Section 3.2.2. The 2D plot of contact pressure distribution for the FEA solution is shown in Figure 3-23 which have the same absolute maximum contact pressure value as the one presented in Figure 3-3, as

expected. The results shown in Figure 3-23 are used to validate the wheel on a rail finite element model to be used in this analysis. The contact pressure on the model presented in Figure 3-31 was validated on a plot in Figure 3-33. The graph shown in Figure 3-23 together with the contact pressure distribution in the contact interface of the model shown in Figure 3-31 are plotted on a same plane in Figure 3-33. The two graphs in Figure 3-33 shown the same behavior and they have approximately the same minimum pressure value. Furthermore the contact patch dimensions are within the same range. Therefore the results presented in this section also validates that 8-node linear brick, explicit 3D stress elements with reduced intergration and hourglass control are eligible for contact analysis. In addition the element sizes shown in Table 3-9 are also valid for the contact analysis of the model size under considartion.

3.2.4 Evaluation of the equivalent track stiffness

A literature review of both methods used in the determination of the equivalent track stiffness and the strains occurring in the rail track web, was conducted in Section 3.2.1. In this analysis the equivalent track stiffness is determined in a FE simulation software environment based on similar track web strain results in the simulation environment as in field experiments and field observations from previous related studies. Based on a previous experimental research, which matched computational models and experimental results, (i.e. [60] Nkundineza and Turner) it was shown that the equivalent track modulus in the simulation software was in hundreds on Mega-Pascal's. Therefore a range of equivalent track stiffness between 200 MPa and 700 MPa was used in a trial and error method to determine the equivalent track stiffness to be used in the FEA. A track web strain of 0.206 ppm (0.206 part per million) was used to approve the equivalent track modulus used in this study. This strain value was based on a literature survey conducted in Section 3.2.1.

As mentioned earlier, the crosstie material modulus of elasticity (i.e. crosstie modulus in short) resembles the equivalent stiffness of combined rail fasteners, pads, cross-ties, and all substructure elements in the simulation environment. A uniform crosstie modulus was used for all the models ran in this section. The FE static analysis shown in Section 3.2.3 was ran for several different values of the crosstie modulus. A plot of rail track web maximum strains (i.e. strains in the vertical direction, $E22$) against crosstie modulus was made. The location of the rail track web strains collected from the FEA is shown in Figure 3.34 below. The vertical strain results were collected from the FE solution at nodes located just above the middle crosstie and below the loading point.

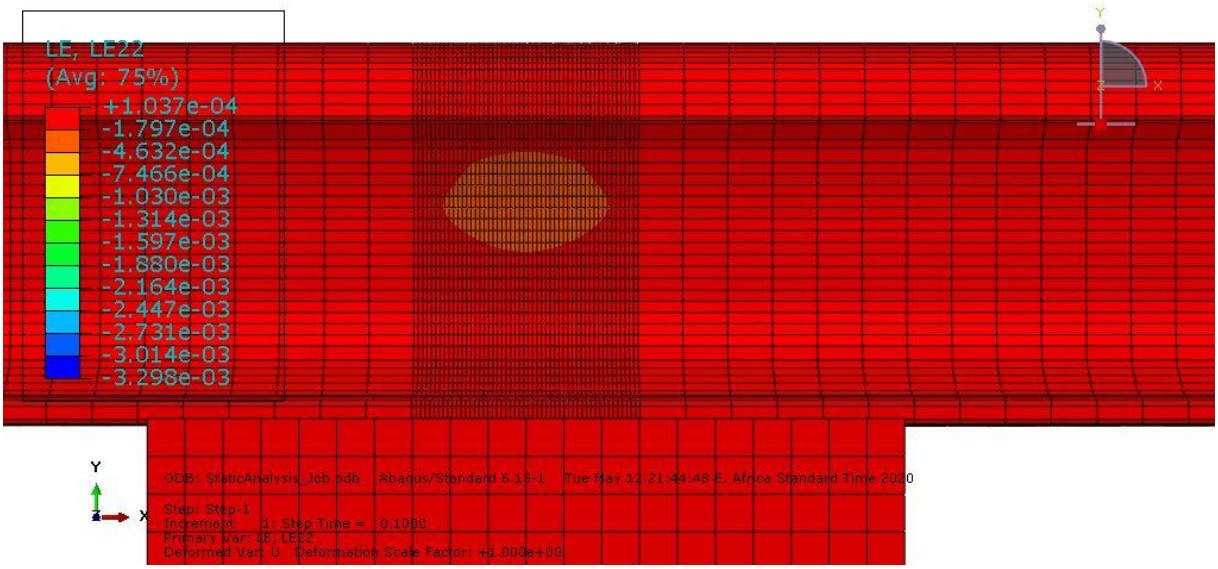

Figure 3-34: Location of rail track web strain data collection from the FEA solution (i.e. on nodes just above the middle crosstie and below the loading point).

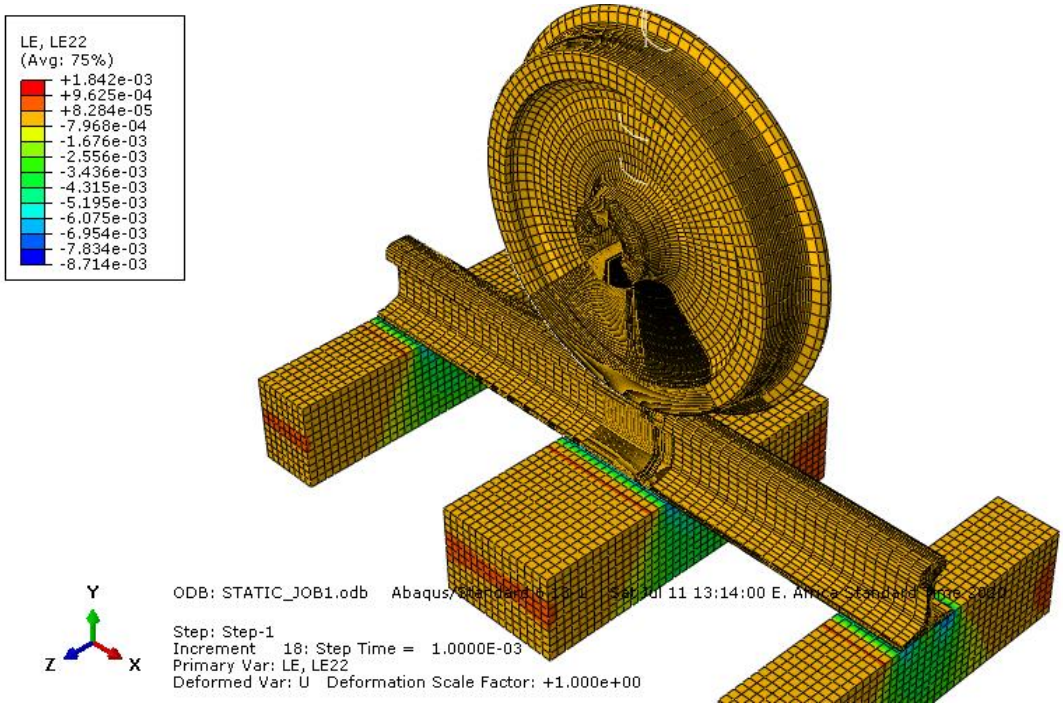

Figure 3-35: Strain results for a train-track interaction model for a crosstie modulus of 500 MPa

Figure 3-35 shows the FEA model set up in the determination of the equivalent track stiffness in terms of crosstie modulus. The rail vehicle wheel was removed for better visualization of vertical strains contour plots and location of critical strains in the track web. Six FEA static models with an ascending crosstie modulus from 200 MPa to 700 MPa were ran in ABAQUS and the strains occurring the rail track web were collected from each model.

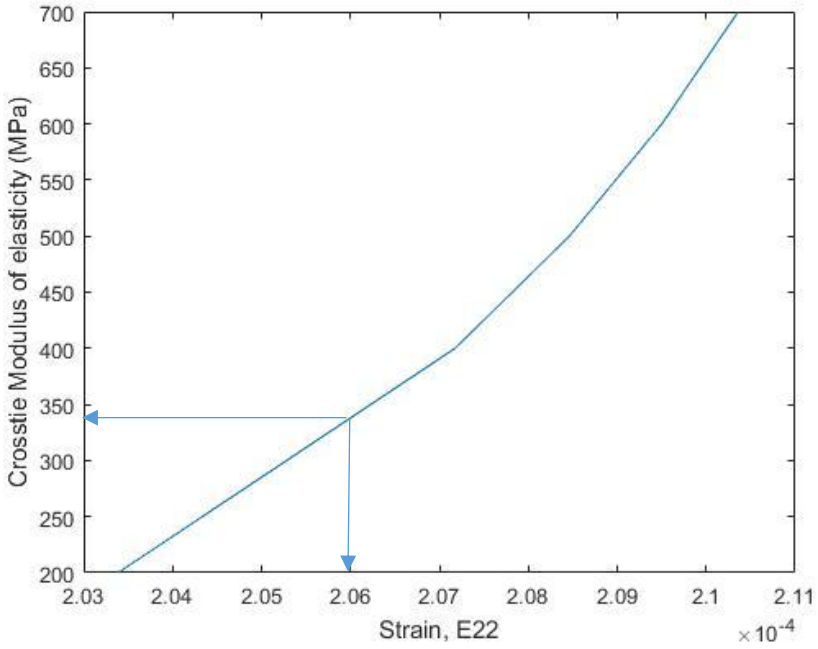

Figure 3-36: A plot of crosstie modulus of elasticity versa vertical strains in the rail track web

It was observed in Figure 3-36 that the rail track web strains increases with increase in crosstie modulus. This characteristic is true since at high track stiffness, track foundation deformations are very small, therefore the railway track deforms more in response to loading conditions, and vice versa. A rail track web strain of 0.206 ppm was used in this analysis which corresponds to a crosstie modulus around 350 MPa according to Figure 3-36. A value of 350 MPa is used as the equivalent crosstie modulus in ABAQUS dynamic simulations. The track stiffness variation in the simulations is achieved by varying the crosstie modulus.

3.3 Finite element dynamic model design and validation method

To investigate the influence of railway track stiffness spatial variation on wheel-rail contact parameters and wheel tread wear behavior, a railway vehicle wheel was rolled on a rail for a finite distance. The railway track is supported by three crossties as in the static analysis presented in Section 3.2.3. The crosstie modulus of elasticity (i.e. crosstie modulus for short) is used to resemble the track stiffness in the simulations. The crosstie modulus is varied in the dynamic analysis to portray the variation in track stiffness.

Model design

The model used in the dynamic analysis is shown in Figure 3-37. The model set up is similar to the one shown earlier in the static analysis. In addition to the static model presented in Section 3.2.3 additional boundary conditions are added to the FE dynamic model and the analysis was carried out in

two steps. The wheel was rolled on the rail across the middle crosstie. It was rolled a distance of 800 mm with a 0.0288 seconds time step. A fine mesh was defined in the last 100 mm rolling distance. Tangential and normal contact behaviors were defined for the contact interaction properties. A penalty friction formulation with a static-kinematic exponential decay coefficient of friction (COF) was defined. A static COF of 0.4, a kinematic COF of 0.32 and a decay coefficient of 6 were set based on literature data [29].

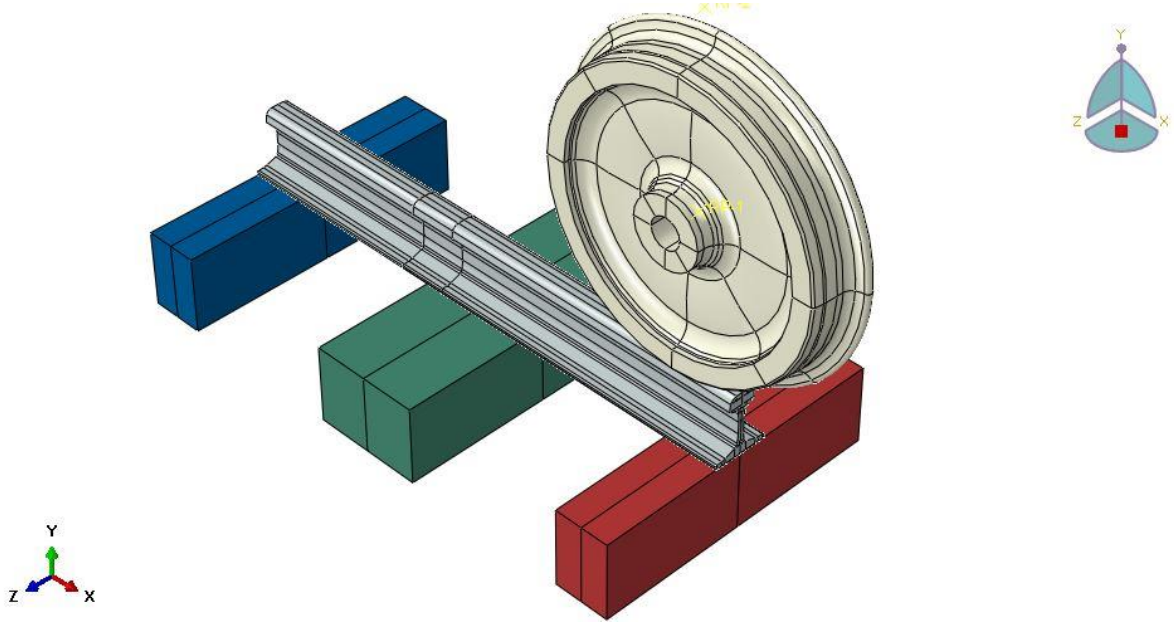

Figure 3-37: FEA dynamic model setup

Applied boundary conditions and loads

The analysis was divided into two steps. The first step is the pre-stressing step where the loads are applied. This is followed by the rolling step where the roller is roller through a finite distance. The applied boundary conditions are dependent on the step and a propagated or modified in the following step.

Two dynamic explicit steps were created for the rolling contact analysis.

Step_1 Pre-Stressing A downward force F_y was applied at the roller center with a linear amplitude.

$F_y = \text{sprung force} + \text{unsprung force} = (5 \text{ tons} + 0.875 \text{ tons}) \times 9810 \text{ mm/s}^2$

- The bottom surfaces of the crossties were constrained in all degrees of freedom to zero.
- The wheel was allowed only to move in the vertical direction. The boundary condition was applied on the reference point on the center of the wheel.

- The side surfaces of the wheel were restricted from moving in the lateral direction (i.e. z axis direction)
- A couple constraint was defined between the side surfaces of the wheel and a reference point on the wheel center.
- The ends of the railway track were restricted to move in the longitudinal direction.

Step_2 Rolling-step. A rotation angle of 2.1 radians in the positive z-direction was specified on the reference point on the wheel center.

- A torque was assigned to a reference point on the center of the wheel. The traction force was calculated as $F_y \times 0.75 \times 0.32 = Q$,
  where; 0.4 is the friction coefficient and
  0.75×0.4 is the traction coefficient.
  The torque = $Q \times$ axel radius,
  where; axel radius = 100 mm.
- The vertical loads applied in Pre-stressing step were kept constant in this step.
- A longitudinal displacement of 800 mm in the rolling direction was also defined.
- The side surfaces of the roller were still restricted to move in the lateral direction

To study the track stiffness spatial variation influence on wheel rail contact parameter, the modulus of elasticity on the middle crosstie is varied while the modulus of elasticity of the side crossties is kept constant. The variation of the middle crosstie modulus relative to the side crosstie modulus is defined in terms of a ratio (i.e. middle crosstie modulus: side crosstie modulus). In this study this ratio is going to be referred to as the crosstie ratio. An equivalent crosstie modulus of 350 MPa was deduced earlier. The side crossties were kept at the equivalent crosstie modulus throughout the analysis. A crosstie ratio above 1 (crosstie ratio>1) signifies the track transition from soft track stiffness to a hard track stiffness section while the crosstie ratio greater than 1 (crosstie ratio<1) shows a transition from a hard track stiffness to a soft track stiffness section. The influence of the crosstie ratio on wheel rail contact parameters is explored using the procedure outline in this section.

3.4 Wear analysis

The Archard wear model will be used in this study to calculate the wear volume. Uniform wear will be assumed therefore the material removed will be assumed to be equally distributed around the wheel tread this will simplify the wheel geometry update procedure.

$$V_W = K\frac{s.N}{H} \qquad \text{Eq. 3-11}$$

Wear Volume	V_w
Wear coefficient	K
Hardness	H
Sliding distance	s
Contact pressure	N

The wear volume is calculated at various track stiffness and its influence on wheel tread wear is deduced. Comparisons of wheel tread wear characteristics at uniform track stiffness versa varying track stiffness is made.

3.5 Conclusion

In this section an overview of the research design and methodology was provided. Analytical formulations of the rolling contact problem were provided and elucidated. The wheel-rail contact patch dimensions and contact pressure distribution for AALRT were calculated based on the Hertzian contact theory. Analytical static and rolling contact solutions were provided by Guler and Alinia methods respectively. A simple roller on a half plane FE model was validated against the analytical solutions. The FE contact solution, the mesh element type and mesh element size were validated. A 3D model of a wheel on a rail supported by crossties was modelled in solid works and imported to ABAQUS. The track stiffness is resembled by the crosstie material modulus of elasticity (i.e. crosstie modulus) in the simulations. Using literature data the equivalent crosstie modulus was deduced in the simulation environment through a set of finite element static analysis. The strains occurring the railway track web were the determining factor for the equivalent crosstie modulus. In addition, the outline of the model to be used in the rolling contact analysis at varying crosstie modulus is explained. Furthermore the wear model to be adopted in this study was also explained.

4 COMPUTATIONAL RESULTS: INFLUENCE OF NON-UNIFORM TRACK MODULUS ON WHEEL-RAIL CONTACT STRESSES, FORCES, AND WEAR

This chapter presence the results and findings of the research as well as a discussion of the results. An insight into the influence of railway track stiffness spatial variation on wheel-rail contact parameters such as contact force, contact area, contact stress etc. is provided. In addition the period of contact forces at varying track stiffness was analyzed. Moreover the impact factor of wheel-rail contact forces at varying crosstie moduli ratio was discussed. The frictional forces acting on the wheel-rail interface were also presented in this section. Contact moments and shear stresses acting on both the wheel tread and the railhead surface were extracted and plotted again the rolling time. Furthermore, the slip velocities at each time increment are extracted from the FE model repetitively at different crosstie moduli ratios. Plots were also made at varying crosstie modulus (i.e. Track stiffness) and their trend was discussed. The slip distance was computed at each time increment and used in the wear calculations.

4.1 Normal contact forces and stresses variation with varying track stiffness ratio

Different finite element models with varying crosstie moduli ratios were ran in ABAQUS. As explained in chapter 3, the modulus of elasticity of the side crossties was kept constant at the determined equivalent crosstie modulus value, while the modulus of elasticity of the middle crosstie was varied. The crosstie modulus ratio was calculated as the middle crosstie modulus divided by the side crosstie modulus. A modulus ratio above 1 shows a transition from a soft track (i.e. lower track stiffness) region to a stiff track (i.e. high track stiffness) while a ratio below 1 shows the exact opposite. The results from the ABAQUS finite element model were extracted at each time increment by utilising the ABAQUS scripting techniques. Python codes were written to extract different results from the ABAQUS Output DataBase file. The python codes were programmed to extract on the maximum

contact quantities (i.e. contact pressure, contact force, contact moments, shear stresses and forces) at each time increment. The scripting codes used for results extraction are presented in the Appendix. Different plots of results from the FE wheel-rail contact model at each time increment were made.

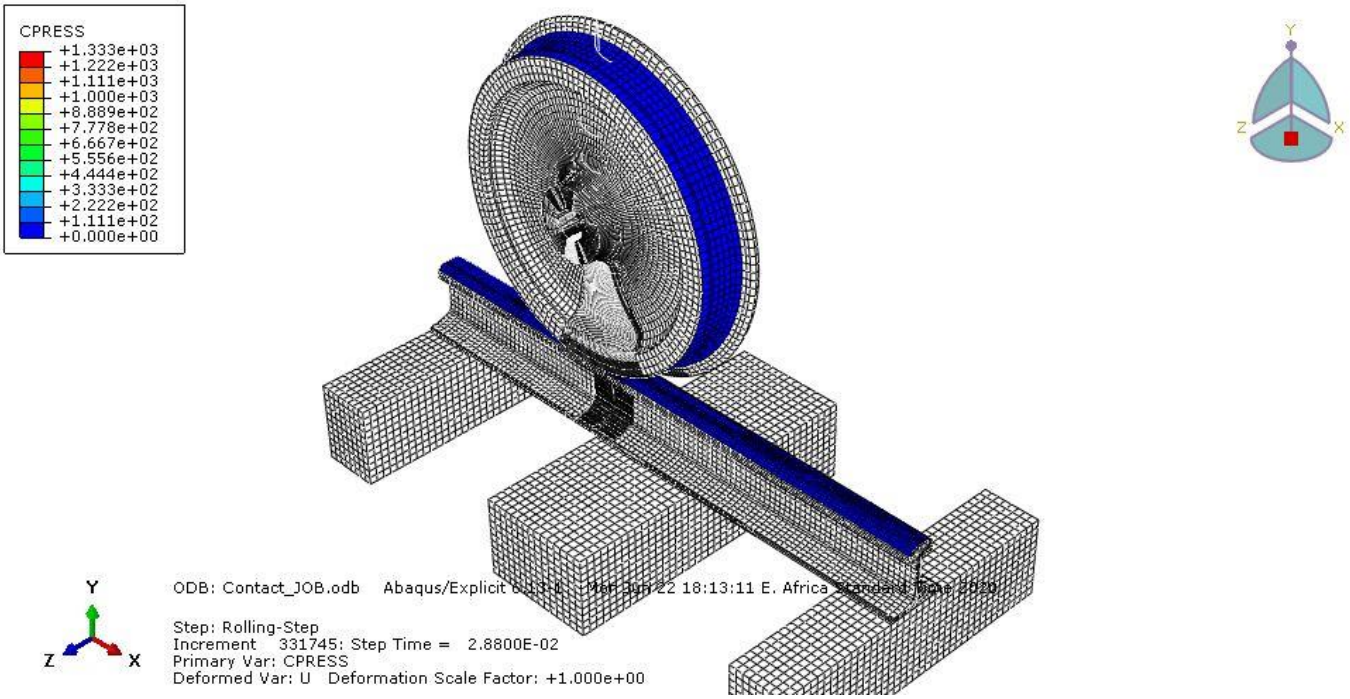

Figure 4-1: ABAQUS 3D FE model displaying contact pressures

The 3D ABAQUS FE model displaying contact pressure results is depicted in Figure 4-1. A single point contact was defined is this study between the wheel tread and the railhead top surface. Therefore the intercation was prescribed only to the contacting surfaces. The contact parameters were extracted after every 0.0001 seconds time increment in the rolling step. Different plots of contact quantities at each time increment in the rolling step are presented in the following sections.

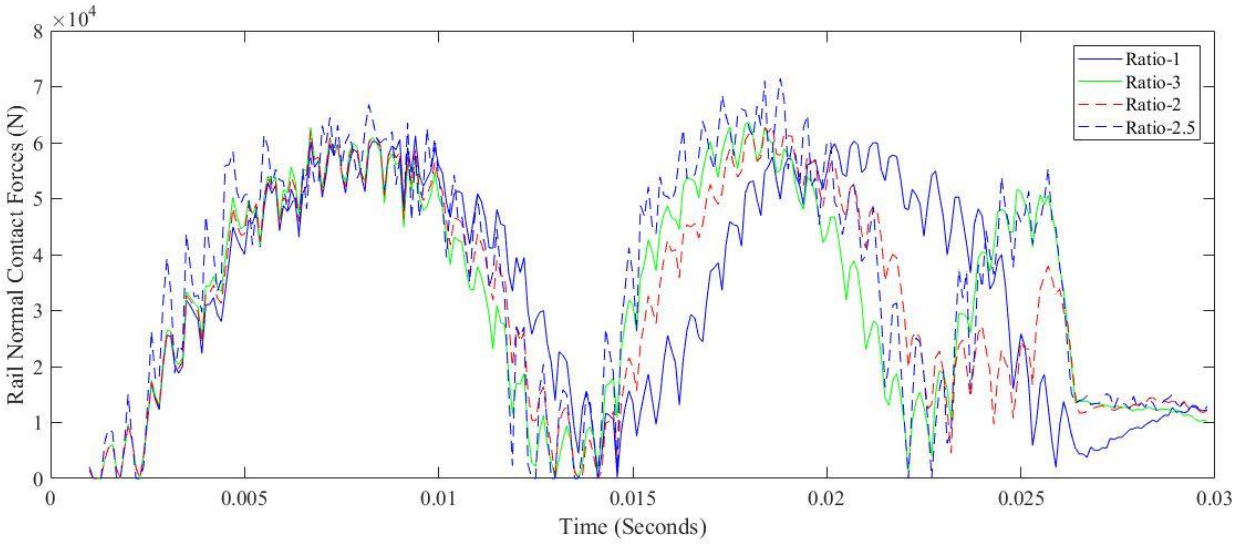

(a)

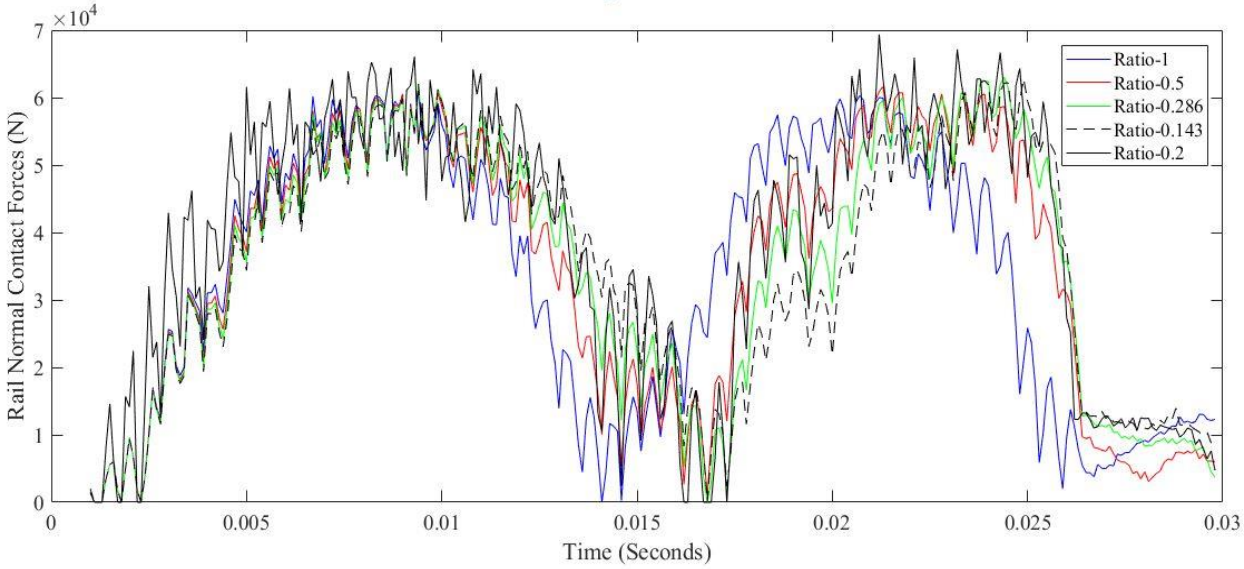

(b)

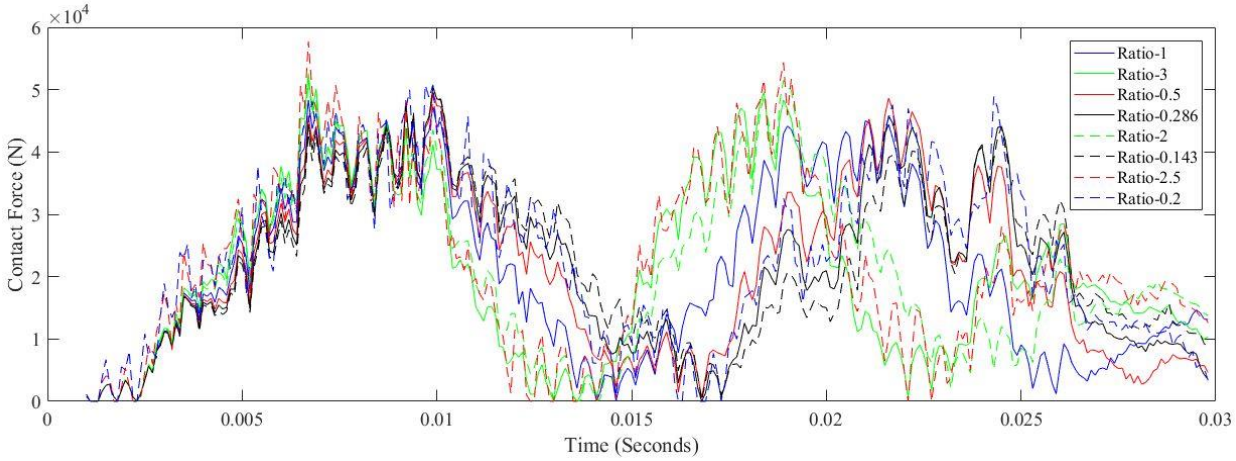

(c)

Figure 4-2: A plot of wheel-rail contact force magnitudes at each time increment in the rolling step and at varying crosstie modulus ratio. Railhead top surface normal contact force at varying crosstie modulus ratios (a) Above 1 and (b) Below 1. (c) Wheel normal contact force at varying crosstie modulus.

Figure 4-2 (a), (b) and (c) shows plots of the contact force magnitudes against the time increment at various crosstie modulus ratios. A time step of 0.0288 seconds was set for the rolling step and the results were extracted for every 0.0001 seconds of time increment as mentioned earlier. The FE model with a crosstie modulus ratio of 1 resembles the uniform track stiffness (i.e. rigid track support structure) that has been used by various previous researchers to predict the behavior of wheel-rail contact forces and stresses. The influence of track stiffness spatial variation on wheel-rail contact parameters was identified through comparisons with the FE model at uniform crosstie modulus. From Figure 4-2 it can be seen that the wheel-rail contact force is sinusoidal meaning that the wheel is bouncing on the rail after a certain period. This bouncing period is affected by the track stiffness

variation. At a transition point from a soft track (i.e. low track stiffness) to a stiff track (i.e. high track stiffness, crosstie modulus ratio above 1) the period of the contact forces is reduced which means the wheel bounce on the rail more often. At a transition point from hard to soft track (i.e. for crosstie modulus ratio below 1) the period of contact forces is increased relative to uniform track modulus. In addition there is a slight variation in the maximum contact force magnitude at different crosstie modulus ratios. This can be well explained by the impact factor plots shown in Figure 4-3.

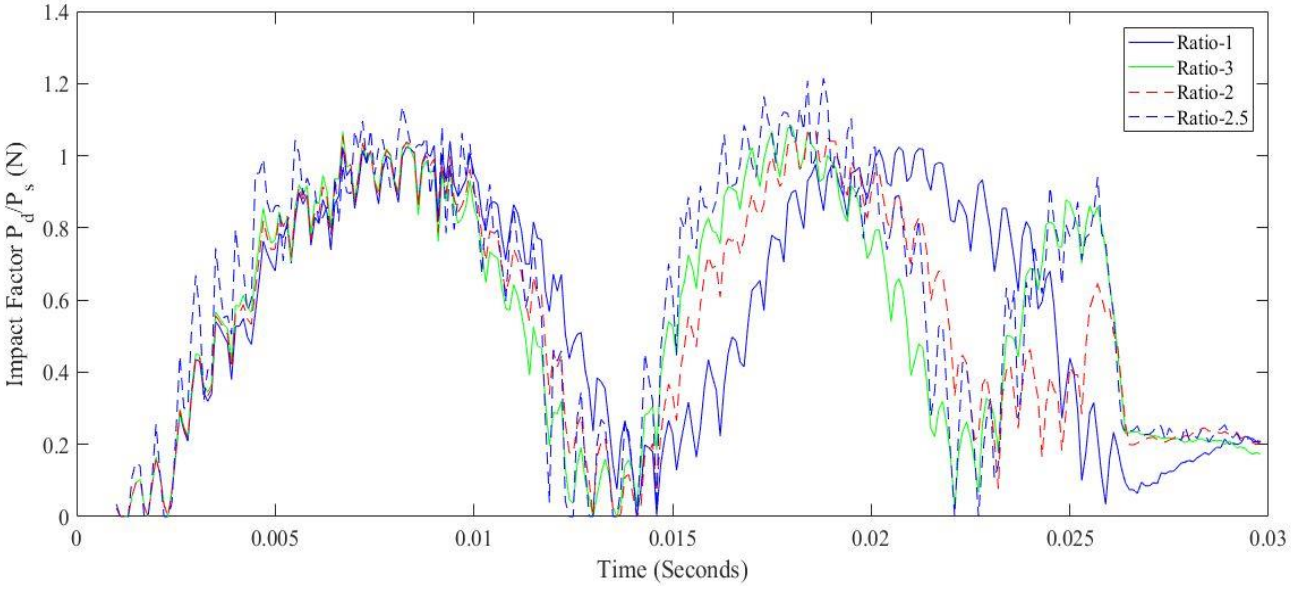

(a)

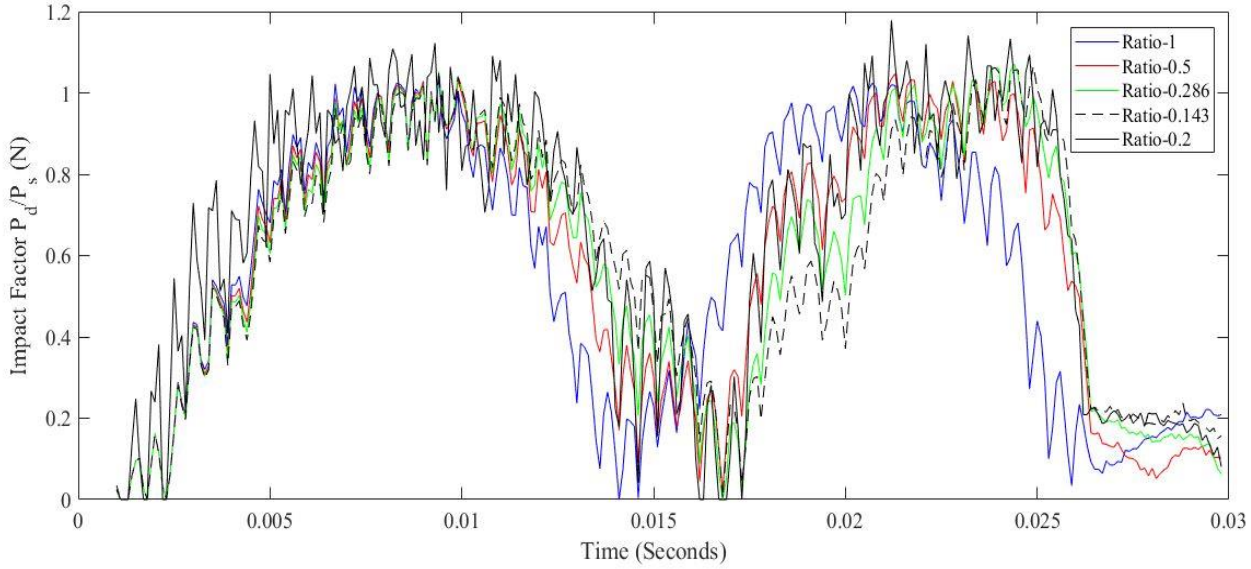

(b)

Figure 4-3: A plot of contact force impact factor at varying crosstie modulus ratio. (a) Crosstie modulus ratios above 1. (b) Crosstie modulus ratios below 1.

The impact factor is a dimensionless parameter calculated as the quotient of dynamic and static wheel-rail contact forces. From Figure 4-3 it can be seen that there is a high impact factor at crosstie modulus ratios above 1. This is in line with the observation made earlier on the period of contact forces. A transition from soft track stiffness region to a hard track stiffness region increases the wheel bouncing frequency in the rail which in turn increases the impact factor. Moreover a stiff track resist deformation which increases the wheel-rail contact forces impact. Lower impact factors are observed when the wheel travels from a harder track section to a softer section (i.e. crosstie ratios below 1) relative to soft-hard transition (i.e. crosstie ratio above 1). The track flexibility at low track stiffness values allows for the rail and its support structure to deform and damp some of the excitations exerted by a rolling wheel. Therefore lower impact factors at hard-soft track stiffness transition relative to soft-hard track stiffness transition, are expected. In addition the flexibility of the track allows longer time intervals of wheel and rail contact before bouncing occurs. This increases the period of the contact force sinusoidal curve as shown in Figure 4-2. Both impact factors at crosstie modulus ratios above and below 1 (i.e. at varying track stiffness) are more than the impact factor at uniform crosstie modulus (i.e. uniform track stiffness). Although more severe contact conditions occurs at a transition from soft to hard track stiffness than at hard to soft, both scenarios are still severe if they are compared with uniform track stiffness.

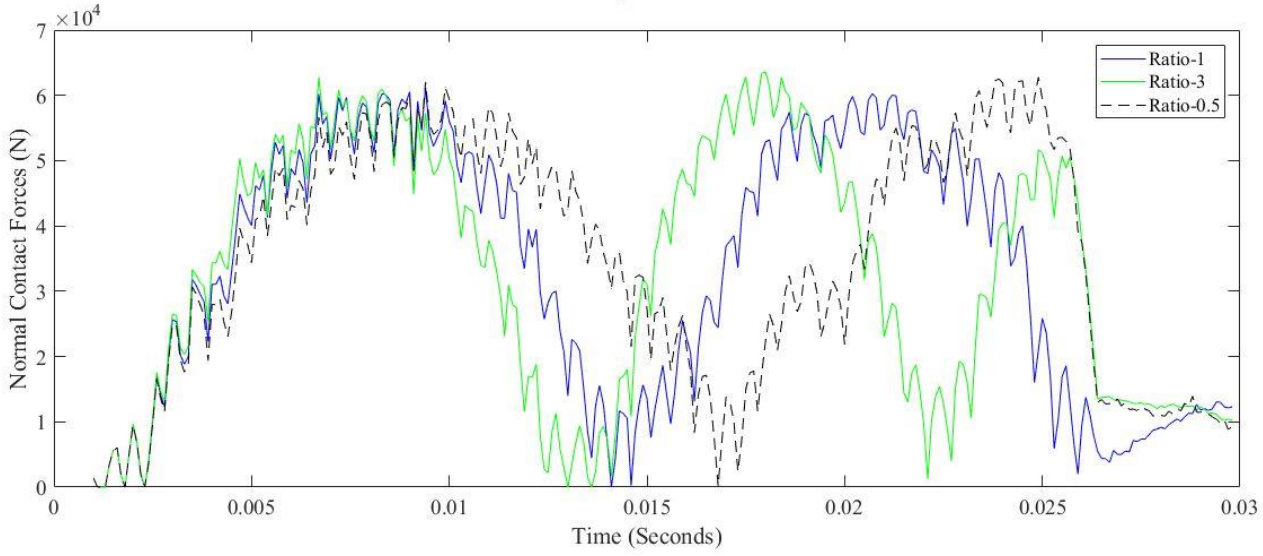

(a)

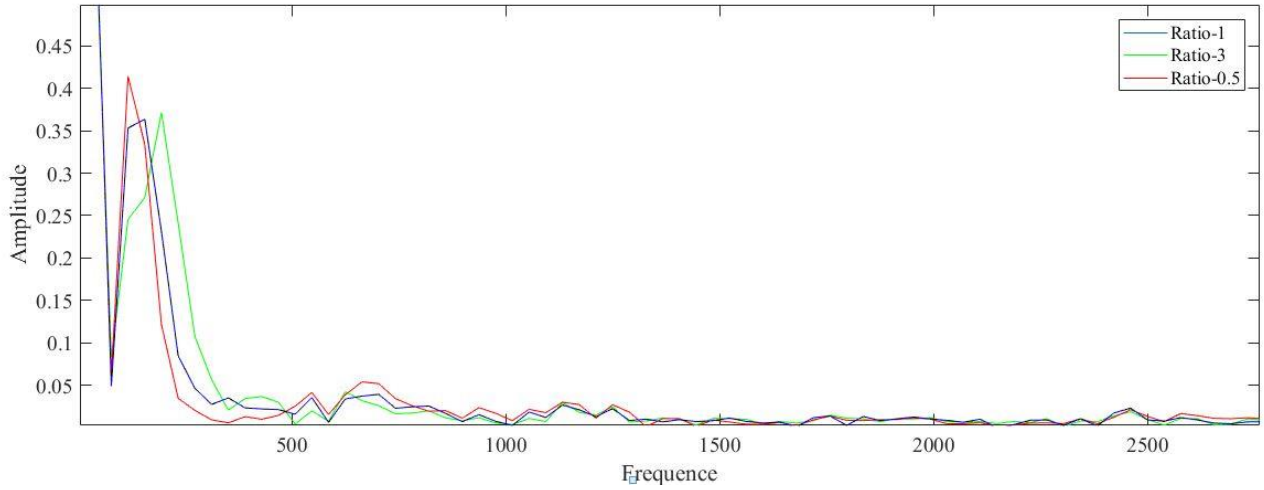

(b)

Figure 4-4: (a) Visualization of normal contact forces fundamental frequencies at different crosstie modulus ratios. (b) A plot of normalized contact force amplitude against frequency spectrum at different crosstie modulus ratios

The contact force fundamental frequencies are plotted against the normalized contact forces at different crosstie moduli ratios as shown in the Figure 4-4 above. The frequencies of wheel-rail contact forces at various crosstie modulus were sketched on a single graph. For the 800 mm distance under study a frequency spectrum of 0 to 2500 Hz is observed through the use of the Fast Fourier Transform function in Matlab. The frequency versus normalized contact force plots at different crosstie modulus are almost the same with a slight significant difference in the amplitude. High fundamental frequencies are found at crosstie modulus ratios below 1. Due to high track flexibility at transitions points from hard to soft track stiffness, and the increase in allowable track deformations increases the fundamental frequencies relative to uniform track stiffness and for transitions between soft to hard track stiffness. The fundamental frequencies at soft to hard track stiffness are still higher relative to uniform track stiffness.

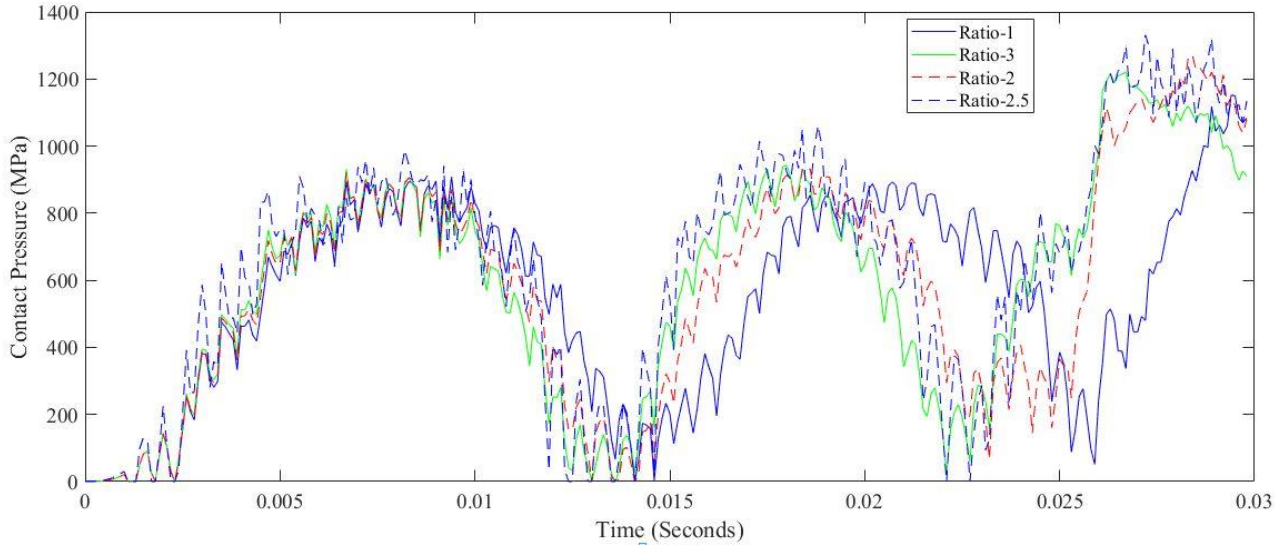

(a)

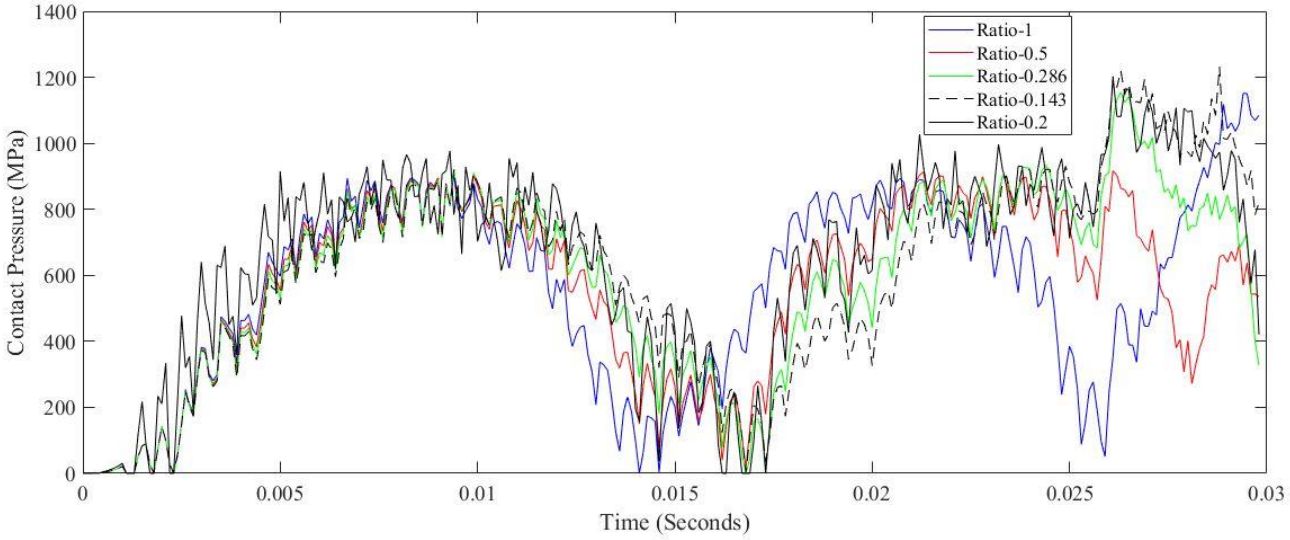

(b)

Figure 4-5: A plot of wheel-rail contact pressure at each time increment in the rolling step for various crosstie moduli ratios. (a) Crosstie modulus ratios above 1. (b) Crosstie modulus ratios below 1.

The contact pressures at each time increment and various crosstie modulus ratios are plotted as shown in Figure 4-5. A similar contact pressure behavior is observed in the time interval between 0 and 0.01 seconds in the rolling step, at different crosstie moduli ratios. This is because the side crosstie are kept at the determined equivalent crosstie modulus while the modulus of the middle crosstie is varied to portray a variation in track stiffness. Despite almost similar behaviors in contact pressure within the mentioned time interval high contact pressure magnitudes are still observed at varying track stiffness relative to uniform track stiffness.

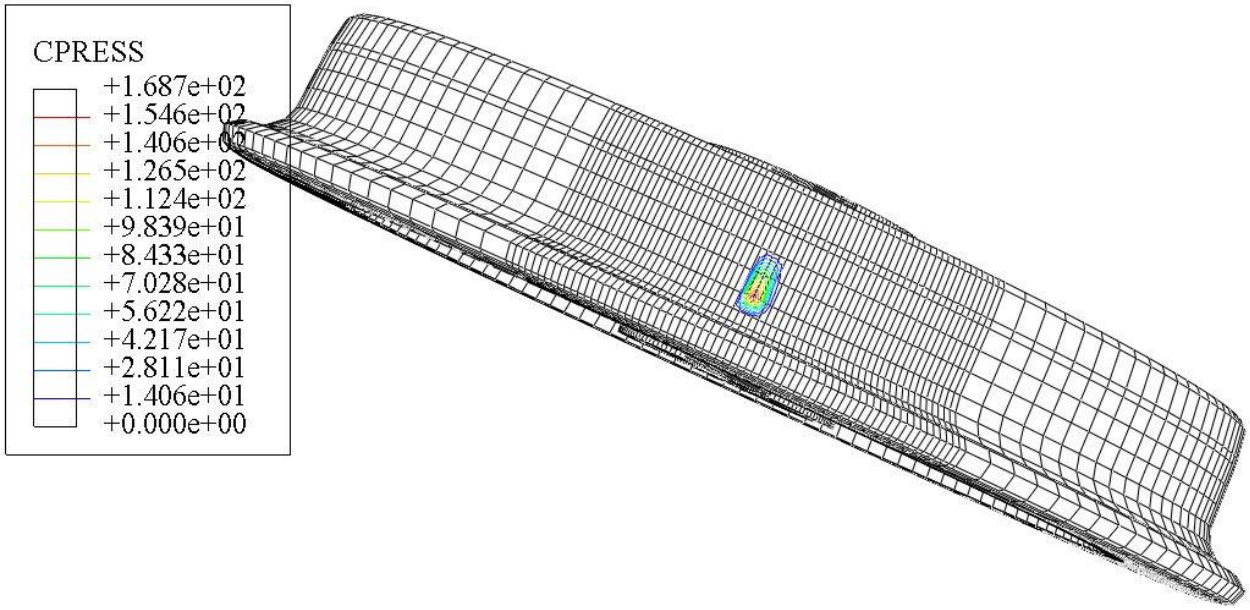

(a)

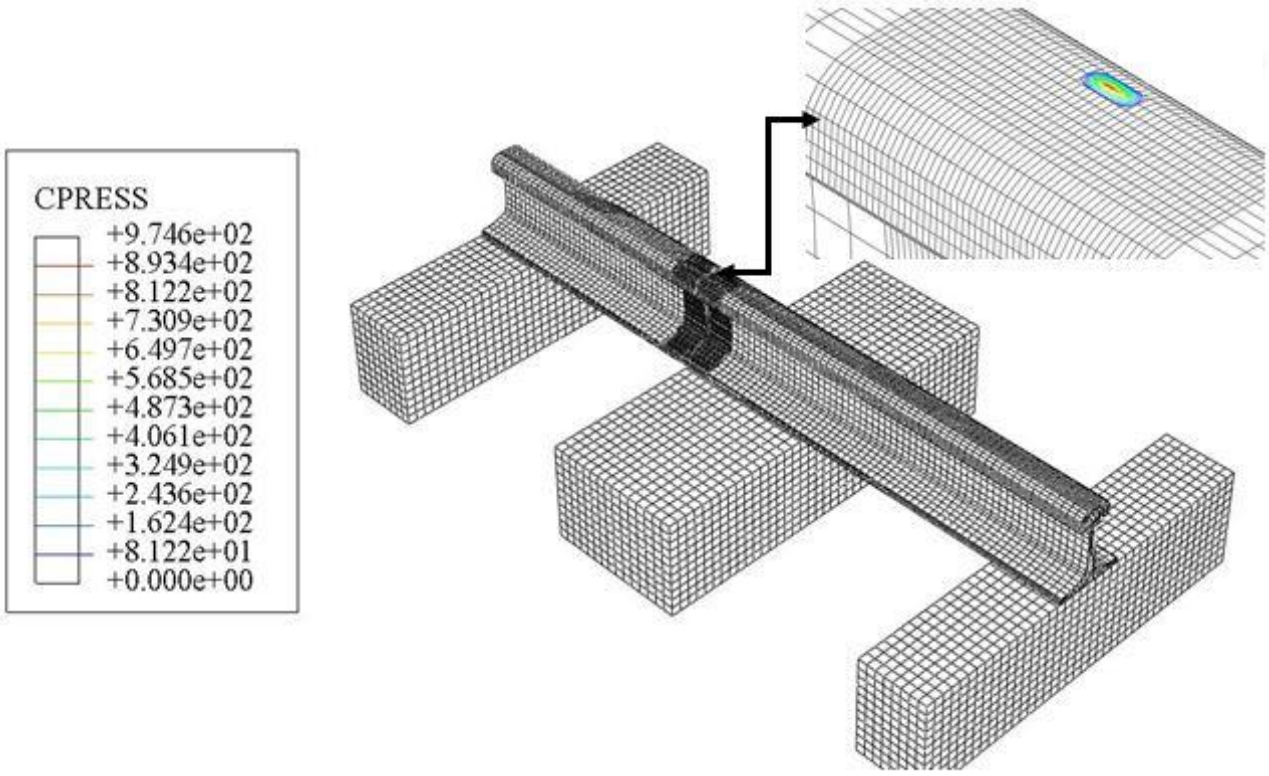

(b)

Figure 4-6: Geometry of the contact area and contour plots of contact pressure distribution (a) On the wheel tread and (b) Railhead top surface

Figure 4-6 shows the geometry of the contact area on the wheel tread surface and the railhead. The contact patch area is still elliptical on the wheel tread surface similar to the railhead top surface contact

area, but the major axis of the ellipse is in the transvers direction on the wheel tread surface while the major ellipse axis is in the longitudinal direction for the railhead top surface contact area.

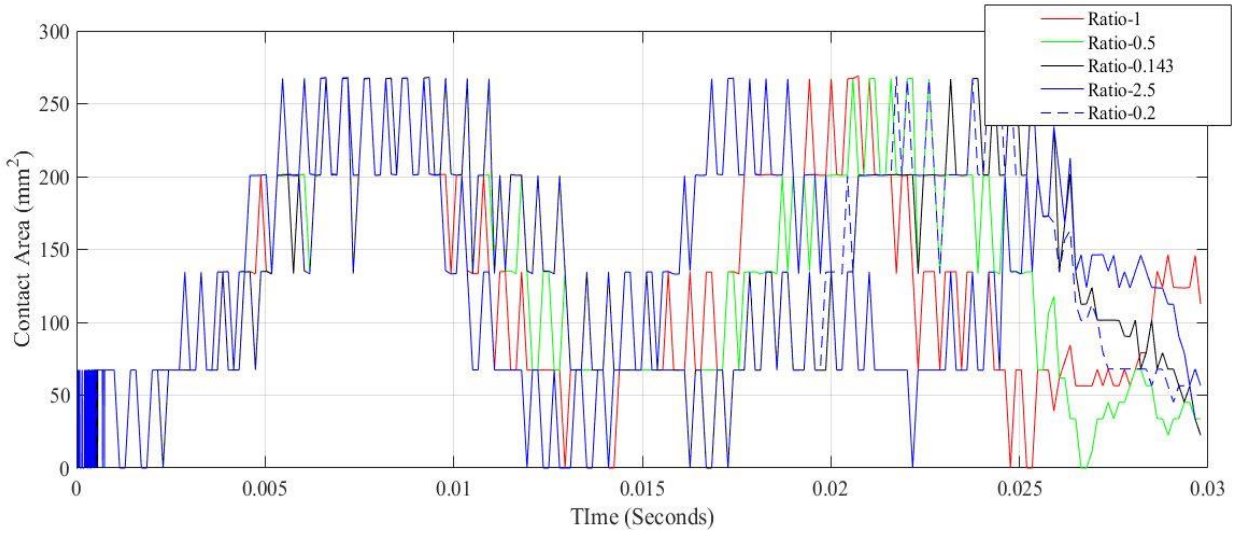

Figure 4-7: Wheel-rail contact area at every time frame and at different crosstie modulus ratios

Figure 4-5 and Figure 4-7 respectively shows the contact pressure and contact area plots at each time increment in the rolling step and at different crosstie moduli ratios. Similarly to the Hertzian contact analysis conducted in CHAPTER 3, the range of maximum contact pressure is between 800 MPa and 1000 MPa. A similar behavior as the one observed for the contact forces is observed for both the contact pressure and contact area. The period of the sinusoidal contact pressure curve changes with changing crosstie modulus. The peak point of the contact pressure curve at crosstie modulus ratios above 1 (i.e. a transition from low track stiffness to high track stiffness) shifts to the left side of the contact pressure curve at uniform crosstie modulus. This reduces the period of the wheel bouncing. The magnitude of the maximum contact area (i.e.275 mm^2) was not affected by the crosstie modulus ratio variation, as shown in Figure 4-7.

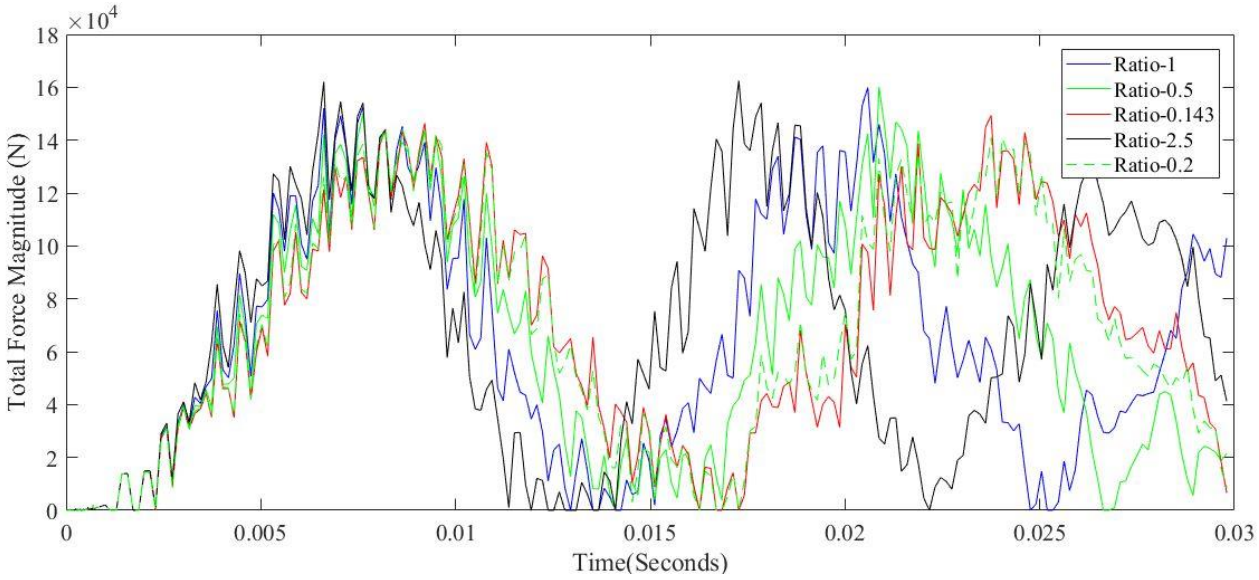

Figure 4-8: A plot of the total force magnitude due to contact pressure and frictional stresses (CFTM) against time.

The magnitude of the forces induced as a result of contact pressure and frictional stresses are plotted against the time increments in the rolling step as shown in Figure 4-8. The maximum magnitude of the summation of contact pressure and fictional forces is almost twice the maximum contact force shown in Figure 4-2. The sinusoidal behavior of the wheel-rail contact forces identified in earlier Figures still holds to the forces plotted in Figure 4-8. Furthermore, it can be seen in Figure 4-8 that a much shorter period occurs at crosstie moduli ratios above 1 relative to the periods observed in contact pressure and force plots. On the other hand the period of the total force magnitude due to contact pressure and frictional stresses is prolonged at crosstie moduli ratios below 1. In addition, the time period at which the summation of contact pressure and frictional forces is zero is more (i.e. $0.0125\ to\ 0.0175$ seconds) at crosstie moduli ratios below 1 relative to crosstie moduli ratios above 1 (i.e. $0.011\ to\ 0.014$ seconds). The track flexibility plays a significant role in the period and frequency of wheel bouncing on the rail which in turn has an influence on the forces acting in the wheel-rail interface.

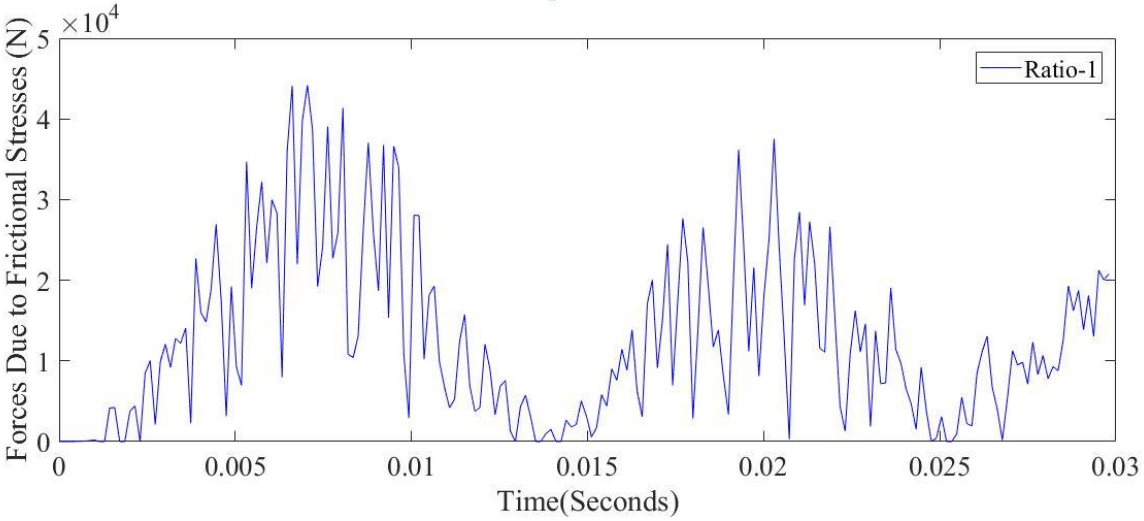
×10^4
Forces Due to Frictional Stresses (N)
Time(Seconds)
Ratio-1
0
1
2
3
4
5
0
0.005
0.01
0.015
0.02
0.025
0.03

(a)

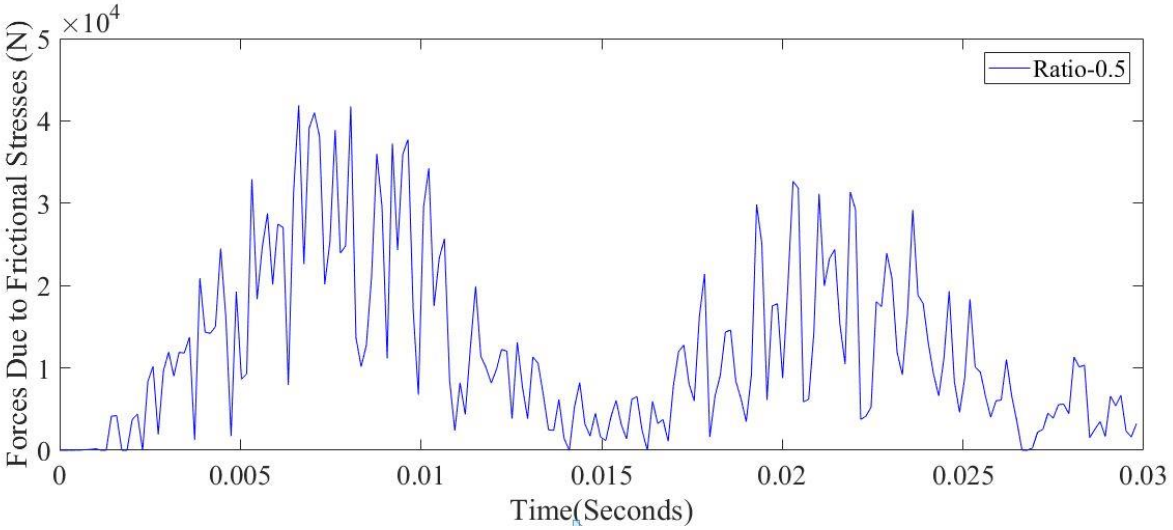
×10^4
Forces Due to Frictional Stresses (N)
Time(Seconds)
Ratio-0.5
0
1
2
3
4
5
0
0.005
0.01
0.015
0.02
0.025
0.03

(b)

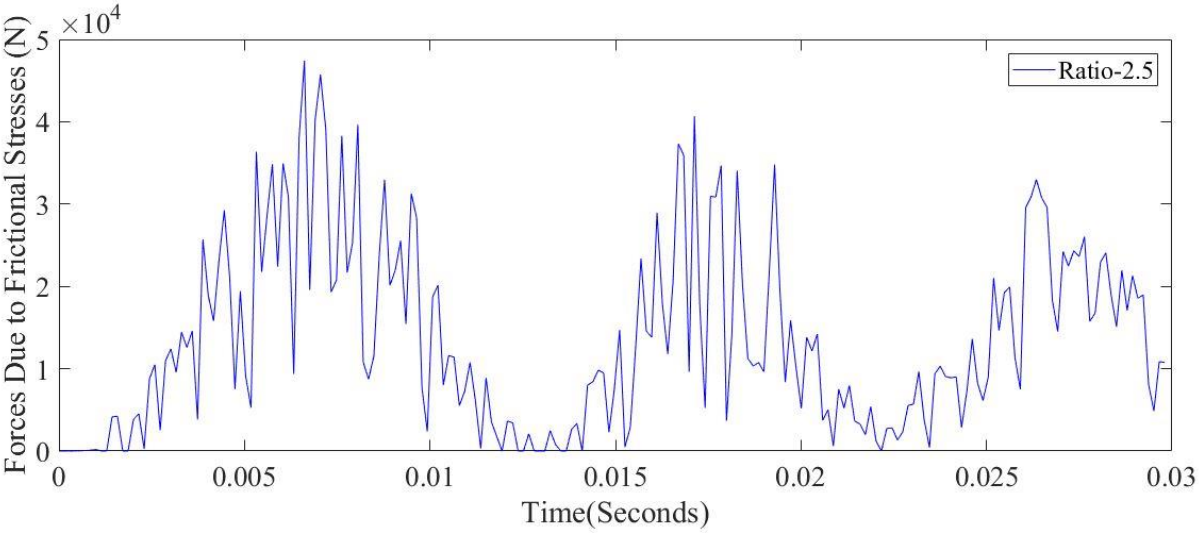
×10^4
Forces Due to Frictional Stresses (N)
Time(Seconds)
Ratio-2.5
0
1
2
3
4
5
0
0.005
0.01
0.015
0.02
0.025
0.03

(c)

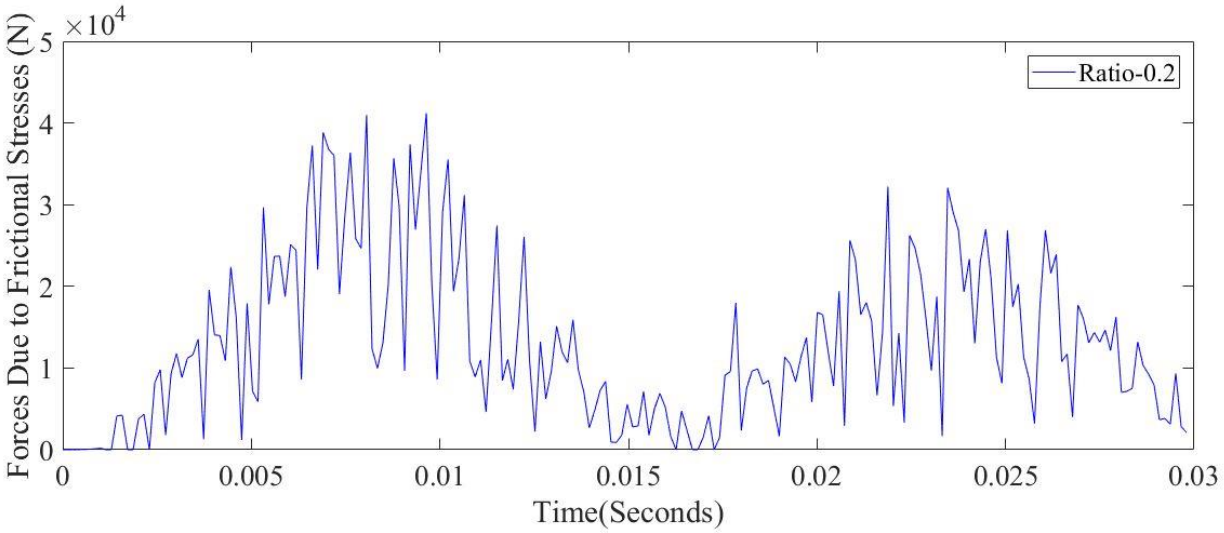

(d)

Figure 4-9: Total force magnitude due to frictional stress at every 0.000 seconds time increment at different crosstie moduli ratios. (a) Crosstie modulus ratio of 1 (b) Crosstie modulus ratio of 0.5 (c) Crosstie modulus ratio of 2.5 (d) crosstie modulus ratio of 0.2.

The frictional stresses have a huge impact on the wear behavior of both wheels and rails, therefore a clearer trend of these forces with varying track stiffness is a necessity. Figure 4-9 (a) to (d) shows plots of forces due to frictional stresses against time at various crosstie modulus ratios. It can be clearly seen that there are more cycles of the friction force curve in the same time period at crosstie modulus ratio of 2.5 relative to the crosstie modulus ratios of $1, 0.5$ and $0{,}143$. Moreover, high friction forces are observed at crosstie modulus ratios of 2.5 and this is due to the high impact factor at transition points from low track stiffness to a high track stiffness section.

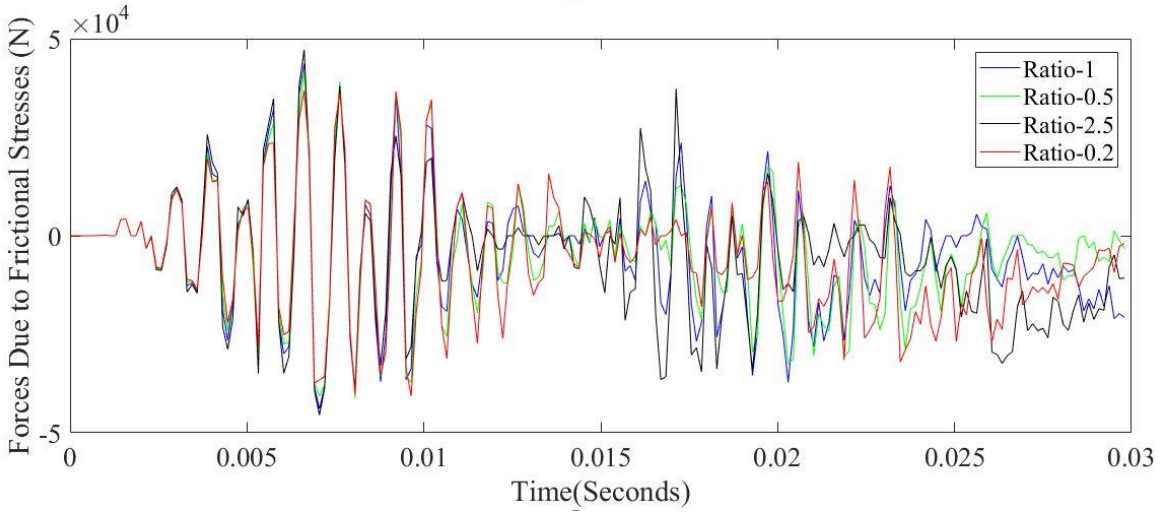

(a)

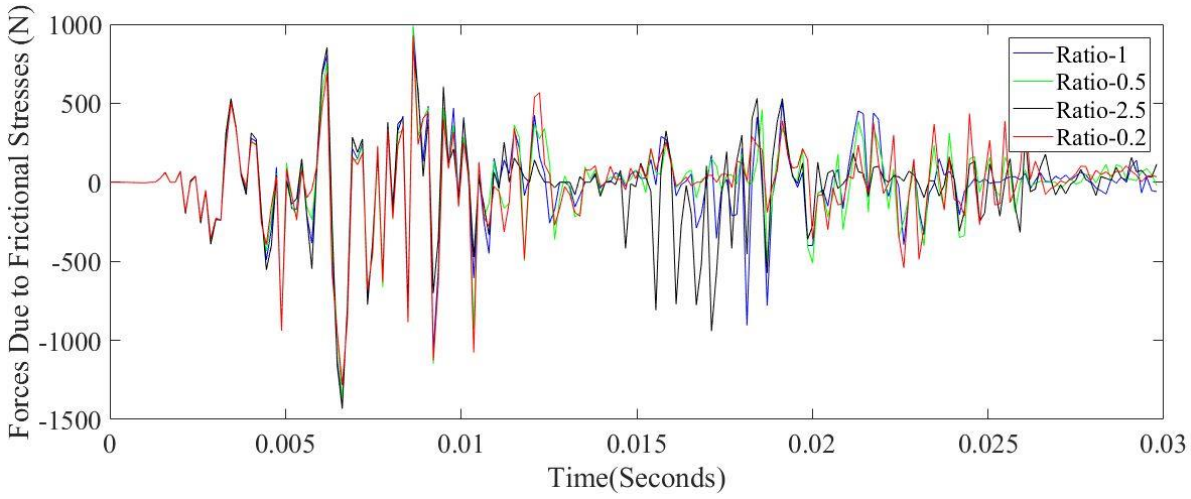

(b)

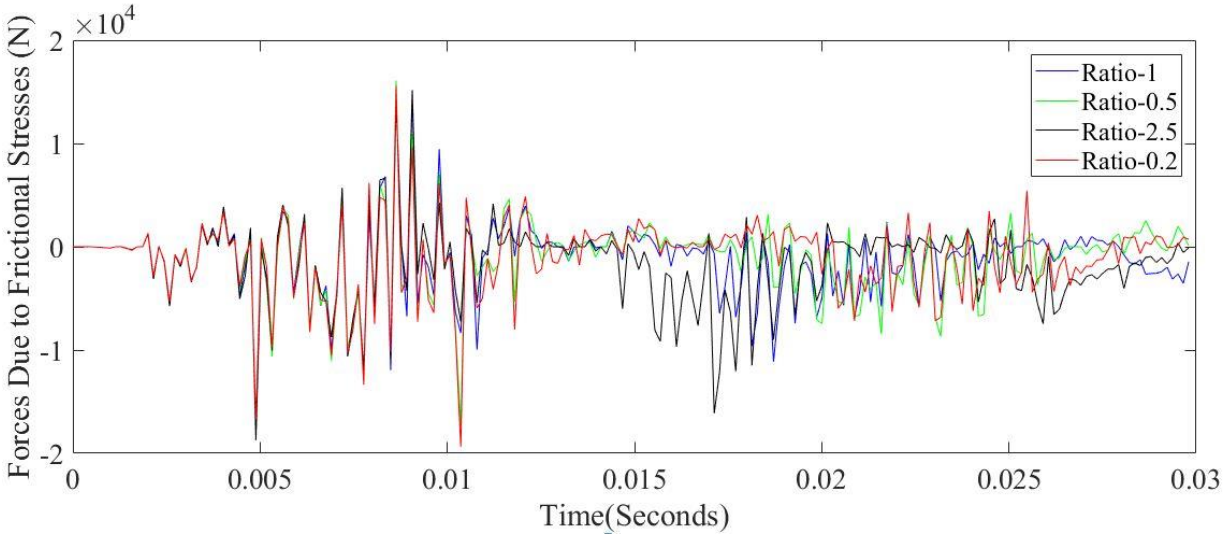

(c)

Figure 4-10: Plots of forces due to frictional stresses against time increments (a) in the x-direction (longitudinal) (b) in the y-direction (vertical) (c) in the z-direction (transvers).

Figure 4-10 (a) to (c) shows the individual components of the frictional force magnitude is the Cartesian coordinate system. Figure 4-10 (b) shows the friction force along the y axis and as it can be seen lower values of fiction force occurs in that direction relative to other directions. Significant frictional forces values are observed along the x and z axis, since friction force occurs at the surfaces in contact in the opposite direction of rolling motion. The lateral motion of the wheel was restricted through boundary condition but still frictional forces in the z direction were observed (see Figure 4-10 (c)). A larger portion of the friction forces is along the x axis since the wheel is moving along this axis (see Figure 4-10 (a)). Throughout the graphs in Figure 4-10, it can be observed that the amplitude of the frictional forces is affected by the variation in crosstie modulus ratio. Larger amplitudes occurs at crosstie ratios of 2.5 and 0.143 relative to a ratio of 1.

4.2 Influence of non-uniform track stiffness on shear contact forces, shear stresses and moments.

The contact moments acting on the wheel-rail interface as well as the shear forces and stresses acting on the wheel tread surface were extracted from the dynamic explicitly FE model and plotted at each time increment and various crosstie modulus ratios. The total magnitude of the contact moments acting on the wheel-rail interface were first plotted followed by the contact moments along each direction in the Cartesian coordinate system. Furthermore the wheel tread shear stresses were plotted at each time increment and comparisons were made between uniform and non-uniform crosstie modulus results.

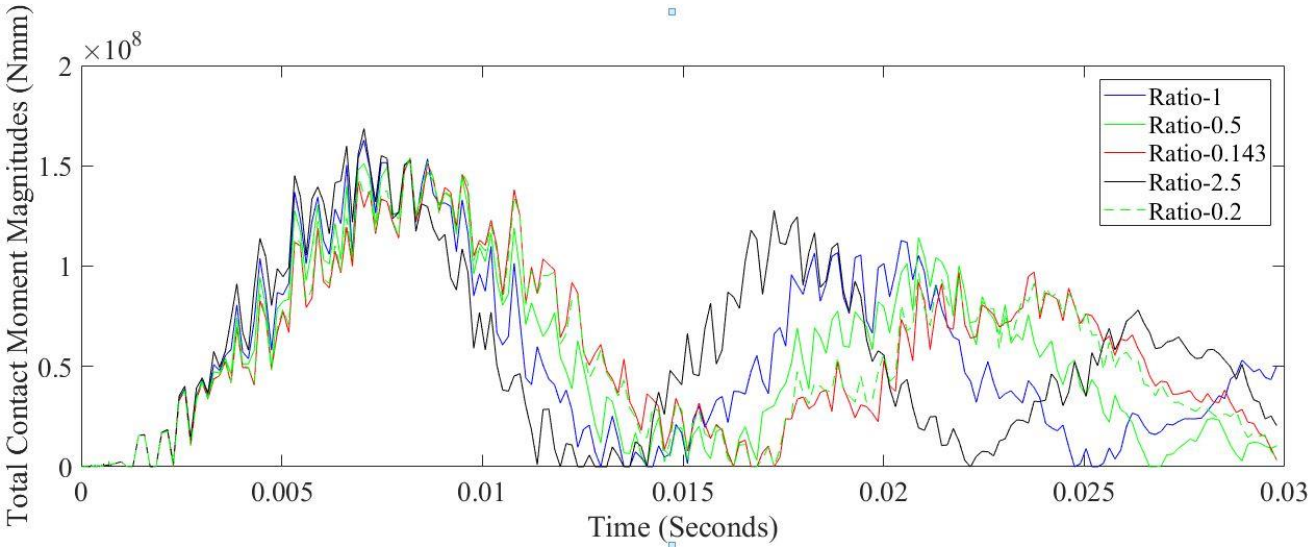

(a)

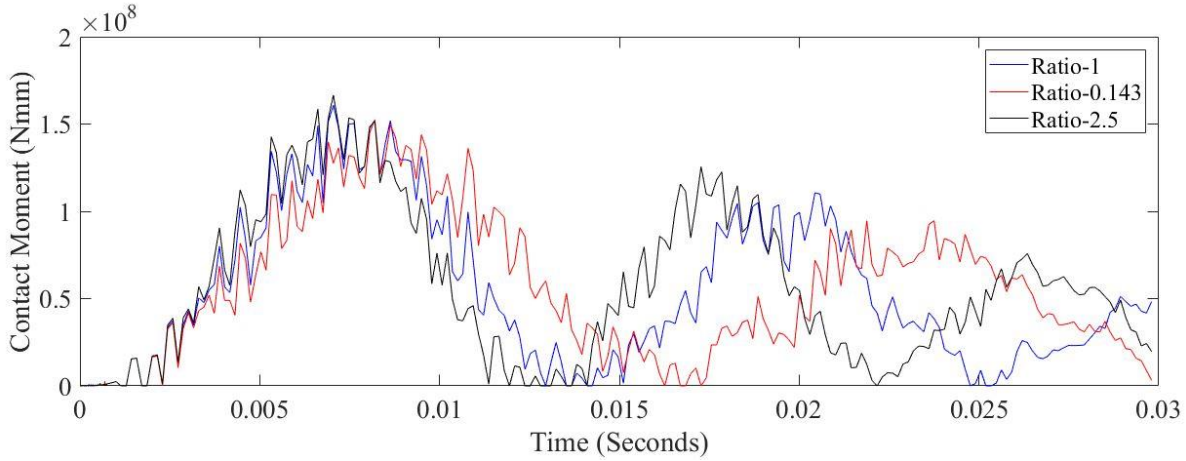

(b)

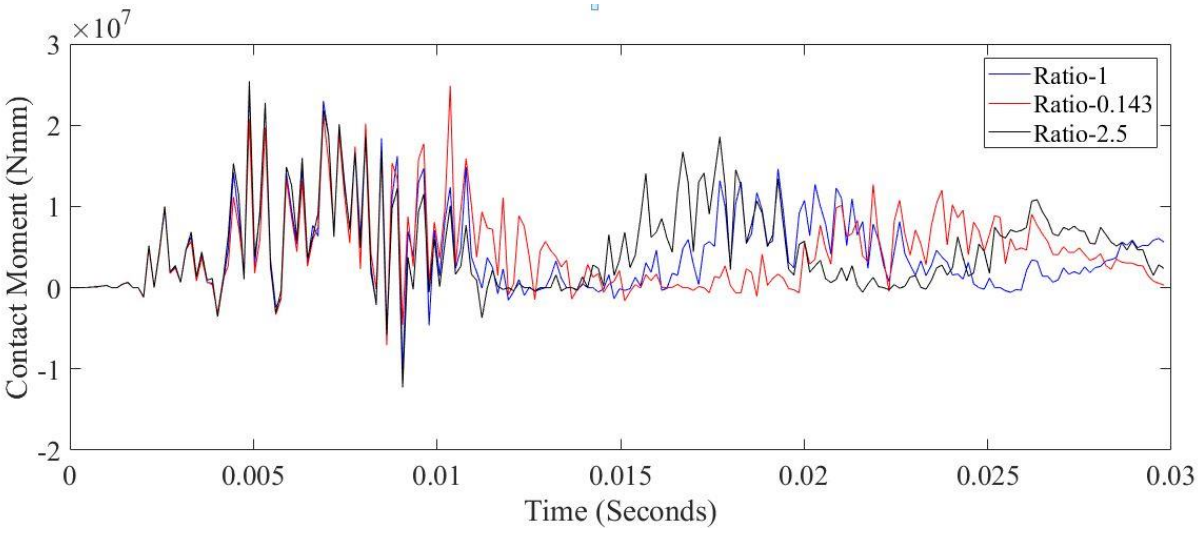

(c)

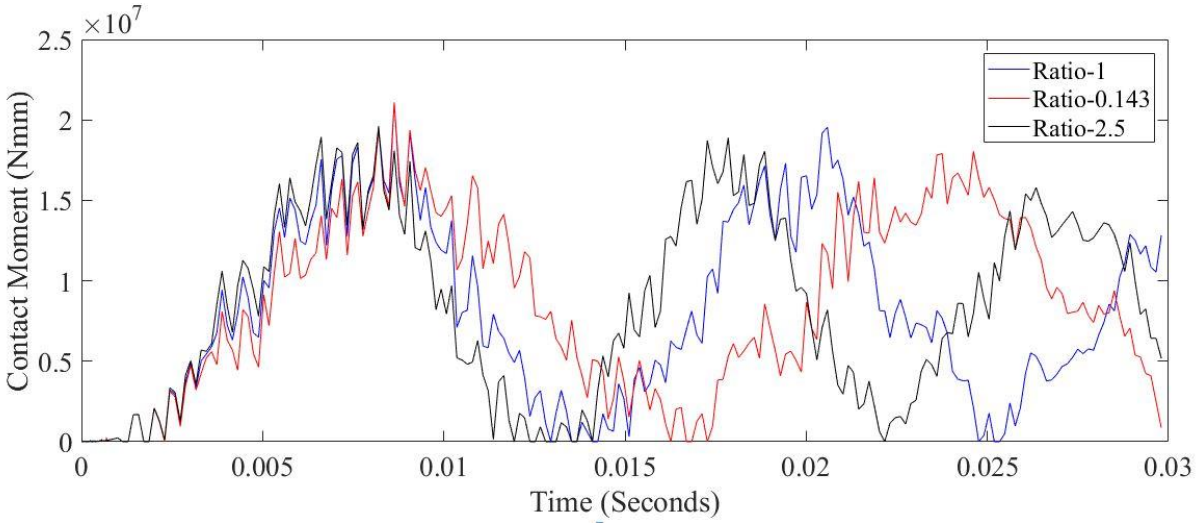

(d)

Figure 4-11: Plots of the contact moments at each time increment. (a) Total contact moment magnitude plot. (b) A plot of contact moments about the z-axis. (c) A plot of contact moments about the y-axis. (d) A plot of contact moments about the x-axis.

The total magnitude of the moments acting in the wheel-rail interface are plotted against the time increments as shown in Figure 4-11 (a) above. The moments about each axis are shown in Figures 4-11 (b) to (d). The maximum magnitude of the contact moment is reducing with rolling time (see Figure 4-11(a)). In the first period of the sinusoidal varying contact moment magnitudes, higher moments are observed at crosstie modulus ratios above 1 relative to those below 1. From Figures 4-11 (b) to (d) it can be seen that higher rotational moments occurs along the z-axis which is along the wheel axis of rotation. Rotations in the x and y-directions still occurs due to the wheel deformation under loading.

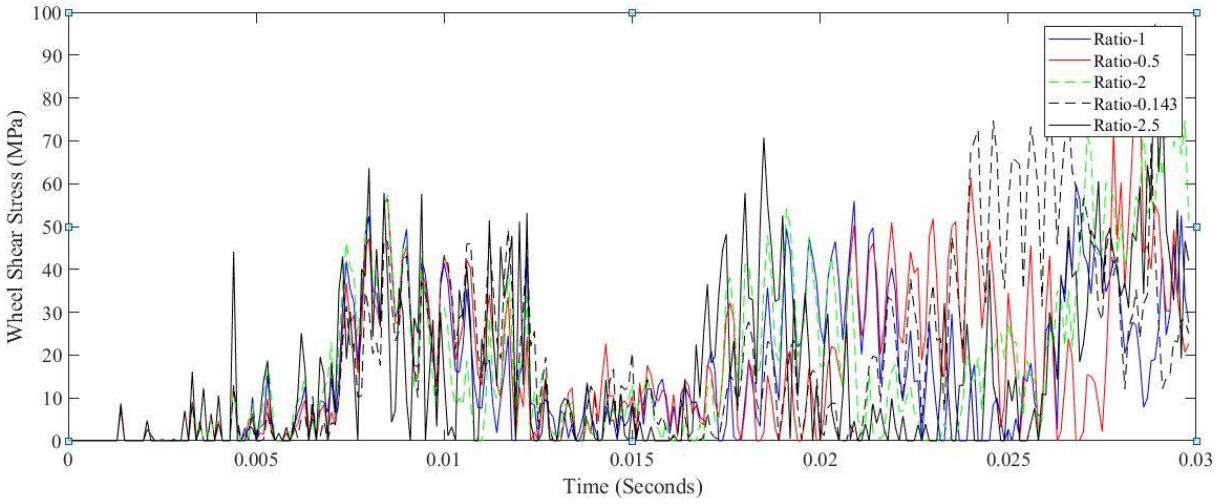

Figure 4-12: Wheel shear stress at varying crosstie modulus ratios

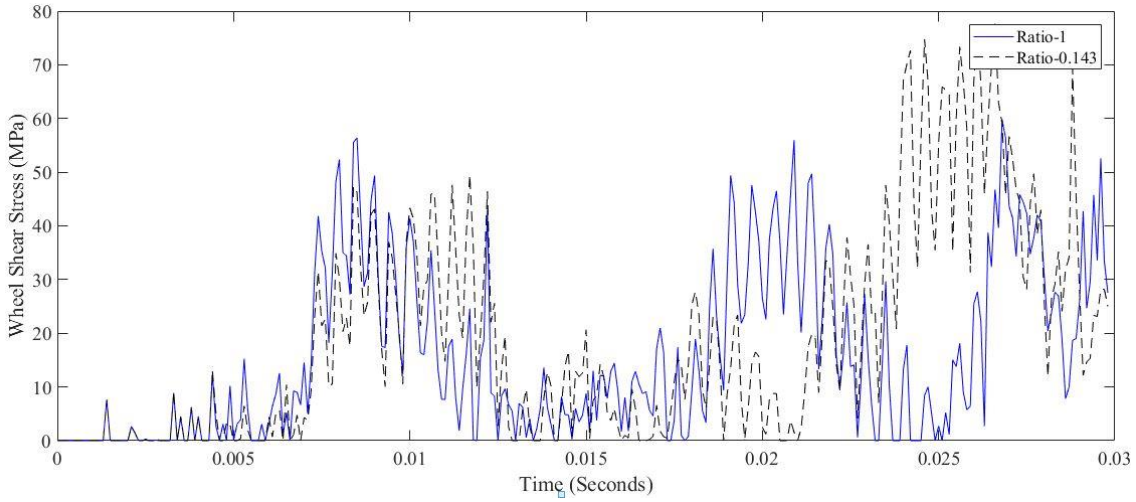

(a)

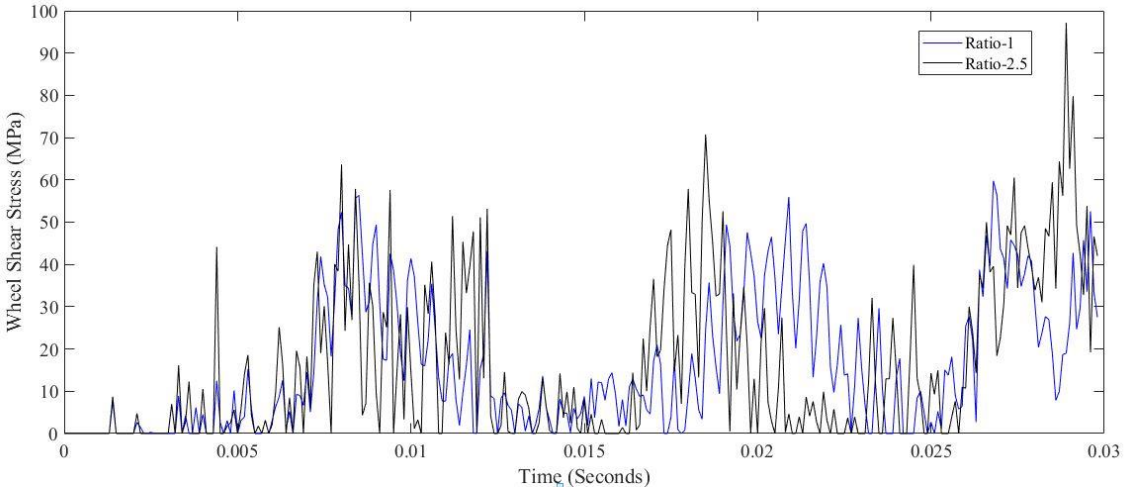

(b)

Figure 4-13: Plots of shear stresses occurring on the wheel tread surface at different crosstie modulus ratio. (a) Ratio-1 and 0.143. (b) Ratio-1 and 2.5.

In Figures 4-12 and 4-13 (a)-(b) the magnitudes of shear stresses acting on the wheel tread surface are plotted against the time increments in the rolling step. For better trend visualization the shear stresses at varying crosstie modulus ratio, selected crosstie moduli ratios are plotted in Figure 4-13 (a) and (b). It can be seen from Figures 4-13 (a) and (b) that the shear stresses acting on the wheel tread surfaces increases at varying crosstie modulus ratio relative to uniform crosstie modulus. Higher wheel tread shear stresses are observed at the transition from a low stiffness track to a high stiffness track (i.e. 100 MPa), see Figure 4-13 (b), while at the transition from a high stiffness track to a low stiffness track a maximum wheel tread shear stress of 80 MPa is observed, see Figure 4-13 (a). At uniform crosstie modulus where the crosstie ratio is 1 the maximum observed wheel tread shear stress was 60 MPa, see Figure 4-12.

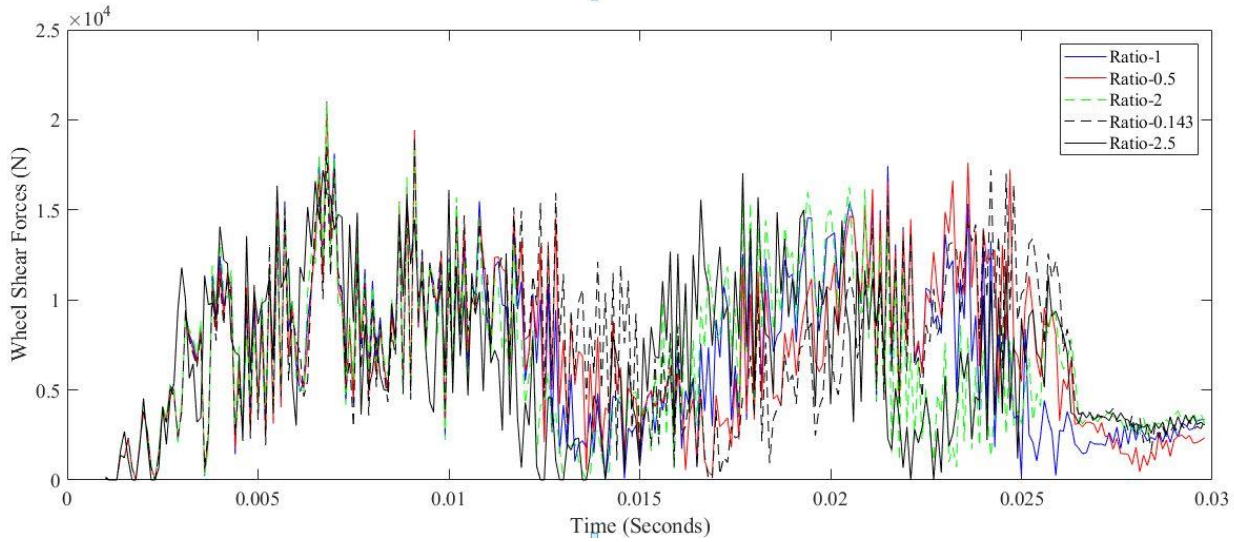

(a)

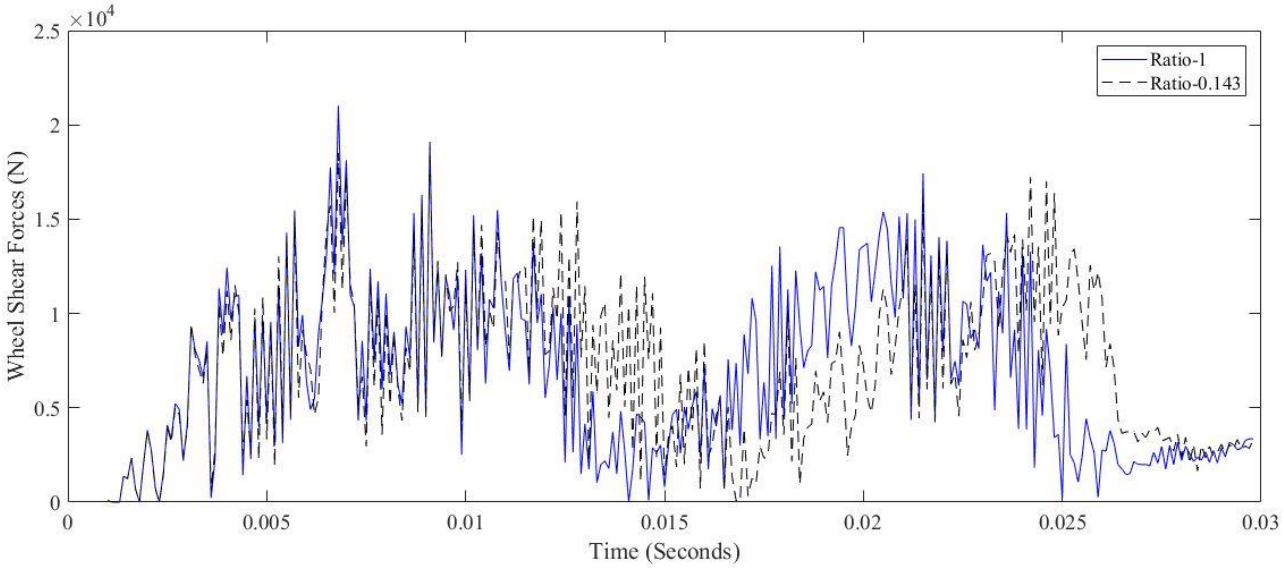

(b)

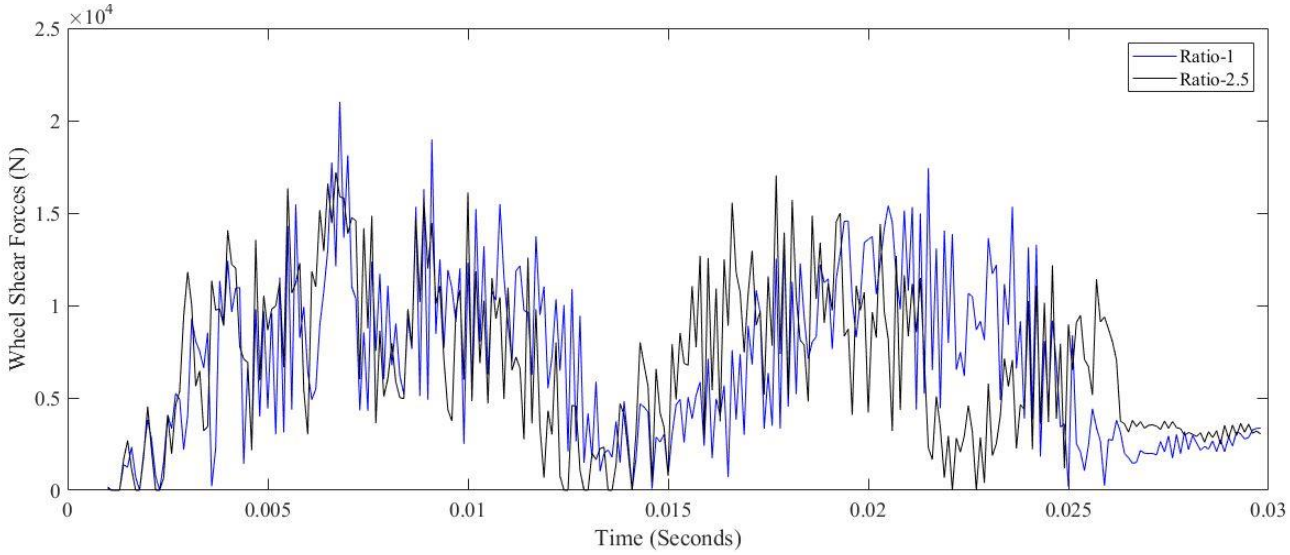

(c)

Figure 4-14: Plots of wheel shear force at varying crosstie modulus ratio. (a) Plots at various crosstie moduli ratios (b) Plots for crosstie modulus ratio-1 and 0.143 (c) Plots for crosstie modulus ratio-1 and 2.5.

The shear forces acting on the wheel tread surface were extracted from ABAQUS odb file using Scripting with python programming language. The extracted results are plotted as shown in Figures 4-14 (a) to (c). High shear forces on the wheel tread at uniform crosstie modulus are observed relative to varying crossti modulus. This implies that more tractive effort can be transmitted into the wheel-rail interface at uniform crosstie modulus than at varying crosstie modulus. Figure 4-13 showed that there is a high shear stress at varying crosstie modulus relative to uniform crosstie modulus. Based on these results it can be said that the wheel contact area at a paticular point in the rolling time is low at varying crosstie modulus relative to uniform crosstie modulus. In addition a shorter period of the shear force curve is observed at crosstie modulus ratios above 1 releative to those below 1. This means that multiple peaks in the shear force at crosstie modulus ratio above 1 occurs in the same time interval than those occuring at uniform crosstie modulus (i.e.Crosstie modulus ratio-1). The periods at crosstie modulus ratios below 1 are prolonge d due to the high flexibility (i.e. more deformation) of the track at lower track stiffnesses. The time at which the wheel is in contact with the rail is more at crosstie modulus ratios below 1 relative to uniform crosstie modulus.

4.3 Influence of track stiffness on wheel-rail slip parameters (i.e. slip velocity)

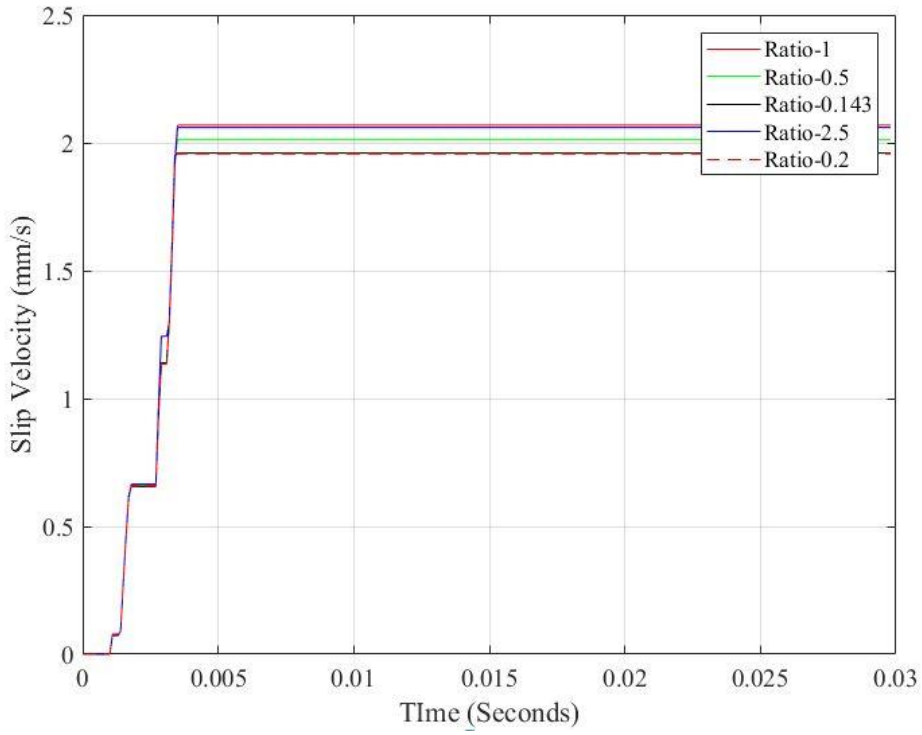

Figure 4-15: Slip velocity plot at different crosstie modulus ratios

Figure 4-15 shows a plots of the slip velocity against time at different crosstie modulus ratios. For each modulus ratio it took the model less than 5 milliseconds to reach a constant value. After 5 milliseconds the slip velocity remained constant throughout the rolling step. The slip velocity reduces at varying crosstie modulus ratio both at ratios below and above 1.

4.4 Track stiffness variation influence on wheel tread wear rate

Two critical parameters are required when calculating the volume of material removal on a railway vehicle wheel tread using Archard's equation. Firstly the wear coefficient 'K' and then the magnitude of the slip distance's'. Usually the wear coefficient, K is determined through experiments and field studies, which are very expensive and time consuming. The determination of the wear coefficient in this study is based on a wear map developed by researchers at the Royal Institute of Technology (KTH), Sweden based in an experimental study [61] (i.e. Disk-on-disk tests at University of Magdeburg, Pin-on-disk tests at KTH and Several published disk-on-disk tests). In his research Jendel calibrated the wear coefficient with the slip velocity and the contact pressure as shown in Figure 4-16. The chart was derived only for dry wheel-rail contact condition which are the same conditions used in this study.

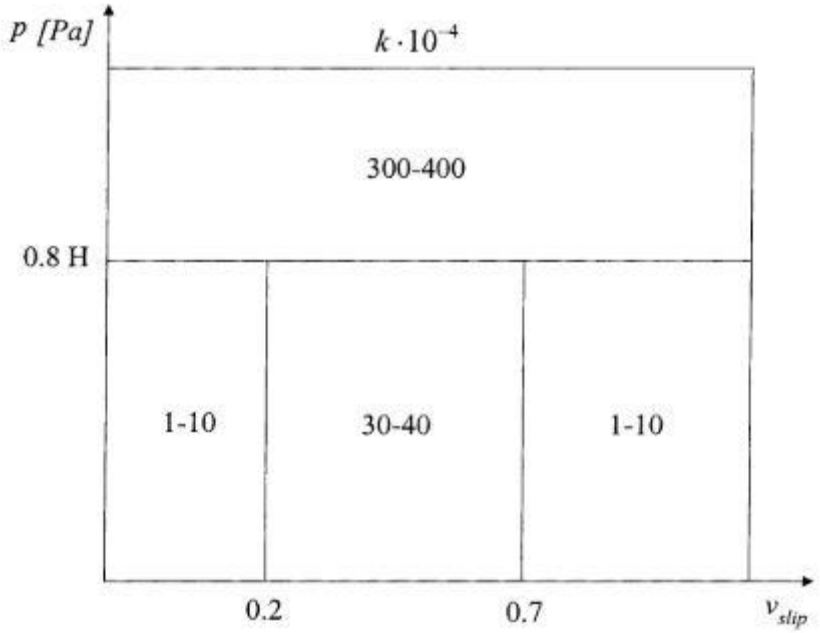

Figure 4-16: Wear chart for the wear coefficient, K based on laboratory measurements with wheel and rail steels(Taken from T. Jendel [61])

The slip distance at each time increment in this study is going to be calculated from Eq. 4-1 which can be written as,

$$\underline{S_i} = \left|\bar{v}_{slip,i}\right|.\Delta t \qquad \text{Eq. 4-1}$$

where,

$\Delta t = 0.0001\text{mm}$ is the time increment,

$\bar{v}_{slip}$ is the slip velocity at each time increment, i.

The wheel material Hardness to be used in the Archard's wear model is,

$$H = 300\ \text{N/mm}^2$$

The contact pressure results from the dynamic model are in the range of $400 - 1000$ MPa and the slip velocity is in the range of 0 to 0.2 m/s. Using this information the values of K, the Archard wear coefficient, can be extracted from the chart illustrated in Figure 4-16. The value of K is taken as the average value in the bottom left corner region of the chart, i.e. $K = 5 \times 10^{-4}$.

Therefore, we approximate the total wear volume during the run period of the FEM as:

$$\underline{V_W} = \frac{K}{H}\sum_{i=0}^{N} S_i\,.\,N_i, \qquad \text{Eq. 4-2}$$

where

$\underline{V_W}$ is the volume of material removed on the wheel tread through a rolling distance of 800 mm,

N is the number of time steps,

S_i is the slip distance at each time increment and,

N_i is the normal contact force at each time increment.

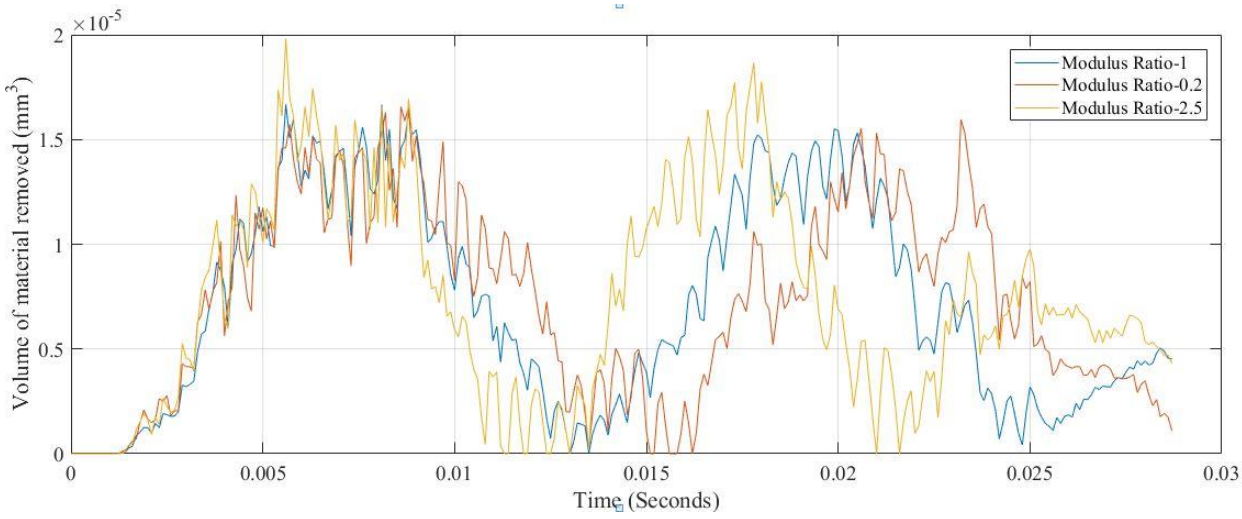

(a)

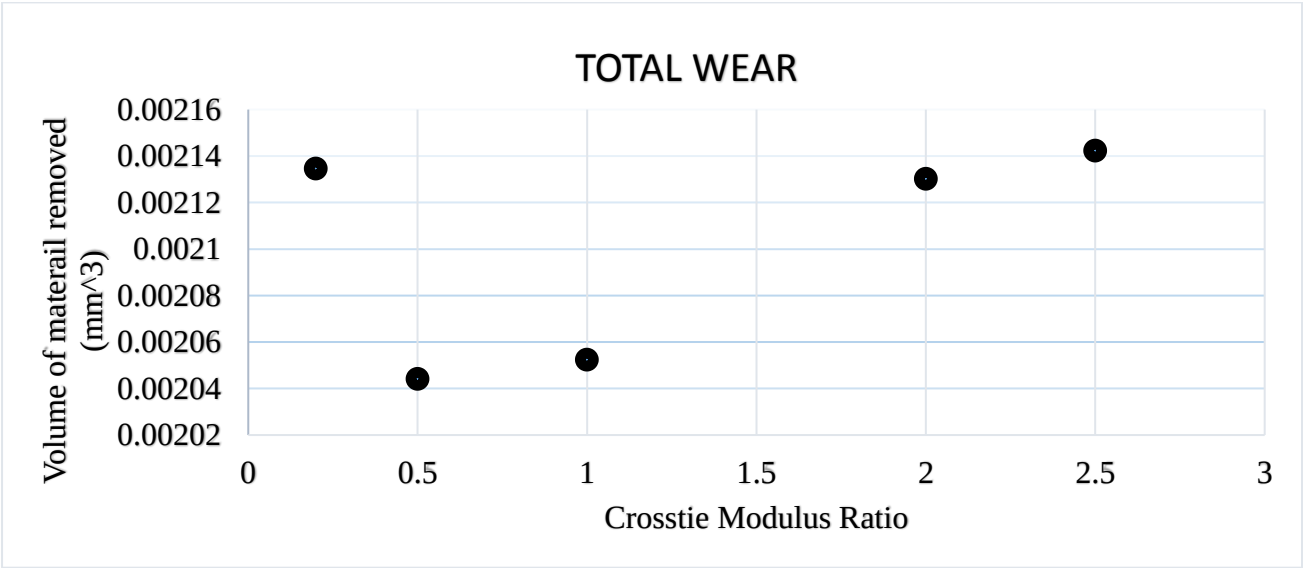

(b)

Figure 4-17: Plot of wear volume at different crosstie modulus ratios (a) Plots of the volume of material removal at each time increment. (b) Plots of total volume of material removed on the wheel tread surface due to wear at different modulus ratios.

It can be clearly seen from Figure 4-17 that the total volume of material removed on the wheel tread after a rolling distance of 800 mm is high at varying crosstie modulus ratio relative to uniform crosstie

modulus. The track stiffness variation at a transition from soft to hard track has a huge impact on the wear volume of railway vehicle wheel as compared to a transition from hard to soft track. A much lower volume of material removal was observed at uniform crosstie modulus.

4.5 Discussion of results

Chapter 4 presented the results of this research and a brief discussion of them. It was shown in Section 4.1 that in a time period of 0.0288 seconds and a railway vehicle wheel translational distance of 800 mm the contact forces acting in the wheel-rail contact area are behaving in a sinusoidal manner. At varying crosstie modulus ratio in a FEA model (i.e. non-uniform track stiffness) the period of the contact forces plot against time increments, also varied. Crosstie modulus ratios above 1 were defined as a track transition from a low stiffness region to a high stiffness one while at crosstie modulus ratios below 1 it is vice versa. The period of the contact forces and stresses became shorter at crosstie modulus ratios above 1. In the same time interval the contact forces had more cycles at varying crosstie ratios (i.e. crosstie modulus ratio above 1) relative to uniform crosstie modulus. In addition the impact factor was calculated as the quotient of wheel-rail contact dynamic forces and static forces. A high impact factor was observed at crosstie modulus ratios above 1. At crosstie modulus ratio below 1 the period of the contact forces and stresses plots at each time increment increased relative to uniform crosstie modulus (i.e. crosstie modulus ratio of 1). This is mainly due to the track flexibility at transition point from high track stiffness to lower track stiffness regions. High allowed track deformations at lower track stiffness values allows for longer time periods at which the wheel is in contact with the rail. The railway track stiffness variation influences the wheel-rail contact forces and stresses as outlined above. The forces due to frictional stresses were also plotted at each time increment in the sections presented in Chapter 4. High frictional forces were observed at varying crosstie modulus relative to uniform crosstie modulus. This was in line with the observations made on the shearing forces and stresses acting in the contact area. High shear stresses were observed at varying track stiffness relative to uniform track stiffness. On the other hand the shear forces were almost the same at both varying and uniform track stiffness but with different time periods. This implies that at a particular point in time in the rolling step the contact area is usually lower at varying track stiffness than at constant track stiffness.

The last section of the results chapter introduced the wheel tread wear. The Archard's wear equation was used to estimate the volume of material removal on the wheel tread surface. The Archard's wear equation has been calibrated by several researcher for use on the wear modelling of wheel-rail contacts. The value of the wear coefficient used in this study was taken from a wear map chart previously

developed by Jendel. The wear calculations showed that the variability of railway track modulus has an influence of the volume of material removed on the wheel tread surface by wear. High wear volumes were observed both at crosstie modulus ratios above and below 1 relative to uniform crosstie modulus. Higher wear volumes were recorded at the transitions from low track modulus to high track modulus (i.e. crosstie modulus ratio above 1). Minimizing the variation in track modulus can indeed reduce the wear of railway vehicle wheels.

5 CONCLUSIONS AND FUTURE WORK

5.1 Conclusions

The study of the factors that influences the wear phenomena occurring on both railway vehicle wheels and railway tracks is of crucial importance in maintenance schedule optimization and maintenance planning. Various researches (i.e. [61], [62], [7], [63], [64], [65]) have been done on the different factors that influences the trend of wheel and rail profile evolution due to wear. Different maintenance schedule optimization models have been developed. In this thesis research, the author tries to incorporate the spatial track stiffness variation into wear prediction models. The influence of track stiffness variation on wheel-rail contact parameters was first investigated followed by the calculation of the volume of material removed from the wheel tread at different degrees of non-uniformity of track modulus.

A Finite Element Model (FEM) of a single railway vehicle wheel rolling in the rail, supported by three crossties was modelled in ABAQUS simulation software environment. The geometry of the wheel and the rail were taken with reference to the vehicle parameters of Addis Ababa Light Rail Transit System (AALRTS). The FE model was validated using closed form rolling contact analytical solutions. The equivalent track stiffness of the railway track support structure was calibrated to match the actual rail track web strains occurring in real operation. The track stiffness variation in the FE model was achieved by varying the crosstie modulus of elasticity ratio between the middle crosstie and the side crossties.

It was observed that the track stiffness spatial variation has an influence on the contact characteristics of wheel-rail physical quantities. The contact stresses and forces were observed to vary in a sinusoidal manner along the rolling distance. At non-uniform track modulus the time periods of the sinusoidal curves of contact forces and stresses were observed to be varying. At a transition from a soft track to a hard track (i.e. crosstie modulus ratio above 1) the time periods were shortened and more cycles occurred in the same time interval relative to uniform track modulus and transition from hard track to soft track. On the other hand the time periods were prolonged for transitions from a hard track to a soft track (i.e. crosstie modulus ratio below 1) relative to uniform track modulus and transitions from soft to hard tracks. This is because at low track stiffness there is more allowable track deformations relative to stiff tracks. Due to the more allowable track deformations at lower track stiffness the time periods

at which the wheel is in contact with the rail are prolonged. Impact factors were also plotted at each time increment, it was shown that large impact factors occur at non-uniform track modulus relative to uniform track modulus. In addition the fundamental frequencies of the contact forces were plotted. Higher fundamental frequencies at transitions from high track stiffness to lower track stiffness region (i.e. crosstie modulus ratio below 1) were observed. From these observations it can be concluded that a stiff track structure can increased the wheel bouncing on the rail which results in high impact factors. In addition it can be said that transition from soft to hard track stiffness regions result in higher impact factors relative to transition from hard to soft track stiffness, but impact factors in these both scenarios are more as compared to uniform track modulus conditions.

Non-uniform track modulus results in high forces due to contact pressure and frictional stresses in the contact interface. More frictional stresses were observed along the rolling direction and their magnitude varied with variation in crosstie modulus ratios. High friction forces occurred at non-uniform relative to uniform crosstie modulus. Furthermore, high contact moments were observed about the z-axis which is parallel to the wheel axle in the FE model. The contact moments were affected by the variation in crosstie modulus ratio. There was an increase in contact moment magnitudes at transition points from soft to hard track regions, while there was a decrease in contact moments magnitudes at transitions from hard to soft track regions. This implies that the tractive effort transmitted into the contact area is affected by the non-uniformity of the track modulus. This point is also supported by the high shear stresses which were observed to be acting on the wheel tread surface at non-uniform track modulus.

A large influence of the track stiffness variation was found to be at transition points from low track stiffness regions to high track stiffness ones, since a large volume of material removed by wear was found at this condition. Higher wear volumes were still observed at transitions from hard track to soft track modulus regions relative to uniform track modulus conditions.

The variability of the track modulus is inevitable on railway tracks, therefore it should be included in wear models so as to improve the accuracy of wear trends prediction. In addition the degree of variability of the track modulus should be reduced at the construction stage by uniform compaction of the track elements and varying rail pads stiffness at different locations to create a uniform global track stiffness.

5.2 Recommendations

It is recommended that the railway track stiffness variation be evaluated in the railway industries and be included in wear prediction models. Maintenance planning and maintenance schedule optimization

tools currently used by railway industries will be improved because wear prediction accuracy would have been improved.

5.3 Future work

Future work will consider the influence of temperature on the wear of both wheels and rails at varying track modulus. The influence of track structure components material damping on the spatial variation of the railway track stiffness will be an area of future research interest. Moreover, the effects of track flexibility on the wear evolution of the wheel tread will be part of future researches.

6 REFERENCES

[1] J. C. Arndt *et al., Transportation, Social and Economic Impacts of Light and Commuter Rail*, vol. 7, no. 19. Texas: Texas Transportation Institute The Texas A&M University System College Station, 2009.

[2] C. Al, *Microstructure and wear of materials*, Series 10. Amsterdam: Elsevier Science Publishers, 1987.

[3] W. Hui, Z. Xu, Y. Zhang, X. Zhao, C. Shao, and Y. Weng, "Hydrogen embrittlement behavior of high strength rail steels : A comparison between pearlitic and bainitic microstructures," *Mater. Sci. Eng. A*, vol. 704, pp. 199–206, 2017.

[4] P. Clayton, "Tribological aspects of wheel-rail contact: a review of recent experimental research," *Wear*, vol. 191, pp. 170–183, 1996.

[5] W. J. Wang, R. Lewis, B. Yang, L. C. Guo, Q. Y. Liu, and M. H. Zhu, "Wear and damage transitions of wheel and rail materials under various contact conditions," *Wear*, vol. 362–363, pp. 146–152, 2016.

[6] A. A. Shabana, R. Chamorro, and C. Rathod, "A multi-body system approach for finite-element modelling of rail flexibility in railroad vehicle applications," *Proc. Inst. Mech. Eng. Part K J. Multi-body Dyn.*, vol. 222, no. 1, pp. 1–15, 2008.

[7] J. F. Aceituno, P. Wang, L. Wang, and A. A. Shabana, "Influence of rail flexibility in a wheel/rail wear prediction model," *Proc. Inst. Mech. Eng. Part F J. Rail Rapid Transit*, vol. 231, no. 1, pp. 57–74, 2017.

[8] L. Puzavac, Z. Popović, and L. Lazarević, "Influence of Track Stiffness on Track Behaviour under Vertical Load," *PROMET - Traffic&Transportation*, vol. 24, no. 5, pp. 405–412, 2012.

[9] J. Evans and M. Berg, "Challenges in simulation of rail vehicle dynamics," *Veh. Syst. Dyn. Int. J. Veh. Mech. Mobil.*, vol. 47, no. 8, pp. 1023–1048, 2009.

[10] T. A. P. and M. P. M.J. Neale, Ed., *Wear– Materilas, Mechanisms and Practice*. West Sussex, England: John Wiley & Sons Ltd, 2005.

[11] K. Mädler and M. Bannasch, "Materials used for Wheels on Rolling Stock, Deutsche Bahn AG, Technical Centre, Brandenburg-Kirchmöser, GERMANY," 2007.

[12] R. Lewis, P. Christoforou, W. J. Wang, A. Beagles, M. Burstow, and S. R. Lewis, "Investigation of the in fluence of rail hardness on the wear of rail and wheel materials under dry conditions (

ICRI wear mapping project),” *Wear*, vol. 430–431, pp. 383–392, 2019.

[13] C. Kennedy, E. Miller, A. Shalaby, J. Coleman, and M. Heather, “The Four Pillars of Sustainable Urban Transportation,” *Transp. Rev. A Transnatl. Transdiscipl. J.*, vol. 25, no. 4, pp. 393–414, 2005.

[14] B. R. Lunden, Chalmersi Charmec, B. Paullsson, *Wheel-rail interface handbook*. Sweden: Wood head Publishing Limited, 2009.

[15] P. Pointner, “High strength rail steels — The importance of material properties in contact mechanics problems,” *Wear*, vol. 265, pp. 1373–1379, 2008.

[16] *J.Z. Lu, J. Cao, H.F. Lu, et al., Wear properties and microstructural analyses of Fe-based coatings with various WC contents on H13 die steel by laser cladding, Surface & Coatings Technology, https://doi.org/10.1016/ j.surfcoat.2019.04.063*. .

[17] K. H. J. Buschow, R. W. Cahn, M. C. Flemings, B. Ilschner, E. J.Kramer, and S. Mahajan, “Encyclopedia of materials,” *Sci. Technol.*, vol. 4, pp. 3565–3575, 2001.

[18] J. H. Beynon and A. J. Perez-unzueta, “Microstructure and wear resistance of pearlitic rail steels,” *Wear*, vol. 164, pp. 173–182, 1993.

[19] J. Debehets *et al.*, “Analysis of the variation in nanohardness of pearlitic steel : Influence of the interplay between ferrite crystal orientation and cementite morphology,” *Mater. Sci. Eng. A*, vol. 616, pp. 99–106, 2014.

[20] B. Sladojević, M. Jelić, and M. Puzić, “New requirements for the quality of steel rails,” *Assoc. Metall. Eng. Serbia AMES*, vol. 17, no. 4, pp. 213–219, 2010.

[21] Z. Gronostajski, Z. Pater, L. Madej, A. Gontarz, and L. Lisiecki, “Recent development trends in metal forming,” *Arch. Civ. Mech. Eng.*, vol. 19, pp. 898 – 941, 2019.

[22] K. Wang and R. Pilon, *Investigation Of Heat Treating Of Railroad Wheels And Its Effect On Braking Using Finite Element Analysis :Griffin Wheel Company*. .

[23] V. Kazymyrovych, J. Bergström, and F. Thuvander, “Local stresses and material damping in very high cycle fatigue,” *Int. J. Fatigue*, vol. 32, no. 10, pp. 1669–1674, 2010.

[24] M. S. Sichani, “Wheel-Rail Contact Modelling in Vehicle Dynamics Simulation,” KTH Royal Institute of Technology, 2013.

[25] H. Ghaednia, X. Wang, S. Saha, Y. Xu, A. Sharma, and R. L. Jackson, “A Review of Elastic-Plastic Contact Mechanics A Review of Elastic-Plastic Contact Mechanics,” *Appl. Mech. Rev.*, vol. 69, no. April, 2018.

[26] K. L. Johnson, *Contact mechanics*. Cambridge: Published by the Press Syndicate of the University of Cambridge, 1985.

[27] M. A. Arslan and O. Kayabasi, “Advances in Engineering Software 3-D Rail – Wheel contact analysis using FEA,” *Eng. Softw.*, vol. 45, pp. 325–331, 2012.

[28] X. Zhao and Z. Li, “The solution of frictional wheel-rail rolling contact with a 3D transient finite element model: Validation and error analysis,” *Wear*, vol. 271, no. 1–2, pp. 444–452, 2011.

[29] X. Zhao and Z. Li, “A solution of transient rolling contact with velocity dependent friction by the explicit finite element method,” *Eng. Comput. Int. J. Comput. Aided Eng. Softw.*, vol. 33, no. 4, pp. 1033–1050, 2016.

[30] E. T. Selig and D. Li, “Track modulus: its meaning and factors influencing it,” *Transp. Res. Rec.*, vol. 1, no. 1470, pp. 47–54, 1994.

[31] T. X. Wu and D. J. Thompson, “The effects of track non-linearity on wheel / rail impact,” *Proc. Inst. Mech. Eng. , Part F J. Rail Rapid Transit*, vol. 218, no. F, pp. 1–15, 2004.

[32] Ê. Fenander, “Frequency dependent stiffness and damping of railpads,” *Proc. Inst. Mech. Eng.*, vol. 211, no. F, pp. 51–62, 1997.

[33] T. Dahlberg, “Railway track stiffness variations - consequences and countermeasures,” *Int. J. Civ. Eng.*, vol. 8, no. 1, pp. 1–12, 2010.

[34] I. Grossoni, A. R. Andrade, Y. Bezin, and S. Neves, “The role of track stiffness and its spatial variability on long-term track quality deterioration,” *Proc. Inst. Mech. Eng. Part F J. Rail Rapid Transit*, vol. 233, no. 1, pp. 1–17, 2018.

[35] E. Tutumluer, T. D. Stark, D. Mishra, and J. P. Hyslip, “Investigation and mitigation of differential movement at railway transitions for us high speed passenger rail and joint passenger/freight corridors,” *2012 Jt. Rail Conf. JRC 2012*, no. April, pp. 75–84, 2012.

[36] L. Ferreira and M. H. Murray, “Transport Reviews : A Transnational Modelling rail track deterioration and maintenance : current practices and future needs Modelling rail track deterioration and maintenance : current,” *Transp. Rev. A Transnatl. Transdiscipl. J.*, vol. 17:3, no. April 2013, pp. 207–221, 1997.

[37] E. Kabo, J. C. O. Nielsen, and A. Ekberg, “Prediction of dynamic train-track interaction and subsequent material deterioration in the presence of insulated rail joints,” *Veh. Syst. Dyn.*, vol. 44, no. SUPPL. 1, pp. 718–729, 2006.

[38] E. G. Berggren, A. M. Kaynia, and B. Dehlbom, “Identification of substructure properties of railway tracks by dynamic stiffness measurements and simulations,” *J. Sound Vib.*, vol. 329, no. 19, pp. 3999–4016, 2010.

[39] J. A. Priest and W. Powrie, “Determination of dynamic track modulus from measurement of

track velocity during train passage," *J. Geotech. Geoenvironmental Eng.*, vol. 135, no. 11, pp. 1732–1740, 2009.

[40] A. Lundqvist and T. Dahlberg, "Load impact on railway track due to unsupported sleepers," *Proc. Inst. Mech. Eng. Part F J. Rail Rapid Transit*, vol. 219, no. 2, pp. 67–77, 2005.

[41] P. Connor, "Track Basics," *Railw. Tech. Website*, no. 2, pp. 1–13, 2017.

[42] A. Andersson, H. Berglund, J. Blomberg, and O. Yman, "The influence of stiffness variations in railway tracks," 2013.

[43] E. Tutumluer, T. D. Stark, D. Mishra, and J. P. Hyslip, "Investigation and mitigation of differential movement at railway transitions for US high speed passenger rail and joint passenger/freight corridors," in *2012 Joint Rail Conference, JRC 2012*, 2012, no. July 2015, pp. 75–84.

[44] B. Liu, "Study of rail vehicle dynamics and wheel-rail contact using full-scale roller rigs.," 2016.

[45] J. F. Archard, "Contact and rubbing of flat surfaces," *J. Appl. Phys.*, vol. 24, no. 8, pp. 981–988, 1953.

[46] A. Zmitrowicz, "Wear patterns and laws of wear - A review," *J. Theor. Appl. Mech.*, vol. Vol. 44 nr, no. 1803, pp. 219–253, 2006.

[47] T. G. Pearce and N. D. Sherratt, "Prediction of wheel profile wear," *Wear*, vol. 144, no. 1–2, pp. 343–351, 1991.

[48] I. Zobory, "Prediction of Wheel/Rail Profile Wear," *Veh. Syst. Dyn. Int. J. Veh. Mech. Mobil.*, vol. 28, no. April 2012, pp. 221–259, 1997.

[49] V. L. Popov, "Contact mechanics and friction: Physical principles and applications," *Contact Mech. Frict. Phys. Princ. Appl.*, vol. 7, no. 3rd edition, pp. 1–362, 2010.

[50] C. Nkundineza and J. A. Turner, "Influence of spatial variations of track stiffness on fatigue crack initiation and propagation," in *2015 Joint Rail Conference, an Jose, California, USA, V001T01A036, ASME*, 2015.

[51] T. G. Johns, K. B. Davies, J. C. Bell, and K. B. Davies, "Engineering Analysis of Stresses in Railroad Rails," 1981.

[52] M. A. Guler and F. Erdogan, "Contact mechanics of two deformable elastic solids with graded coatings," *Mech. Mater.*, vol. 38, no. 7, pp. 633–647, 2006.

[53] Y. Alinia, A. Beheshti, M. A. Guler, S. El-Borgi, and A. A. Polycarpou, "Sliding contact analysis of functionally graded coating/substrate system," *Mech. Mater.*, vol. 94, pp. 142–155, 2016.

[54] J. Drozdziel, B. Sowinski, and A. Szulczyk, “Equivalent track stiffness determination,” in *SCIENTIFIC PROCEEDINGS XIX INTERNATIONAL SCIENTIFIC-TECHNICAL CONFERENCE*, 2011, vol. 3, no. x, pp. 16–18.

[55] R. P. D, R. Murphy, and W. Zhao, “Determining the Stresses in Steel Railroad-Track Rails Due to Freight Movements Using Non- Contact Laser-Speckle Determining the Stresses in Steel Railroad- Track Rails Due to Freight Movements Using Non-Contact Laser-Speckle Kansas State University,” 2012.

[56] A. Mayers, “The effect of heavy haul train speed on insulated rail joint bar strains,” *Aust. J. Struct. Eng.*, vol. 7982, no. September, pp. 2204–2261, 2017.

[57] A. Kolomeets and T. Sych, “Calibration method for a strain-gauge measurement system based on bidirectional rail loading,” in *MATEC Web of Conferences, Polytransport systems*, 2018, vol. 216.

[58] P. Wang, K. Xie, L. Shao, L. Yan, J. Xu, and R. Chen, “Longitudinal force measurement in continuous welded rail with bi-directional FBG strain sensors,” *Smart Mater. Struct.*, vol. 25, no. 1, 2015.

[59] C. Nkundineza and J. A. Turner, “The influence of spatial variation of railroad track stiffness on the fatigue life,” *Proc. Inst. Mech. Eng. Part F J. Rail Rapid Transit*, vol. 232, no. 3, pp. 824–831, 2018.

[60] C. Nkundineza, “Influence of spatial variations of railroad track stiffness and material inclusions on fatigue life,” PhD Diss., The University of Nebraska, 2015.

[61] T. Jendel, “Prediction of wheel profile wear - Comparisons with field measurements,” *Wear*, vol. 253, no. 1–2, pp. 89–99, 2002.

[62] G. Tao, Z. Wen, Q. Guan, X. Zhao, Y. Luo, and X. Jin, “Locomotive wheel wear simulation in complex environment of wheel-rail interface,” *Wear*, vol. 430–431, no. May, pp. 214–221, 2019.

[63] A. Ramalho, “Wear modelling in rail – wheel contact,” *Wear*, vol. 331, no. 330–331, pp. 524–532, 2015.

[64] Y. Muhamedsalih, J. Stow, and A. Bevan, “Use of railway wheel wear and damage prediction tools to improve maintenance efficiency through the use of economic tyre turning,” *Proc. Inst. Mech. Eng. Part F J. Rail Rapid Transit*, vol. 233, no. 1, pp. 103–117, 2019.

[65] M. Ignesti, M. Malvezzi, L. Marini, E. Meli, and A. Rindi, “Development of a wear model for the prediction of wheel and rail profile evolution in railway systems,” *Wear*, vol. 284–285, pp. 1–17, 2012.

7 APPENDIX

1. Matlab 3D Plot of Contact Pressure Distribution in the contact area

```
% Contact Pressure distribution
clc
clear
clf

R_1 = 360;
R_2 = 380;
C_b = 0.82;
C_a = 0.66;
v_1 = 0.3;
v_2 = 0.3;
E_1 = 200e3;
E_2 = 200e3;
k = 0.81;
P = 71056.09;

delta = ((2*R_1*R_2)/(R_1+R_2))*(((1-v_1^2)/E_1)+(1-v_2^2)/E_2);

b = C_b*(P*delta)^(1/3);
a  = b/k;

sigma_max = -(C_a*b)/delta;

x = linspace(-10,10);
y = linspace(-10,10);

[xx,yy] = meshgrid(x,y);

sigma_y = -sigma_max.*(1-((xx./a).^2)-(yy./b).^2).^(1/2);

surf(xx,yy,real(sigma_y))
colorbar;
xlabel('Longitudinal direction (mm)')
zlabel('Contact pressure(MPa)')
ylabel('Lateral direction (mm)')
```

2. 2D elastic To Elastic frictional contact - Guler Formula

```
clc
clear
clf

v2=0.3; %poison ratio
v3=0.3;
E2=2E5; %E modulus of Elasticity
E3=2E5; %E modulus of Elasticity
mu2=E2/(2*(1+v2)); %G modulus of rigidity
mu3=E3/(2*(1+v3)); %G modulus of rigidity
% k2=3-4*v2;          %Plane Strain
% k3=3-4*v3;
k2=(3-v2)/(1+v2); %Plane Stress
k3=(3-v3)/(1+v3);
gamma=mu3/mu2;
A_star=((k3-1)-(k2-1)*gamma)/((k3+1)+(k2+1)*gamma);
eta=0.4;
theta=atan(abs(1/(A_star*eta)));
alfa=theta/pi;
beta=1-theta/pi;
X=0;
R2=380;
R1=R2/X;

R=1/((1/R1)+(1/R2));
D_star=((k3+1)+(k2+1)*gamma)/4;

%a=0.1*R2/(1+beta/alfa);
a=7;
b=(beta/alfa)*a;
%b=6.3;

P=(mu3*R2)*((2*pi*alfa*beta)/(k3+1))*(((b+a)/R2)^2);

x=linspace(-a-20,b+20,200);
x1=linspace(-a-20,-a,50);
x2=linspace(-a,b,100);
x3=linspace(b,b+20,50);

sigmay=(-mu3/(R*D_star))*(sin(pi*alfa))*((b-x).^alfa).*((x+a).^beta);
sigmayMIN=min(sigmay);

L1=-2*((b-x1).^alfa).*((-x1-a).^beta)-2*x1+b-a+2*(alfa-beta)*(b+a);
L2=((b-x2).^alfa).*((x2+a).^beta).*cos(pi*alfa)-2*x2+b-a+2*(alfa-beta)*(b+a);
L3=2*((x3-b).^alfa).*((x3+a).^beta)-2*x3+b-a+2*(alfa-beta)*(b+a);

sigmax1=(-mu3*eta/(R*D_star))*L1;
p=(1/(R*D_star))*(sin(pi*alfa)).*((b-x2).^alfa).*((x2+a).^beta);
```

```
sigmax2=(-p*mu3)-(mu3*eta/(R*D_star))*L2;
sigmax3=(-mu3*eta/(R*D_star))*L3;

sigmax=[sigmax1 sigmax2 sigmax3];
xx=[x1 x2 x3];

figure(1)
plot(xx,sigmax)
grid on
xlabel('contact patch (mm)')
ylabel('sigmaX (MPa)')

figure(2)
plot(x,sigmay)
grid on
xlabel('contact patch (mm)')
ylabel('sigmaY (MPa)')
```

3. 2D Rolling contact Alinia-Formula

```
clc
clear
clf

R1=Inf;
R2=100;
R0=R2; % 1/R0=(1/R1)+(1/R2)
eta=0.4;
v1=0.3;
v2=0.3; %arbitrarily chosen roller poisson ratio. just to find mu2=Inf.
E1=2E5; %half-plane
E2=2E5; %roller is a rigid body
mu1=E1/(2*(1+v1));
mu2=E2/(2*(1+v2));
% k1=3-4*v1;        %Plane Strain
% k2=3-4*v2;
k1=(3-v1)/(1+v1); %Plane Stress
k2=(3-v2)/(1+v2);
A1=(k1+1)/(4*mu1);
A2=(k2+1)/(4*mu2);
A=A1+A2;

%CONTACT HALF-LENGTH(aa)
aa=5;
P=((aa^2)*pi)/(2*A*R0);
Q=eta*0.75*P;
bb=aa*(2*sqrt(1-abs(Q/(eta*P)))-1);
%MAX. CONTACT PRESSURE
P0=(2*P)/(pi*aa);
```

```
%STRESS-Y
N=500;
x=linspace(-aa,aa,2*N);
x1=linspace(-aa,bb,N); %for 1st condition of sigmaxy
x2=linspace(bb,aa,N); %for 2nd condition of sigmaxy
x3=[x1(:,1:(N-1)) x2]; %for total array of sigmaxy
sigmayy=-P0.*sqrt(1-((x./aa).^2));
sigmayy1=-P0.*sqrt(1-((x1./aa).^2)); %for 1st condition of sigmaxy (sigmaxy1)
sigmayy2=-P0.*sqrt(1-((x2./aa).^2)); %for 2nd condition of sigmaxy (sigmaxy2)
sigmayyMIN=min(sigmayy);
%STRESS-XY
sigma_s=eta.*P0.*sqrt(1-((2.*x1+aa-bb)./(aa+bb)).^2).*(1+bb/aa)/2;
sigmaxy1=eta*(sigmayy1)+sigma_s;
sigmaxy2=eta*(sigmayy2);
sigmaxy=[sigmaxy1(:,1:(N-1)) sigmaxy2]; %total array of sigmaxy
sigmaxyMIN=min(sigmaxy);
sigmaxy=-sigmaxy;


%PLOTS
figure(1)
%Y-STRESS
plot(x,sigmayy)
grid on
xlabel('Contact Length(mm)')
ylabel('sigma-yy (MPa)')

figure(2)
%XY-STRESS
plot(x3,sigmaxy)
grid on
xlabel('Contact Length(mm)')
ylabel('sigma-xy (MPa)')
```

4. Python Scripting Code for Extracting Results in ABAQUS odb File

```
# Function to extract contact forces from a dynamic model.

#Import Abaqus module

from job import *

from sketch import *

from visualization import *

from connectorBehavior import *

import odbAccess

import time
```

```
def extractdata(odbfile,datarequest,filename):

    start_time = time.time()

    #Let open the model output database by calling the Abaqus module odbAccess and its instance openOdb; the parameters are the path of the file and whether the file can be read or not:

    myOdb = odbAccess.openOdb(path=odbfile, readOnly=False)

    #Get the two steps separately and call them step1 and step2

    step1 = myOdb.steps['Pre_Stressing-Step']

    step2 = myOdb.steps['Rolling-Step']

    # Also, initialize a text file name 'max_press.txt' that will store the data and let give it a variable fmcp, and let it open to take data

    fmcp=open(filename,'w')

    #Write headings for each columns: 'Step time','CPRESS','CSHEAR1','CSHEAR2' on same line.

    fmcp.write('Total Time'+'\t')

    [fmcp.write(str(titledata)+'\t') for titledata in datarequest]

    ## Go to the second line for next data writing

    fmcp.write('\n')

    #Let loop over each step

    #initialize initial time to be zero

    t0=0.0

    #From initial step add the total step time of step 1 (From which step 2 time starts). Note that we are extracting data in step 2 only.

    t0+=step1.timePeriod


    #Within each step we want to get the field output as contact force at each frame (or time increment) ; then, we want to acquire the maximum contact force at each

    #frame (by frame we mean at a specific time increment

    ## We need to loop over each frame (or time increment) and extract the maximum contact force append this maximum contact force and write it in the file that has a variable fmcp
```

```
#Then loop over each frame or requested time increment
for frame in step2.frames:
    #Extract step time times
    steptime=t0+frame.frameValue
    fmcp.write(str(steptime)+'\t')

        cvaluedata=frame.fieldOutputs[datav]
        n_data=len(cvaluedata.values)
        #Initialize the list all_cpress which will accept contact pressure data
        all_cdata=[]
        ## Let loop over each contact pressure data and extract it. Note: contact pressure data is extracted by using an attribute,data
        for  i in range(n_data):
                cdata_value=cvaluedata.values[i].magnitude
            #Append each contact pressure at the list, except if the value is zero (This allows us to reduce the computation time)
                if cdata_value>0.00:
                    all_cdata.append(cdata_value)
        #At this moment we have all force data at time increment i listed in all_cpress. we can find maximum value now at time increment i (or frame i) :
        # However if in this frame all contact forces are zero, we can not find maximum value because the list all_cdata is empty. Therefore we add a value of zero if it was empty.
        if all_cdata==[]:
            all_cdata=[0.0]
        max_cd=max(all_cdata)
        fmcp.write(str(max_cd)+'\t') #the paramter '\t' allows us to write the next value at the next column.
    fmcp.write('\n')
        #After looping over all frames,
#Calculate the runtime and write the run time in a file
```

```
run_time=time.time()-start_time

fmcp.write(str(run_time))

# close the text file fmcp

fmcp.close()
```

#Let our abaqus working directory (or location of our output database) be in the folder 'scripting_ex' located in "C:\Documents" and we want to open the file

#To run this file:

complete the scripts to specify inputs (or arguments) to the functions and write the function with its arguments.

go to cmd and navigate to the directory in which this file is located and type: abaqus cae nogui=PostProcessing_cpress.py or the type the whole path without navigating; for example

C:\Users\user\Documents\scripting_ex\PostProcessing_cpress.py

after the run is completed, in the directory a file named max_cdata.xls will have been created and will have all requested data.

You can do the same to extract CPRESS, CSHEAR1 and CSHEAR2 by changing in the code "cvaluedata.values[i].magnitude" to "cvaluedata.values[i].data"

You can also specify which contact surfaces you want to extract the pressure (Note in this model we have defined interaction between the surface of the beam called

odbfile='C:\Users\Mutswatiwa\Documents\scripting_ex\Contact_JOB.odb'

DataExtract=['CF','CM','CNORMF
ASSEMBLY_RAILTOP_SURF/ASSEMBLY_WHEEL_SURF','CNORMF
ASSEMBLY_WHEEL_SURF/ASSEMBLY_RAILTOP_SURF','CSHEARF
ASSEMBLY_RAILTOP_SURF/ASSEMBLY_WHEEL_SURF','CSHEARF
ASSEMBLY_RAILTOP_SURF/ASSEMBLY_WHEEL_SURF']

filename='C:\Users\Mutswatiwa\Documents\scripting_ex\max_cdata2.xls'

extractdata(odbfile,DataExtract,filename)

5. Fast fourier transform code in Matlab

```
clc
clear
clf

dataset = xlsread('Contact_force.xlsx', 'WheelNforc', 'A02:I290');
```

```
x = dataset(:,1);
y = dataset(:,2);
y1 = dataset(:,3);
y2 = dataset(:,4);
y3 = dataset(:,5);
y4 = dataset(:,6);
y5 = dataset(:,7);
y6 = dataset(:,8);
y7 = dataset(:,9);


%upload signal input yt
Fs = 20000;                                % Sampling frequency
T=1/Fs;                                    % Sample time
dt = 0:T:0.05-T;

%model 1 uniform modulus
L=length(y);                               % Length of response signal
NFFT = 2^nextpow2(L);                      % Next power of 2 from length of ft

ff = fft(y,NFFT);
fff = ff(1:NFFT/2);
xfff = Fs * (0:NFFT/2-1)/NFFT;
ffff = fff/max(fff);

%model 2 3 crosstie modulus ratio
L1=length(y1);                               % Length of response signal
NFFT1 = 2^nextpow2(L1);                      % Next power of 2 from length of ft

ff1 = fft(y1,NFFT1);
fff1 = ff1(1:NFFT1/2);
xfff1 = Fs * (0:NFFT1/2-1)/NFFT1;
fff11 = fff1/max(fff1);

%model 3 0.5 crosstie modulus ratio
L2=length(y2);                               % Length of response signal
NFFT2 = 2^nextpow2(L2);                      % Next power of 2 from length of ft

ff2 = fft(y2,NFFT2);
fff2 = ff2(1:NFFT2/2);
xfff2 = Fs * (0:NFFT2/2-1)/NFFT2;
fff22 =fff2/max(fff2);

%model 4 0.2867 crosstie modulus ratio

L3=length(y3);                               % Length of response signal
NFFT3 = 2^nextpow2(L3);                      % Next power of 2 from length of ft

ff3 = fft(y,NFFT3);
fff3 = ff3(1:NFFT3/2);
xfff3 = Fs * (0:NFFT3/2-1)/NFFT3;
fff33 =fff3/max(fff3);

%model 5 2 crosstie modiulus ratio
L4=length(y4);                               % Length of response signal
NFFT4 = 2^nextpow2(L4);                      % Next power of 2 from length of ft

ff4 = fft(y,NFFT4);
```

```
fff4 = ff4(1:NFFT4/2);
xfff4 = Fs * (0:NFFT4/2-1)/NFFT4;
fff44 = fff4/max(fff4);

%model 6 0.143 crosstie modiulus ratio
L5=length(y5);                          % Length of response signal
NFFT5 = 2^nextpow2(L5);                 % Next power of 2 from length of ft

ff5 = fft(y,NFFT5);
fff5 = ff5(1:NFFT5/2);
xfff5 = Fs * (0:NFFT5/2-1)/NFFT5;
fff55 = fff5/max(fff5);

%model 7 2.5 crosstie modiulus ratio
L6=length(y6);                          % Length of response signal
NFFT6 = 2^nextpow2(L6);                 % Next power of 2 from length of ft

ff6 = fft(y,NFFT6);
fff6 = ff6(1:NFFT6/2);
xfff6 = Fs * (0:NFFT6/2-1)/NFFT6;
fff66 = fff6/max(fff6);

%model 8 0.2 crosstie modiulus ratio
L7=length(y7);                          % Length of response signal
NFFT7 = 2^nextpow2(L7);                 % Next power of 2 from length of ft

ff7 = fft(y,NFFT7);
fff7 = ff7(1:NFFT7/2);
xfff7 = Fs * (0:NFFT7/2-1)/NFFT7;
fff77 = fff7/max(fff7);



figure(1)
plot(xfff,abs(ffff))
xlabel('Frequence')
ylabel('Amplitude')

hold on
plot(xfff1,abs(fff11), 'g')
plot(xfff2,abs(fff22), 'r')
plot(xfff3,abs(fff33), 'black')
plot(xfff4,abs(fff44), 'g--')
plot(xfff5,abs(fff55), 'black--')
plot(xfff6,abs(fff66), 'r--')
plot(xfff7,abs(fff77), 'b--')
legend('Ratio-1', 'Ratio-3', 'Ratio-0.5')
```